

Synthesis of functional inorganic nanofibers using
cellulose nanofibers as templates

Shunsuke Gunji

2016

Contents

General Introduction	1
-----------------------------------	---

Chapter 1 Synthesis of SiO₂ nanofibers using templates of TEMPO-oxidized cellulose nanofibers (TOCN)	16
--	----

1.1 Introduction	
1.2 Experimental procedure	
1.3 Results and discussion	
1.4 Conclusion	
References	

Chapter 2 Synthesis and photocatalytic properties of SiO₂/TiO₂ nanofibers using TOCN as templates	
--	--

2.1 Synthesis of SiO ₂ /TiO ₂ nanofibers using TOCN as templates.....	31
---	----

2.1.1 Introduction	
2.1.2 Experimental procedure	
2.1.3 Results and discussion	
2.1.4 Conclusion	
References	

2.2 Photocatalytic properties of SiO ₂ /TiO ₂ nanofibers toward model organic pollutant of methylene blue	45
2.2.1 Introduction	
2.2.2 Experimental procedure	
2.2.3 Results and discussion	
2.2.4 Conclusion	
References	

Chapter 3 Synthesis and gas sensing properties of SiO₂/SnO₂ nanofibers using TOCN as templates

3.1 Synthesis of SiO ₂ /SnO ₂ nanofibers using TOCN as templates and effect of acetylacetone to stabilize Sn precursor.....	68
3.1.1 Introduction	
3.1.2 Experimental procedure	
3.1.3 Results and discussion	
3.1.4 Conclusion	
References	
3.2 Effect of synthesis condition of SiO ₂ /SnO ₂ nanofibers on gas sensing properties toward ethanol.....	87
3.2.1 Introduction	
3.2.2 Experimental procedure	
3.2.3 Results and discussion	
3.2.4 Conclusion	
References	

3.3 Advantage in gas sensing properties of SiO ₂ /SnO ₂ nanofibers compared to conventional SnO ₂ nanoparticles.....	105
3.3.1 Introduction	
3.3.2 Experimental procedure	
3.3.3 Results and discussion	
3.3.4 Conclusion	
References	
3.4 Gas sensing properties of SiO ₂ /SnO ₂ nanofibers under humid conditions	120
3.4.1 Introduction	
3.4.2 Experimental procedure	
3.4.3 Results and discussion	
3.4.4 Conclusion	
References	
Publication List.....	134
Acknowledgements.....	136
Copyrights and Sources.....	137

General Introduction

The first scientific discussion of nanotechnology can be attributed to the lecture “There’s Plenty of Room at the Bottom” in 1959 by Richard Feynman who was a Nobel Prize winner in physics [1]. Today, almost sixty years later, nanotechnology is constantly advancing and plays important roles in a wide range of disciplines, such as chemistry [2], biology [3], architecture [4], electronics [5], agriculture [6], energy engineering [7], and environmental engineering [8]. Nanomaterials, which are typically defined as materials with sizes on the order of nanometers [9], exhibit excellent properties that are significantly different from those of the respective bulk materials because of their high surface-to-volume ratio and quantum size effects [10]. Nanomaterials can be classified into four groups: zero-dimensional (0D), one-dimensional (1D), two-dimensional (2D), and three-dimensional (3D) [11] in the viewpoint of its limited space.

In particular, nanofibers, which are representative of 1D nanomaterials, have excellent properties such as high mechanical strength [12], high specific surface area [13], desirable hydrodynamic characteristics [14], high electrical and thermal conductivities [15, 16], high thermal stability [17], and good optical transparency [18]. In general, nanofibers consist of organic components (e.g. polymers, supermolecules) and/or inorganic components (e.g. metals, ceramics) [19-21]. Inorganic oxide nanofibers are very attractive materials in terms of their unique optical, magnetic, and electrical properties in addition to their chemical and physical stability [22]. In practice, the use of 1D nanomaterials as the building blocks for 3D structures is preferable because such hierarchical sizes can enhance the diffusion of ions or molecules, resulting in more efficient devices such as lithium ion storage and photocatalysts [23, 24]. As

shown in Table 1, inorganic oxide nanofibers have been applied in various areas [25-41]. Although 1D inorganic oxide nanomaterials can be produced using several methods such as self-organization [42], laser spinning [43], and the most popular method of electrospinning [44, 45], it is still difficult to produce nanofibers with diameters of several nanometers. Thinning the diameter of nanofibers can result in higher mechanical strength [12], higher surface-to-volume ratio [13], higher electrical conductivity [16, 46], and improved quantum size effect [47], leading to promising materials for next-generation devices.

In the 1990s, C. R. Martin et al. pioneered the concept of template synthesis for fabricating 1D organic and/or inorganic nanomaterials [48-50]. The greatest advantage of this method is that the obtained 1D inorganic nanomaterials retain the original fine and unique structures of the templates, even though the dimensions are on the order of several nanometers [51, 52]. Recently, cellulose nanofibers have gained significant attention because they are sustainable and diversified resources with dimensions on the order of several or a dozen nanometers. Cellulose nanofibers consist of individual microfibrils or a bundle of microfibrils derived from plant cell walls [53] (Fig. 1). It is possible to obtain these nanofibers from refined wood pulp using mechanical or chemical methods [54, 55]. In 2005, J. Huang et al. [56] reported the synthesis of nanotubular SnO₂ templated by cellulose fibers in a filter paper. Their report was followed by several other reports on synthesizing 1D organic-inorganic hybrid and inorganic oxide nanomaterials using cellulose nanofibers as templates [57-63].

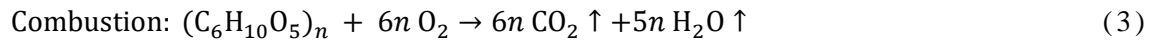
Among several kinds of cellulose nanofibers, 2,2,6,6-tetramethylpiperidine-1-oxyl (TEMPO)-oxidized cellulose nanofibers (TOCN) are attracting much attention [64]. TOCN have the thinnest diameters (3 to 5 nm) among various cellulose nanofibers prepared using different processes [65, 66]. However, because precursors of inorganic oxide typically react with hydroxyl groups on a normal cellulose surface, the presence of carboxyl groups that cover

the surfaces of TOCN make it difficult to use surface deposition, resulting in few reports on the template synthesis of fibrous inorganic oxide materials with TOCN as templates [67]. There have also been no reports on the treatment of TOCN with a silane coupling agent for 1D inorganic oxide nanomaterial synthesis.

Figure 2 shows the concept of the synthesis procedure used in this thesis. Following this concept, new approaches to synthesizing and functionalizing inorganic oxide nanofibers were carried out. In this thesis, I report the synthesis of inorganic oxide nanofibers via the modification of TOCN surfaces, the deposition of inorganic oxide; and the combustion of TOCN as templates in air. The surface modification was carried out using a silane coupling agent. Silane coupling agents, which are silicon alkoxides with functional groups that are different from those of alkoxy groups, are typically used to facilitate stiff adhesion or bonding between polymer matrixes and inorganic fillers owing to their silanol groups [68]. Using a silane coupling agent, silanol groups were introduced to facilitate condensation reactions by the sol-gel process. Through the deposition of inorganic oxides, sol-gel process was carried out. The sol-gel process typically occurs through the following hydrolysis and condensation reactions [69]:



where M is a metal or nonmetal atom (e.g. Si, Ti, Sn in this thesis) and OR is an alkoxy group. After the combustion of TOCN in air, the degraded products, CO₂ and H₂O, are ejected from the reaction system as follows:



With the concept described above, an attempt was made to synthesize various types of nanofibers with core-shell structures. Further deposited oxides were TiO_2 or SnO_2 which are the most popular materials as photocatalyst and gas sensor, respectively [70, 71]. SiO_2 acts as good substrate by providing stiff covalent Si-O-M bonding [72]. Moreover, it is known that SiO_2 affects the properties and state of supported material by suppressing grain growth and modifying coordination [73, 74]. Here, improved properties as photocatalyst and gas sensor through the effect of SiO_2 toward surface phenomena are reported.

Summary of each chapter

Chapter 1:

SiO₂ nanofibers with diameters of approximately 4 nm were successfully synthesized with the template of TEMPO-oxidized cellulose nanofibers (TOCN). In the experiment, the sequential treatment of two types of Si alkoxides in aqueous suspension was employed, and the structural changes that occurred after the treatment of each reagent were investigated. First, the surface carboxyl groups were converted into silanol groups by 3-aminopropyltrimethoxysilane (APTMS) of a silane coupling agent via electrostatic adsorption. Then, the Si–O–Si networks were created by the subsequent treatment of tetramethoxysilane (TMOS). As the result, it was revealed that the sequential treatment of APTMS and TMOS was essential for retaining the original fine structure of the TOCN template after calcination at 500°C. It should be remarked that the obtained structure of the SiO₂ nanofibers was not tubular because once introduced pore might be sintered immediately because of the extremely thin diameters of the TOCN.

Chapter 2:

SiO₂/TiO₂ core-shell nanofibers with diameters of approximately 8 nm were successfully synthesized. Moreover, the photocatalytic properties of the obtained nanofibers were estimated. In the synthesis process, the TOCN covered with SiO₂ were used as starting material. TiO₂ was deposited onto the TOCN with Ti isopropoxide in ethanol suspension. After calcination at 500°C, SiO₂/TiO₂ nanofibers, which were composed of a core of amorphous SiO₂ and a shell of anatase TiO₂, were obtained. The nanofibers exhibited high Brunauer–Emmett–Teller (BET) specific surface areas of more than 100 m²/g. The photocatalytic degradation properties of the SiO₂/TiO₂ nanofibers toward the model pollutant of methylene blue (MB) were characterized

and compared to those of a reference sample of porous TiO₂ particles with a similar specific surface area under irradiation by a metal halide lamp. In spite of the lower optical absorbance and the lower generation of OH radicals which largely contributes to the photocatalytic degradation of MB, the SiO₂/TiO₂ nanofibers exhibited faster photocatalytic degradation. This can be attributed to partially exposed SiO₂ on the surfaces of the nanofibers. The SiO₂ acted as a sorbent for the cationic pollutant of MB, thus bringing the MB into close proximity with the photocatalytic site of TiO₂, which in turn provided more efficient degradation. The detailed degradation kinetics and recyclability were also investigated.

Chapter 3:

SiO₂/SnO₂ core-shell nanofibers with diameters of approximately 10 nm were synthesized. The gas sensing properties of the SiO₂/SnO₂ nanofibers toward reductive species, namely ethanol, H₂, and CO were characterized. Although the synthesis procedure was almost the same as that of the SiO₂/TiO₂ nanofibers, it differed in the use of Sn (IV) isopropoxide and a stabilizing agent of acetylacetone. The obtained SiO₂/SnO₂ nanofibers were composed of amorphous SiO₂ and rutile phase SnO₂. By controlling the amount of acetylacetone, the crystallite size of SnO₂, which affects its sensitivity as a gas sensor in an inverse relationship [75], was suppressed to be 3.2 nm after calcination at 500°C. When the sensitivities toward ethanol gas were compared, the SiO₂/SnO₂ nanofibers with the crystallite size of 3.2 nm exhibited a sensitivity that was approximately ten times larger than that of the SiO₂/SnO₂ nanofibers with a crystallite size of 11 nm. Furthermore, the gas sensing properties of the SiO₂/SnO₂ nanofibers were compared to those of hydrothermally synthesized SnO₂ nanoparticles. From the results, it was found that the SiO₂/SnO₂ nanofibers could act as highly sensitive gas sensors at higher temperatures whereas the SnO₂ nanoparticles showed little

sensitivity. This property is suitable for detecting less-reactive species such as methane [76]. The gas sensing reaction can be attributed to the reaction of the chemisorbed oxygen with the analyte gas. Hence, it seems that the presence of SiO₂ affects the adsorption behavior of oxygen and/or the analyte gas.

References

1. C.M. Shea, *Journal of Engineering and Technology Management* 22, 185 (2005).
2. G. M. Whitesides, *Small*, 1, 172 (2005).
3. A. Albanese, P. S. Tang, and W. C. W. Chan, *Annual Review of Biomedical Engineering* 14, 1 (2012).
4. F. Sanchez and K. Sobolev, *Construction and Building Materials* 24, 2060 (2010).
5. M. T. Bohr, *IEEE Transactions on Nanotechnology* 1, 1 (2002).
6. L. R. Khot, S. Sankaran, J. M. Maja, R. Ehsani, and E. W. Schuster, *Crop Protection* 35, 64 (2012).
7. E. Serrano, G. Rus, and J. García-Martínez, *Renewable and Sustainable Energy Reviews* 13, 2373 (2009).
8. D. G. Rickerby and M. Morrison, *Science and Technology of Advanced Materials* 8, 19 (2007).
9. D. R. Boverhof, C. M. Bramante, J. H. Butala, S. F. Clancy, M. Lafranconi, J. West, and S. C. Gordon, *Regulatory Toxicology and Pharmacology* 73, 137 (2015).
10. C. Bréchnac, P. Houdy, and M. Lahmani, *Nanomaterials and Nanochemistry* (Springer-Verlag GmbH, 2007).
11. L. J. Liu and S. Bashir, *Advanced Nanomaterials and their Applications in Renewable Energy* (Elsevier Inc., 2007).
12. F. Chen, X. Peng, T. Li, S. Chen, X. F. Wu, H. R. Reneker, and H. Houl, *Journal of Physics D: Applied Physics* 41, 025308 (2008).
13. V. Thavasi, G. Singh, and S. Ramakrishna, *Energy & Environmental Science* 1, 205 (2008).
14. V. Tomer, R. Teye-Mensah, J. C. Tokash, N. Stojilovic, W. Kataphinan, E. A. Evans, G. G. Chase, R. D. Ramsier, D. J. Smith, and D. H. Reneker, *Solar Energy Materials and Solar*

- Cells 85, 477 (2005).
15. S. Shen, A. Henry, J. Tong, R. Zheng, and G. Chen, *Nature Nanotechnology* 5, 251 (2010).
 16. N. T. Xuyen, E. J. Ra, H.-Z. Geng, K. K. Kim, K. H. An, and Y. H. Lee, *The Journal of Physical Chemistry B* 111, 11350 (2007).
 17. G. Korotcenkov and B. K. Cho, *Sensors and Actuators B* 156, 527 (2011).
 18. M. Nogi, M. Karakawa, N. Komoda, H. Yagyu, and T. T. Nge, *Scientific Reports* 5, 17254 (2015).
 19. Z.-M. Huang, Y.-Z. Zhang, M. Kotaki, and S. Ramakrishna, *Composites Science and Technology* 63, 2223 (2003).
 20. R. N. Shah, N. A. Shah, M. M. D. R. Lim, C. Hsieh, G. Nuber, and S. I. Stupp, *Proceedings of the National Academy of Sciences* 107, 3293 (2009).
 21. I. S. Chronakis, *Journal of Materials Processing Technology* 167, 283 (2005).
 22. H. Wu, W. Pan, and H. Li, *Journal of Advanced Ceramics* 1, 2 (2012).
 23. Y. Tan, Q. Gao, C. Yang, K. Yang, W. Tian, and L. Zhu, *Scientific Reports* 5, 12382 (2015).
 24. K. Nakata and A. Fujishima, *Journal of Photochemistry and Photobiology C: Photochemistry Reviews* 13, 169 (2012).
 25. M. Zhi, N. Mariani, R. Gemmen, K. Gerdes, and N. Wu, *Energy & Environmental Science* 4, 417 (2007).
 26. E. Formo, M. S. Yavuz, E. P. Lee, L. Lane, and Y. Xia, *Journal of Materials Chemistry* 19, 3878 (2009).
 27. M. S. Kolathodi, M. Palei, and T. S. Natarajan, *Journal of Materials Chemistry A* 3, 7513 (2015).
 28. Y. Ding, Y. Wang, L. Su, H. Zhang, and Y. Lei, *Journal of Materials Chemistry* 20, 9918 (2010).

29. M. Ge, C. Cao, J. Huang, S. Li, Z. Chen, K.-Q. Zhang, S. S. Al-Deyab and Y. Lai, *Journal of Materials Chemistry A* 4, 6772 (2016).
30. A. Nikfarjam and N. Salehifar, *Sensors and Actuators B: Chemical* 211, 146 (2015).
31. Y.-J. Liu, H.-D. Zhang, X. Yan, A.-J. Zhao, Z.-G. Zhang, W.-Y. Si, M.-G. Gong, J.-C. Zhang, and Y.-Z. Long, *RSC Advances* 6, 85727 (2016).
32. W. Wang, H. Huang, Z. Li, H. Zhang, Y. Wang, W. Zheng, and C. Wang, *Journal of the American Ceramics Society* 91, 3817 (2008).
33. Y. Wang and J. J. Santiago-Avilés, *Nanotechnology* 15, 32 (2004).
34. L. Yan, X. Rui, G. Chen, W. Xu, G. Zou, and H. Luo, *Nanoscale* 8, 8443 (2016).
35. S. Chonan, S. Kato, and T. Aoki, *Scientific Reports* 4, 4785 (2014).
36. I. Lověntinská-Šlamborová, P. Holý, P. Exnar, and I. Veverkoá 2016, 2485173 (2016).
37. H. Wu, D. Lin, and W. Pan, *Applied Physics Letters* 89, 133125 (2006).
38. R. Sahay, P. S. Kumar, V. Aravindan, J. Sundaramurthy, W. C. Ling, S. G. Mhaisalkar, S. Ramakrishna, and S. Madhavi, *The Journal of Physical Chemistry C* 116, 18087 (2012).
39. X. Xia, S. Li, X. Wang, J. Liu, Q. Wei, and X. Zhang, *Journal of Materials Science* 48, 3378 (2013).
40. Q. Qi, T. Zhang, L. Liu, and X. Zheng, *Sensors and Actuators B: Chemical* 137, 471 (2009).
41. H.-W. Kim and H.-E. Kim, *Journal of Biomedical Materials Research* 77, 323 (2006).
42. Y. Hu, L. He, and Y. Yin, *Angewandte Chemie International Edition* 50, 3747 (2011).
43. S. Itoh, M. Sakakura, Y. Shimotsuma, and K. Miura, *Applied Physics B* 119, 519 (2015).
44. I. Kim and A. Rothschild, *Polymers Advanced Technologies* 22, 318 (2011).
45. D. Li and Y. Xia, *Advanced Materials* 16, 1151 (2004).
46. X. M. Tao, *Wearable Electronics and Photonics* (Woodhead Publishing Limited, 2005).

47. Y.-M. Lin, X. Sun, and M. S. Dresselhaus, *Physical Review B* 62, 4610 (2000).
48. W. Liang and C. R. Martin, *Journal of the American Chemical Society* 112, 3445 (1990).
49. J. D. Klein, R. D. I. Herrick, D. Palmer, M. J. Sailor, C. J. Brumlik, and C. R. Martin, *Chemistry of Materials* 5, 902 (1993).
50. J. C. Hulthen and C. R. Martin, *Journal of Materials Chemistry* 7, 1075 (1997).
51. S. J. Hurst, E. K. Payne, L. Qin, and C. A. Mirkin, *Angewandte Chemie International Edition* 45, 2672 (2006).
52. H.-W. Liang, S. Liu, and S.-H. Yu, *Advanced Materials* 22, 3925 (2010).
53. H. Zhu, Z. Fang, C. Prestron, Y. Li, and L. Hu, *Energy & Environmental Science* 7, 269 (2014).
54. T. Kondo, R. Kose, H. Naito, and W. Kasai, *Carbohydrate Polymer* 112, 284 (2014).
55. Y. Habibi, *Chemical Society Reviews* 43, 1519 (2014).
56. J. Huang, N. Matsunaga, K. Shimano, N. Yamazoe, and T. Kunitake, *Chemistry of Materials* 17, 3513 (2005).
57. Y. Gu, X. Liu, T. Niu, and J. Huang, *Chemical Communications* 46, 6096 (2010).
58. J. Huang and Y. Gu, *Current Opinion in Colloid & Interface Science* 16, 470 (2011).
59. Y. Gu and J. Huang, *Chemistry – A European Journal* 19, 10971 (2013).
60. Y. Zhang, X. Liu, and J. Huang, *ACS Applied Materials & Interfaces* 3, 3272 (2011).
61. H. Scheel, C. Zollfrank, and P. Greil, *Journal of Materials Research* 24, 1709 (2009).
62. J. T. Korhonen, P. Hiekkataipale, J. Malm, M. Karppinen, O. Ikkala, and R. H. A. Ras, *ACS Nano* 5, 1967 (2010).
63. D. Sun, J. Yang, and X. Wang, *Nanoscale* 2, 287 (2010).
64. A. Isogai, T. Saito, and H. Hukuzumi, *Nanoscale* 3, 71 (2011).
65. Y. Qing, R. Sabo, J. Y. Zhu, U. Agarwal, Z. Cai, and Y. Wu, *Carbohydrate Polymer* 97, 226

(2013).

66. Y. Habibi, L. A. Lucia, and O. J. Rojas, *Chemical Reviews* 110, 3479 (2010).
67. L. Melone, L. Altomare, I. Alfieri, A. Lorenzi, L. D. Nard, and C. Punta, *Journal of Photochemistry and Photobiology A: Chemistry* 261, 53 (2013).
68. N. Suzuki and H. Ishida, *Macromolecular Symposia* 118, 19 (1996).
69. C. J. Brinker and G. W. Scherer, *Sol-gel science, the physics and chemistry of sol-gel processing* (Academic Press, Inc., 1991).
70. M. Pelaez, N. T. Nolan, S. C. Pillai, M. K. Seery, P. Falaras, A. G. Kontos, P. S.M. Dunlop, J. W.J. Hamilton, J.A. Byrne, K. O'Shea, M. H. Entezari, and D. D. Dionysiou, *Applied Catalysis B: Environmental* 125, 331 (2012).
71. N. Narsan, D. Koziej, and U. Weimar, *Sensors and Actuators B: Chemical* 121, 18 (2007).
72. Y. Gushikem and S. S. Rosatto, *Journal of the Brazilian Chemical Society* 12, 695 (2001).
73. C. He, B. Tian, and J. Zhang, *Journal of Colloid and Interface Science* 344, 382 (2010).
74. Y. Iwasawa, Y. Nakano, and S. Ogasawara, *Journal of the Chemical Society, Faraday Transactions* 74, 2968 (1978).
75. C. Xu, J. Tamaki, N. Miura, and N. Yamazoe, *Sensors and Actuators B* 3, 147 (1991).
76. D. Kohl, *Sensors and Actuators* 18, 71 (1989).

Table.1 Inorganic oxide nanofibers and their potential applications.

Component	Applications	Ref.
ZrO ₂	Fuel cell, catalyst	[25, 26]
NiO	Battery cathode, gas sensor	[27, 28]
TiO ₂	Photocatalyst, solar cell, gas sensor	[29, 30]
ZnO	Optoelectronic device, gas sensor	[31, 32]
PbZrO ₃ -PbTiO ₃	Piezotransducer	[33]
Nb ₂ O ₅	Supercapacitor, battery anode	[34]
SiO ₂	Optical device, drug carrier	[35, 36]
CuO	Electronic device, battery anode	[37, 38]
SnO ₂	Battery anode, gas sensor	[29, 40]
Ca ₁₀ (PO ₄) ₃ (OH, F) ₂	Biomedical implant, artificial bone	[41]

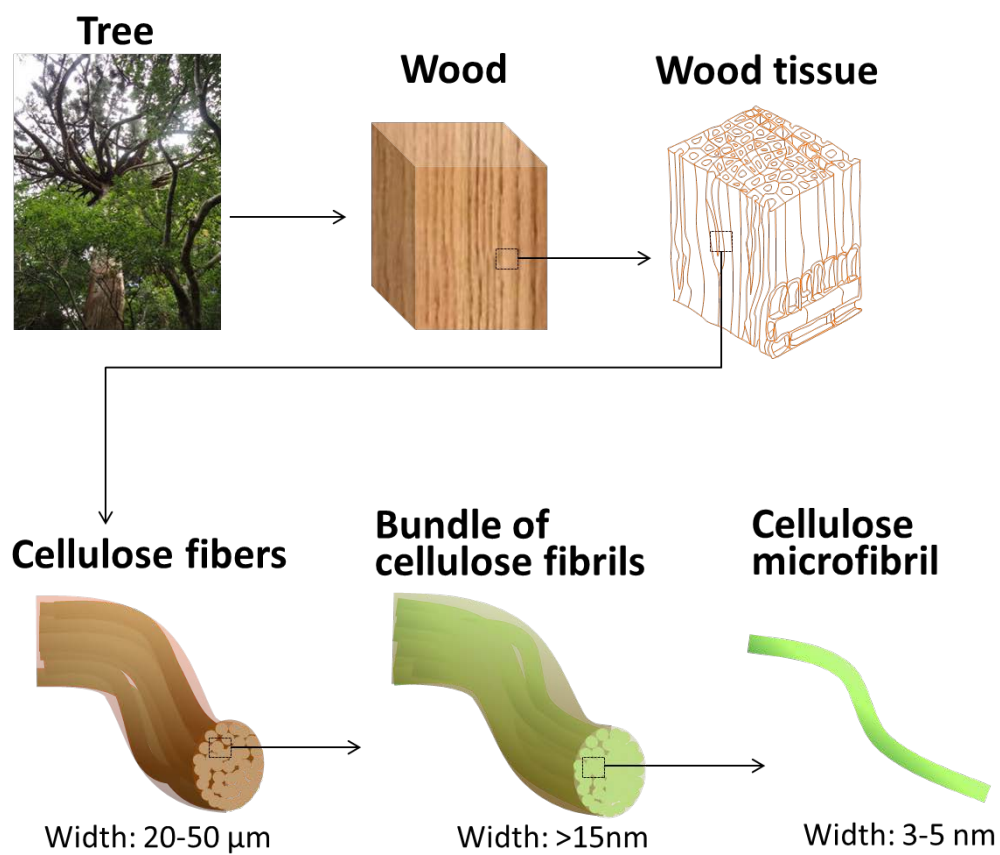


Fig. 1 Schematic of fibrous cellulose derived from wood biomass.

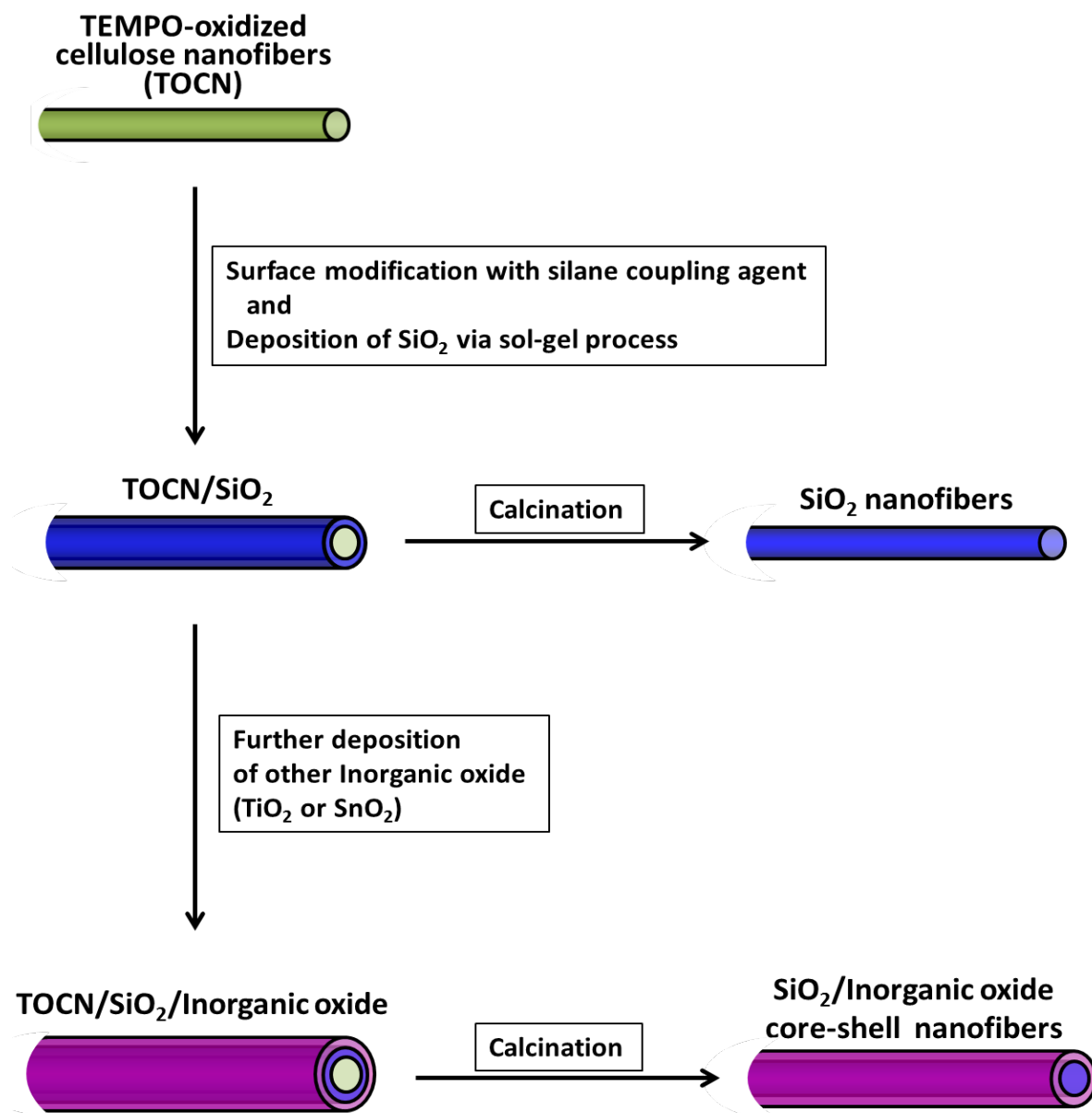


Fig. 2 Schematic procedure for synthesis of SiO_2 nanofibers and SiO_2 /inorganic oxide core-shell nanofibers.

Chapter 1

Synthesis of SiO₂ nanofibers using templates of TEMPO-oxidized cellulose nanofibers

1.1 Introduction

In 2006, Saito et al. reported that the mild chemical oxidation toward natural cellulose fibers mediated by catalyst of 2,2,6,6-tetramethylpiperidine-1-oxyl (TEMPO) brought dissociated cellulose nanofibers with low fibrillation energy [1]. These nanofibers are called TEMPO-oxidized cellulose nanofibers (TOCN). Through the catalytic oxidation reaction using TEMPO, C6 primary hydroxyl groups on the surface of cellulose microfibrils are selectively converted into the sodium salt of the carboxyl groups which cause the electrostatic repulsion force between individual microfibrils (Fig. 1) [2]. It should be noted that TOCN have the thinnest diameters of around 3 to 5 nm among various cellulose nanofibers prepared by the different preparation processes [3, 4]. TOCN have remarkable properties such as high gas barrier properties, optical transparency, and biodegradability due to their significantly thin diameters [5-9].

In terms of the template for the synthesis of inorganic materials, the use of TOCN is still favorable because the synthesized inorganic nanofibers will be able to inherit the characteristics of TOCN such as the very small dimension and the high dissociated state [10]. These structural features would enable wide applications by dispersing them in solvent and matrices (e.g., polymer, ceramics, and pulp) on contrast to inorganic nanofibers synthesized from entangled cellulose templates [11-17]. However, although there reported the preparation of porous inorganic materials using TOCN [18], none on the synthesis of inorganic nanofibers using

TOCN as templates have been reported since ever. Since precursors of inorganic oxide typically react with hydroxide groups on the normal cellulose surface, it is difficult to deposit such precursors on the TOCN surface attached with carboxyl groups.

To solve the problem of conventional deposition, a silane coupling agent was used for the TOCN surface modification. Consequently, it was tried to synthesize SiO₂ nanofibers by using the TOCN as template. These SiO₂ nanofibers have potential applications ranging from optical devices [19], tissue engineering [20], lithium ion storage [21], to biosensor [22]. Furthermore, SiO₂ is widely used as a substrate for the introduction of metal or metal oxide nanoparticles [23]. Actually, SiO₂ can provide positive effect to properties of supported materials by improving the dispersion [24], modifying the coordination of supported material [25, 26], and suppressing the grain growth and phase transition. To overcome the difficulty in the deposition of inorganic oxide onto TOCN, the following sequential treatments were applied. The TOCN once treated with 3-aminopropyltrimethoxysilane (APTMS) of a silane coupling agent were subsequently treated with tetramethoxysilane (TMOS), resulting in the condensation reactions between preliminarily introduced silanol groups and TMOS. Then after the combustion of the TOCN as templates, the structure of obtained SiO₂ nanofibers was characterized.

1.2 Experimental Procedure

1.2.1 Preparation of TEMPO-oxidized cellulose nanofibers (TOCN)

TOCN were prepared by the previously reported TEMPO mediated oxidation method [27], which is the chemical treatment of fibrous cellulose refined from wood cellulose. 4.00 g of fibrous cellulose (KY-100G, Daicel FineChem) was suspended in 400 mL distilled water (Kishida Chemicals) under magnetic stirring for 30 min, and then 400 mg of NaBr (Kishida Chemicals) and 64.0 mg of (2,2,6,6-tetramethylpiperidin-1-yl)oxyl (TEMPO, Sigma-Aldrich)

were added in the suspension. The oxidation of TOCN was initiated by adding 12.4 mL of NaClO solution (Wako Pure Chemicals). The pH value was maintained at 10 by using 0.5 M NaOH (Kishida Chemicals) solution under stirring for 2.5 h at room temperature. The obtained TOCN were washed with distilled water repeatedly using a suction filtration and stored at 4°C as an aqueous dispersion for further experiments.

1.2.2 Synthesis of SiO₂ nanofibers via treatment of silicon alkoxides

To deposit SiO₂ on the TOCN surface, the prepared TOCN were reacted by silicon alkoxides including a silane coupling agent. After the combustion of the TOCN, SiO₂ nanofibers were obtained. In the experiments, two types of silicon alkoxides, 3-aminopropyltrimethoxysilane (APTMS, Sigma-Aldrich) of a silane coupling agent and tetramethoxysilane (TMOS, Sigma-Aldrich), were used. At room temperature, 0.98 mL of APTMS was added to 100 mL of 1.0 wt% TOCN aqueous suspension and stirred for 45 min. After that, the TOCN treated with APTMS were repeatedly washed with distilled water repeatedly using centrifugation at 4000 rpm. Subsequently, 0.10 mL of TMOS was added to 1.0 wt% TOCN aqueous suspension and stirred for 45 min at room temperature. The TOCN treated with APTMS and TMOS were washed with distilled water repeatedly and then the solvent was substituted with 2-propanol (Kishida Chemicals) using centrifugation at 4000 rpm. The treatment only with APTMS or TMOS was also performed as a reference sample. In the treatment only with APTMS, the longer reaction time of 12 h was also conducted. Especially for the treatment only with TMOS, the longer reaction times of 6 h or 12 h were conducted. The same washing and solvent substitution conditions were applied. After the solvent substitution, the TOCN treated with silicon alkoxides were dried with a super critical dryer (SCRD 4, Rexxam) using CO₂. To combust of the TOCN as templates, the TOCN treated with silicon alkoxides were calcined at 500°C for 4 h in air.

1.2.3 Characterization

FT-IR spectra were measured by an FT-IR spectrometer equipped with an ATR accessory (Spectrum Two, Perkin Elmer). Microscopic structures were observed by a field-emission scanning electron microscope (FE-SEM; JSM-6700F, JEOL) with an Energy-dispersive X-ray spectrometer (EDS; JEOL) and a transmission electron microscope (TEM; JEM-2200FS, JEOL).

1.3 Results and discussion

Figure 2 shows the synthesis procedures of the SiO₂ nanofibers. Figure 3 shows FE-SEM images of the initial mechanically prepared commercial cellulose nanofibers (Fma-1002, Sugino Machine), the TOCN prepared by the TEMPO mediated oxidation method, and the TOCN treated with various silicon alkoxides. Figure 4 also shows FE-SEM and TEM image of the TOCN treated with various silicon alkoxides and the successive calcination at 500°C. It should be noted that the chemically prepared TOCN have much finer structures than the mechanically prepared commercial cellulose nanofibers (Fig. 3a, b). After the treatment with silicon alkoxides, there were few obvious differences in structure (Fig. 3c, e, f) except for the TOCN treated with TMOS for 12 h which contained many spherical nanoparticles (Fig. 3d). On the other hand, after calcination at 500°C the large structural differences were observed depending on reagents and times thorough the treatment (Fig. 4). In the calcined TOCN treated only with TMOS, there were no fibrous structures both in 6 h and 12 h (Fig. 4a, b). The shorter one had the micron-size particles and the longer one had the spherical nanoparticles. In the meanwhile, it was revealed that the treatment of APTMS is effective to retain fibrous structures after the calcination (Fig. 4c, d). In the cases of the TOCN treated only with APTMS, the coarsened fibers were obtained,

while in the case of the TOCN treated with both APTMS and TMOS, the fine structures derived from TOCN remained after calcination.

Figure 5 shows FT-IR spectra of the initial TOCN and the TOCN treated with silicon alkoxides. Figure 6 shows FT-IR spectra of these TOCNs after calcination at 500°C. In the initial TOCN spectrum, a broad carboxylate peak typically ranging from 1610 to 1560 cm^{-1} was observed. In particular, the peak positioned at 1605 cm^{-1} is assigned to the $-\text{COONa}$ [28]. This carboxylate peak can be attributed to the introduced surface groups by the TEMPO mediated oxidation. After the treatment only with TMOS, the carboxylate peak did not shift. Especially for longer time of 12 h, there was the new peak of Si–O–Si rocking mode at 457 cm^{-1} before calcination and there were the new peaks of typical amorphous SiO_2 after calcination [29]. The observed spherical particles in Fig. 3d, 4b were assumed to be amorphous SiO_2 nanoparticles. In this case, the fibrous structures did not remain. It can be interpreted in terms of non-existence of the bondings between the surface carboxylate groups and the silicon alkoxides or generated SiO_2 nanoparticles. Meanwhile, after the treatment with APTMS, the carboxylate peak was shifted to 1596 cm^{-1} , indicating the substitution of Na with the amino group of APTMS. This change can be supported by the result that Na was not detected in the elemental analysis of EDS (Fig. 7). No further peak shift was observed, even if such treatment was performed for longer time. The IR peak of amide bonds is typically observed around 1660 cm^{-1} [30]. Although the formation of amide bonds between the carboxyl groups of chemically oxidized carbon nanotubes and the amino groups of aminopropylsilanes in an aprotic polar solvent has been reported [31], in this study, the amide bond was not formed because the formation of amide bond does not take place in water between unactivated carboxylic acid and amine without catalyst [32]. After treatment with TMOS and subsequent to APTMS, more SiO_2 deposition occurred, as indicated by the increasing peak of Si–O–Si rocking mode at 457 cm^{-1} (Fig. 5). It

can be interpreted that silanol groups introduced by TMOS made it possible to occur deposition of SiO₂ via condensations. The presence of Si–O–Si network provided enough robustness, which results in keeping the original fine structure of TOCN through calcination. These clearly indicate that the sequential treatment with APTMS and TMOS was essential.

The SiO₂ nanofibers after calcination of the TOCN treated with APTMS and TMOS exhibited the very thin diameters of approximately 4 nm (Fig. 4e) which is corresponding to that of initial TOCN. From the typical peaks of amorphous SiO₂ (Fig. 6), it was revealed that the obtained SiO₂ nanofibers composed of amorphous SiO₂ same as SiO₂ nanoparticles in Fig. 4b. According to former reports [11, 14-17], the structures of the obtained SiO₂ nanofibers were predicted to be tubular, but no apparent tubular structures were observed. Due to the extremely thin diameters of TOCN [3], such tubular nanostructures derived from the combustion of the TOCN could immediately shrink. In the case that calcination was carried out in inert atmosphere, it is expected that the core-shell nanofibers composed of the core of carbon and shell of SiO₂ will be obtained.

1.4 Conclusion

It was demonstrated that SiO₂ nanofibers could be successfully synthesized by using TEMPO-oxidized cellulose nanofibers (TOCN) as templates. It should be noted that sequential treatments of APTMS and TMOS is effective way to cover the surface of TOCN with sufficient SiO₂ enough to retain the original fine structure after calcination. As the result, the SiO₂ nanofibers, which composed of amorphous SiO₂, were obtained and they showed diameters of approximately 4 nm. The synthesized SiO₂ nanofibers can be applied as adsorbent, catalyst, electrode, and substrate for other materials.

References

1. T. Saito, Y. Nishiyama, J.-L. Putaux, M. Vignon, and A. Isogai, *Biomacromolecules* **7**, 1687 (2006).
2. T. Okita, T. Saito, and A. Isogai, *Biomacromolecules* **11**, 1696 (2010).
3. Y. Qing, R. Sabo, J. Y. Zhu, U. Agarwal, Z. Cai, and Y. Wu, *Carbohydrate Polymer* **97**, 226 (2013).
4. Y. Habibi, L. A. Lucia, and O. J. Rojas, *Chemical Reviews* **110**, 3479 (2010).
5. A. Isogai, T. Saito, and H. Fukuzumi, *Nanoscale* **3**, 71 (2011).
6. H. Koga, T. Saito, T. Kitaoka, M. Nogi, K. Suganuma, and A. Isogai, *Biomacromolecules* **14**, 1160 (2013).
7. H. Fukuzumi, T. Saito, T. Iwata, Y. Kumamoto, and A. Isogai, *Biomacromolecules* **10**, 162 (2009).
8. A. Azetsu, H. Koga, L. Y. Yuan, and T. Kitaoka, *BioResources* **8**, 3706 (2013).
9. H. Koga, A. Azetsu, E. Tokunaga, T. Saito, A. Isogai, and T. Kitaoka, *Journal of Materials Chemistry* **22**, 5538 (2012).
10. H.-W. Liang, S. Liu, and S.-H. Yu, *Advanced Materials* **22**, 3925 (2010).
11. J. Huang, N. Matsunaga, K. Shimano, N. Yamazoe, and T. Kunitake, *Chemistry of Materials* **17**, 3513 (2005).
12. Y. Gu, X. Liu, T. Niu, and J. Huang, *Chemical Communications* **46**, 6096 (2010).
13. J. Huang and Y. Gu, *Current Opinion in Colloid & Interface Science* **16**, 470 (2011).
14. Y. Gu and J. Huang, *Chemistry - A European Journal* **19**, 10971 (2013).
15. Y. Zhang, X. Liu, and J. Huang, *ACS Applied Materials & Interfaces* **3**, 3272 (2011).
16. J. T. Korhonen, P. Hiekkataipale, J. Malm, M. Karppinen, O. Ikkala, and R. H. A. Ras, *ACS Nano* **5**, 1967 (2011).

17. D. Sun, J. Yang, and X. Wang, *Nanoscale* **2**, 287 (2010).
18. L. Melone, L. Altomare, I. Alfieri, A. Lorenzi, L. D. Nard, and C. Punta, *Journal of Photochemistry and Photobiology A: Chemistry* **261**, 53 (2013).
19. S. Ravets, J. E. Hoffman, L. A. Orozco, S. L. Rolston, G. Beadie, and F. K. Fatemi, *Optics Express* **21**, 18325 (2013).
20. W. S. Chen, P. H. Hsieh, W. N. Yang, P. Z. Fan-Jen, M.-L. Yang, J. M. Yeh, Y. Wei, T. Y. Chin, and Y. W. Chen-Yang* , *Journal of Materials Chemistry B* **2**, 1205 (2014).
21. Z. Favors, W. Wang, H. H. Bay, A. George, M. Ozkan, and C. S. Ozkan, *Scientific Reports* **4**, 4605 (2014).
22. J. Shen, X. Yang, Y. Zhu, H. Kang, H. Cao, and C. Li , *Biosensors and Bioelectronics* **34**, 132 (2012).
23. Y. Gushikem and S. S. Rosatto, *Journal of the Brazilian Chemical Society* **12**, 695 (2001).
24. C. He, B. Tian, and J. Zhang, *Journal of Colloid and Interface Science* **344**, 382 (2010).
25. L. Owens and H. H. Kung, *Journal of Catalysis* **144**, 202 (1993).
26. Y. Iwasawam, Y. Nakano, and S. Ogasawara, *Journal of the Chemical Society, Faraday Transactions* **74**, 2968 (1978).
27. T. Saito, S. Kimura, Y. Nishiyama, and A. Isogai, *Biomacromolecules* **8**, 2485 (2007).
28. C. Huang, J. Chen, T. Tsai, Y. Hsieh, K. A. Andrew, *Polymer* **3**, 195 (2015).
29. J. Wang, B. Zou, and M. A. El-Sayed, *Journal of Molecular Structure* **508**, 87 (1999).
30. N. A. Lapin and Y. J. Chabal, *Journal of Physical Chemistry B* **113**, 8776 (2009).
31. K. Babooram and R. Narain, *ACS Applied Materials & Interfaces* **1**, 181 (2009)
32. C. L. Allen, A. R. Chhatwal, and J. M. J. Williams, *Chemical Comuunications* **48**, 666 (2012).

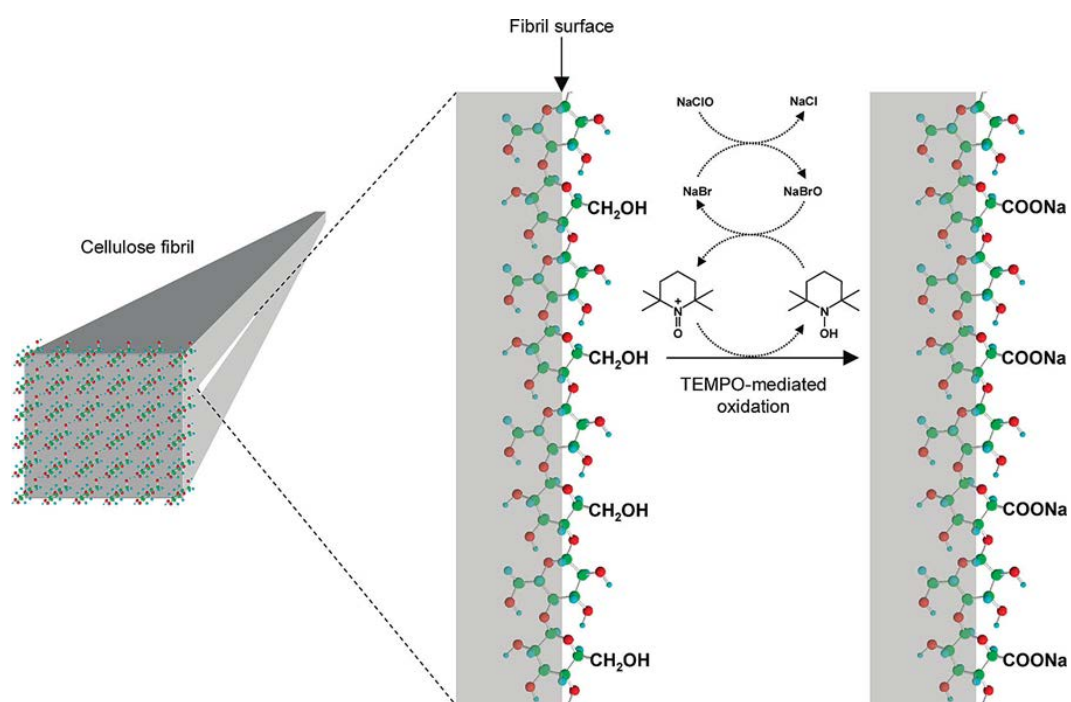


Fig. 1 Schematic of oxidation of C6 primary hydroxyl on cellulose microfibril surfaces by TEMPO-mediated oxidation.

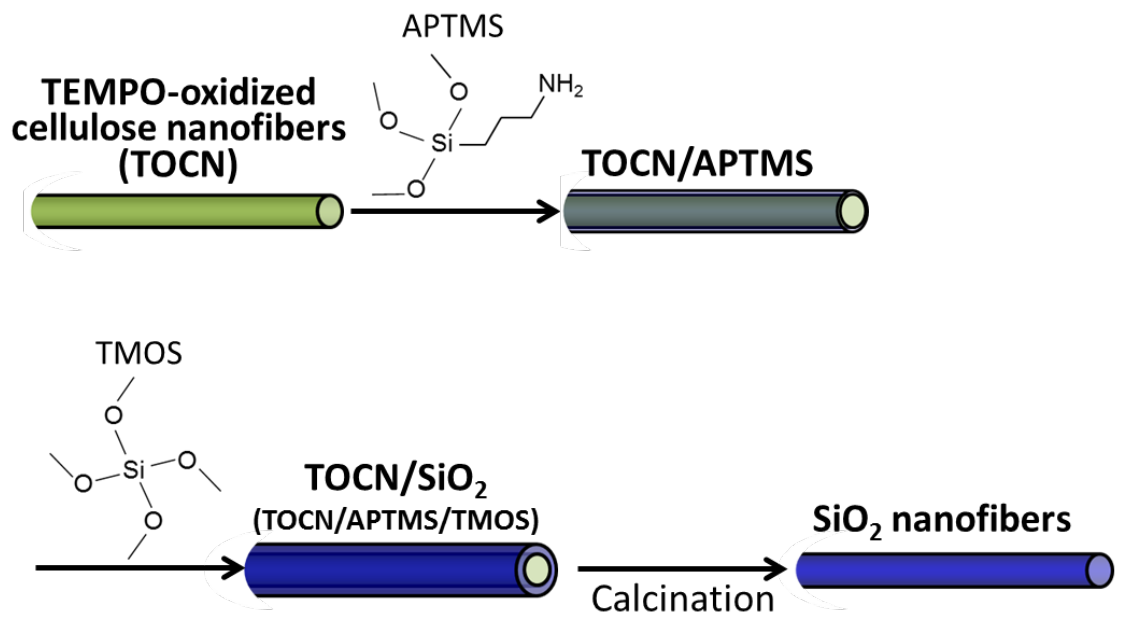


Fig. 2 Schematic procedure for synthesis of SiO₂ nanofibers.

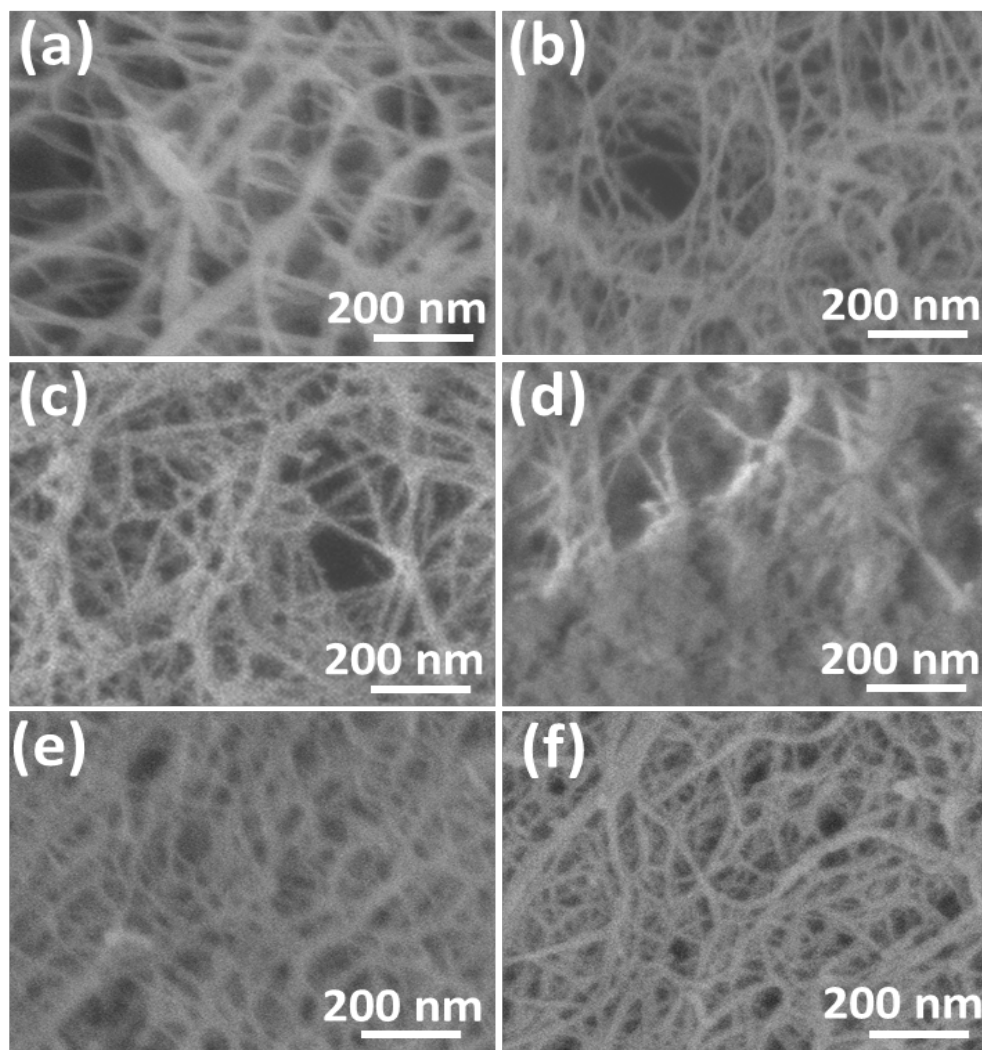


Fig. 3 FE-SEM images of **a** mechanically dissociated cellulose nanofibers, **b** chemically prepared TOCN, **c** TOCN treated TMOS for 6 h, **d** TOCN treated TMOS for 12 h, **e** TOCN treated APTMS for 45 min, and **f** TOCN sequentially treated with APTMS and TMOS for 45 min respectively.

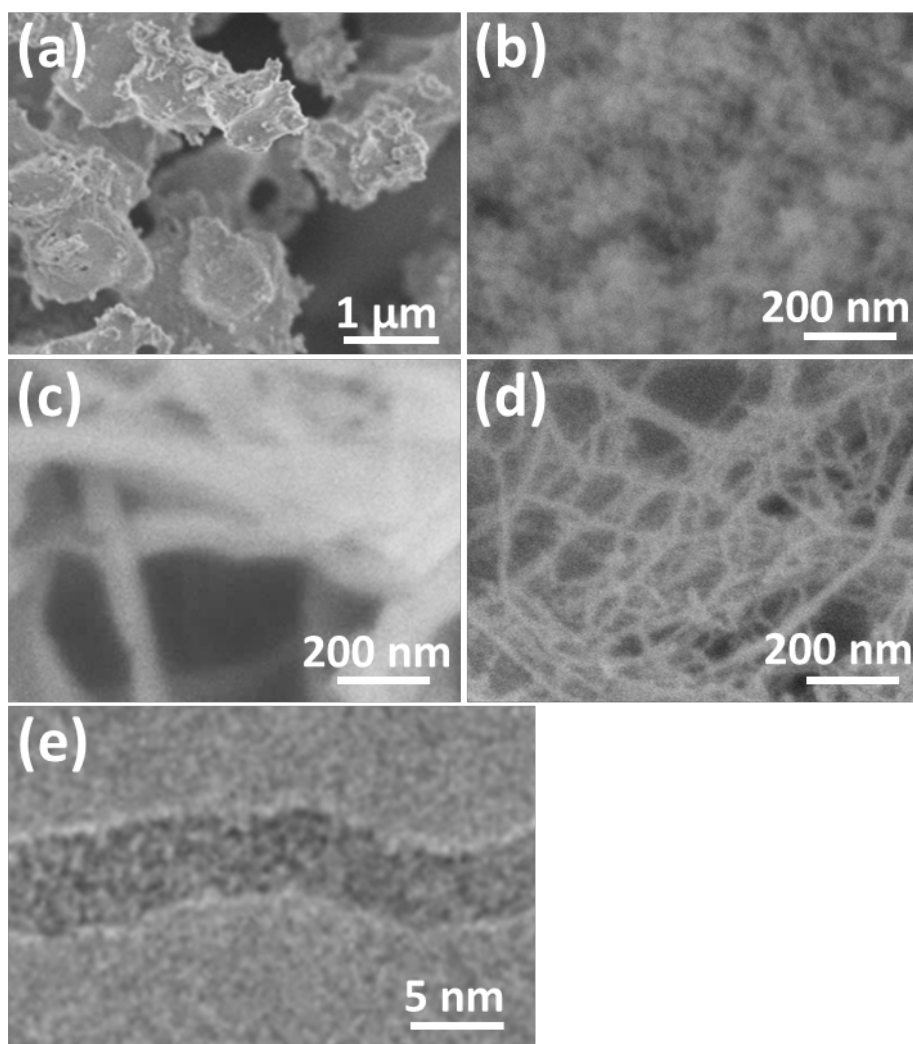


Fig. 4 FE-SEM image of **a** TOCN treated with TMOS for 6 h calcined at 500°C, **b** TOCN treated with TMOS for 12 h calcined at 500°C, **c** TOCN treated with APTMS for 45 min calcined at 500°C, and **d** TOCN sequentially treated with APTMS and TMOS for 45 min respectively calcined at 500°C. **e** TEM image of TOCN sequentially treated with APTMS and TMOS for 45 min respectively calcined at 500°C.

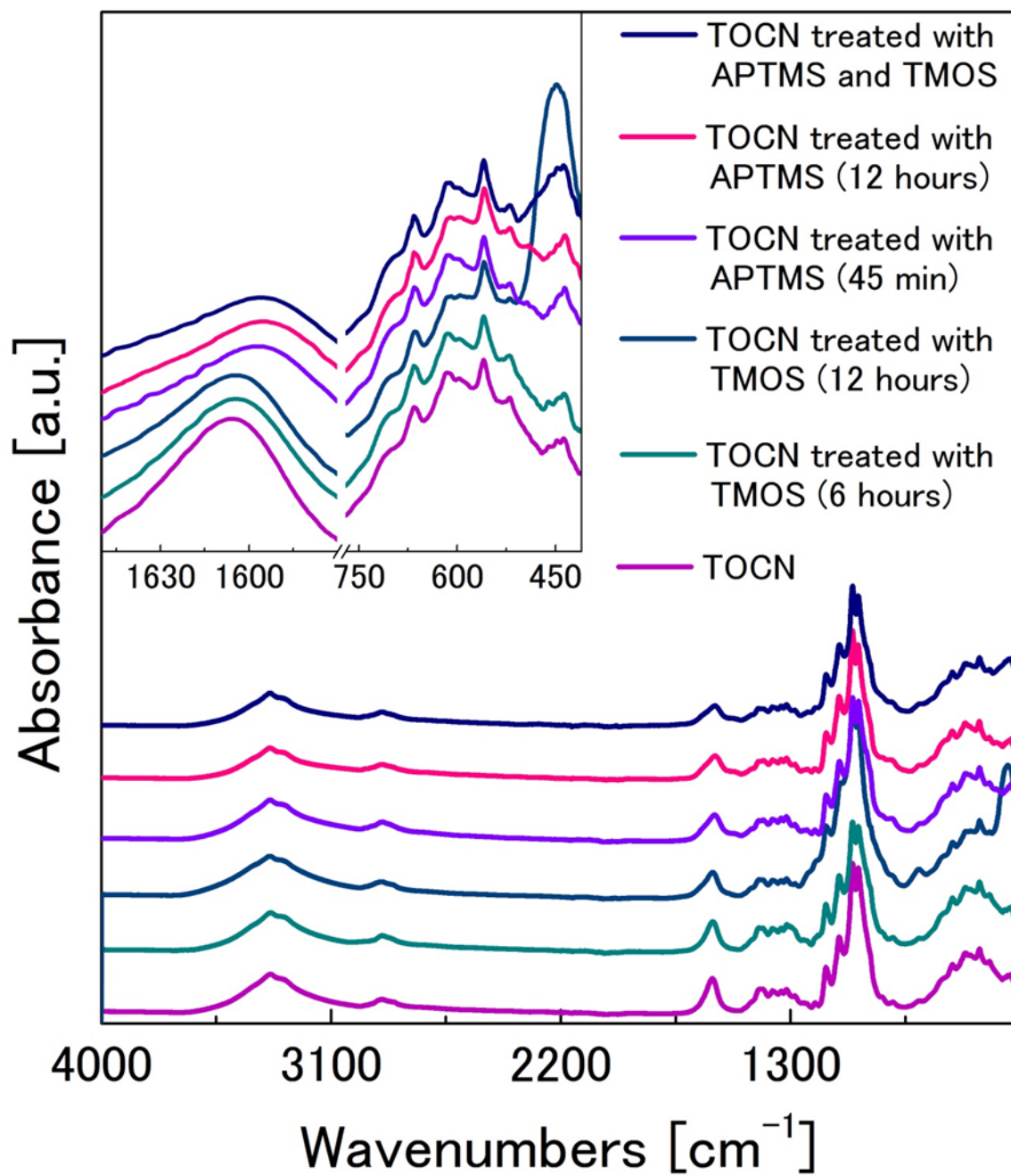


Fig. 5 IR spectra of as-prepared TOCN, and TOCN treated with silicon alkoxides by different conditions.

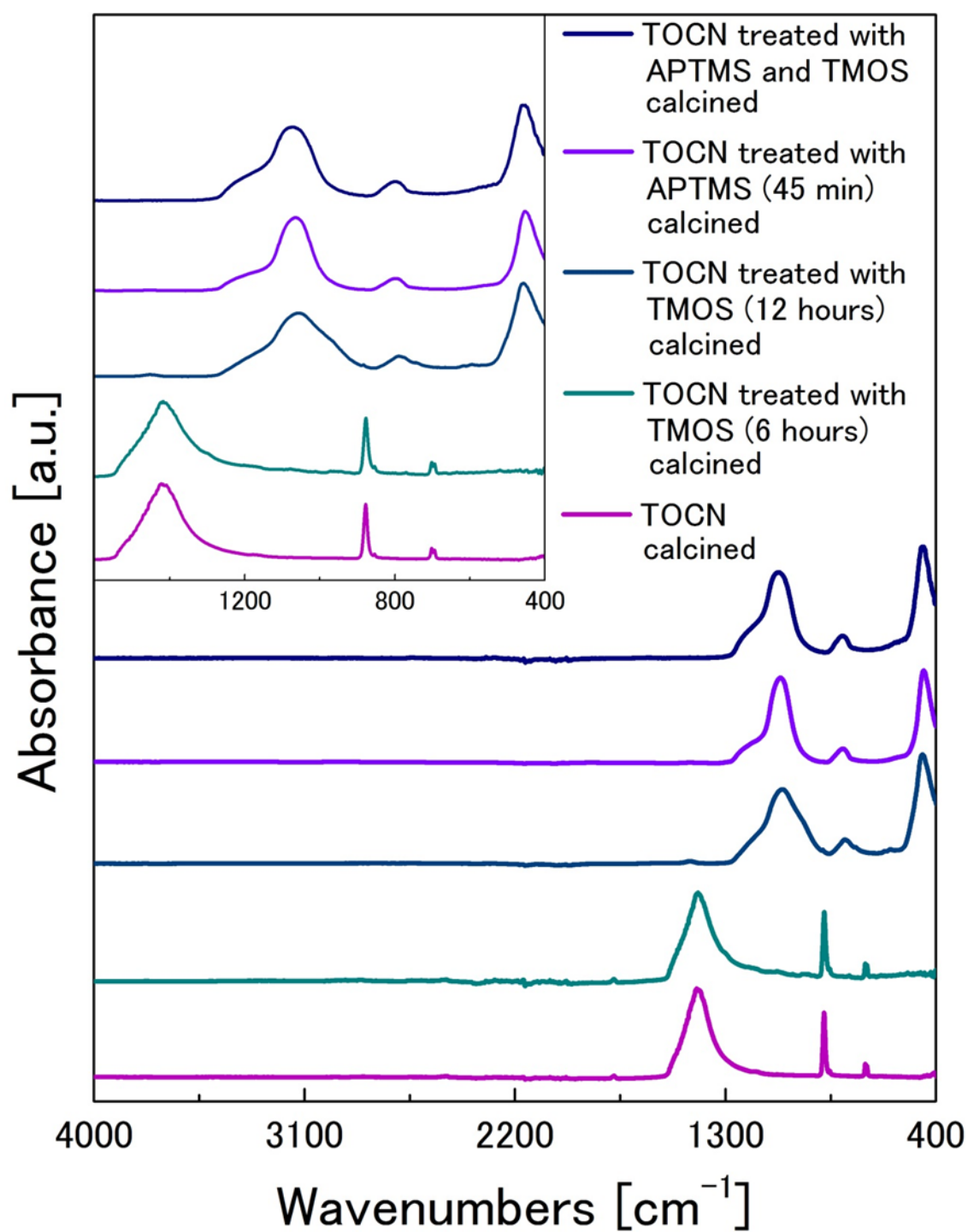


Fig. 6 IR spectra of as-prepared TOCN, and TOCN treated with silicon alkoxides by different conditions after calcination.

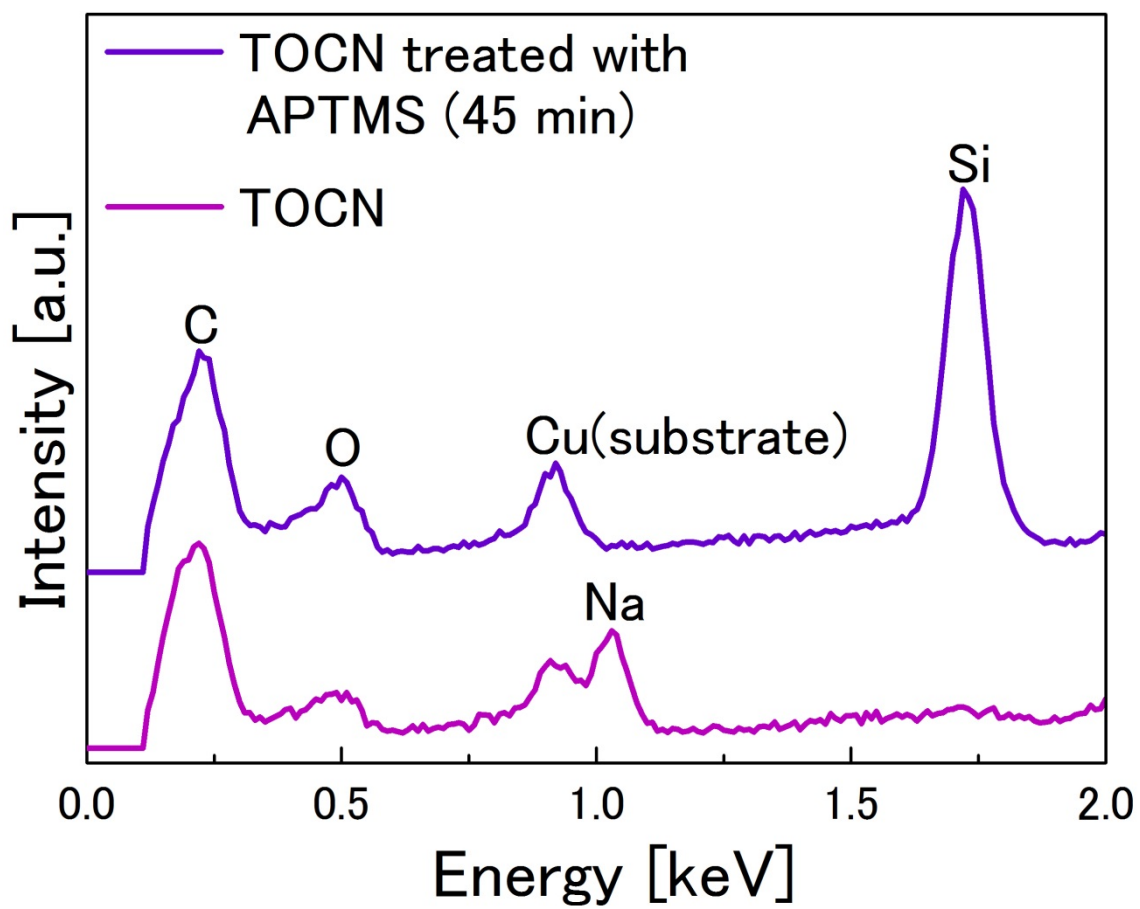


Fig. 7 EDS spectra of TOCN and TOCN treated with APTMS for 45 min.

Chapter 2

Synthesis and photocatalytic properties of SiO₂/TiO₂ nanofibers using TOCN as templates

2.1 Synthesis of SiO₂/TiO₂ nanofibers using TOCN as templates

2.1.1 Introduction

TiO₂ has prominent properties such as chemical stability, non-toxicity, semiconductivity and unique photo-activity, which enable the many promising applications in areas ranging from pigment, sunscreen, anode of dye sensitized solar cell, chemical sensor, to photocatalyst [1]. The first use of TiO₂ as photocatalyst was carried out to bleach dyes by C. F. Goodeve et al. in 1938 [2], and the research of photocatalytic use of TiO₂ was accelerated after the discovery of the electrochemical photolysis of water by A. Fujishima et al. in 1972 [3]. At the present day, in order to broaden the active wavelength region (TiO₂ is generally active at UV region) and to enhance the efficiency of photocatalytic degradations, several material design are employed, for example the doping of anion or cation and the complexing TiO₂ with other metals or inorganic oxides [4].

Compared to the TiO₂ nanoparticle, TiO₂ nanofibers are promising because of good recyclability, high transportation of carriers, and ease of complexing materials [5, 6]. Furthermore, the 3D structures formed with a number of entwined nanofibers are suitable for practical applications because the pores derived from hierarchical structure are good pathways for molecules and ions, resulting in efficient separation, energy storage, and purification. Hence, the almost photocatalytic purifiers are composed of porous ceramics coated with TiO₂ particles, however, there is the problem that TiO₂ particles may be stripped off from the surface [7]. To

avoid the stripping, it is acceptable way to fabricate the composite nanofibers that TiO_2 attached to the substrate through a stable bonding.

Here, the $\text{SiO}_2/\text{TiO}_2$ core-shell type nanofibers with diameters of approximately 8 nm using the TOCN as template were synthesized. In the experiments, the starting materials are TOCN covered with SiO_2 (in the following, TOCN/ SiO_2) after the sequential treatments of APTMS and TMOS as described in the previous chapter. The additional deposition of TiO_2 to TOCN/ SiO_2 was carried out by the hydrolysis and condensation reactions of titanium tetraisopropoxide (TTIP) via making the covalent bond between SiO_2 and TiO_2 . After calcination, the template of TOCN were burned out and as-deposited TiO_2 is crystallized, resulting in $\text{SiO}_2/\text{TiO}_2$ nanofibers composed of the core of amorphous SiO_2 and the shell of anatase phase TiO_2 . The structural changes depending on the fabrication conditions were investigated.

2.1.2 Experimental procedure

2.1.2.1 Synthesis of $\text{SiO}_2/\text{TiO}_2$ nanofibers

To deposit TiO_2 onto the TOCN/ SiO_2 surface, the sol-gel reaction of titanium tetraisopropoxide (TTIP) were performed [8]. After the dispersion medium of the TOCN/ SiO_2 was changed to ethanol (Kishida Chemicals), the suspension was diluted to be 75 mL of 0.10 wt% suspension. Then 1.1 mL of 28 % NH_3 aqueous solution (Kishida Chemicals) in 6.4 mL of ethanol and 35 μL of TTIP (Kishida Chemicals) in 21 mL of ethanol were added and stirred for 12 h at room temperature. After repeated washing by ethanol using centrifugation, the solvent was substituted with 2-propanol (Kishida Chemicals). The TOCN/ SiO_2 treated with TTIP (in the following, TOCN/ $\text{SiO}_2/\text{TiO}_2$) were dried with a super critical dryer (SCRD 4, Rexam) using CO_2 . To obtain $\text{SiO}_2/\text{TiO}_2$ nanofibers through the combustion of the TOCN templates, the dried TOCN/ $\text{SiO}_2/\text{TiO}_2$ were calcined at temperatures between 300°C and 1000 °C for 4 h in air.

2.1.2.2 Characterization

FT-IR spectra were measured by an FT-IR spectrometer equipped with an ATR accessory (Spectrum Two, Perkin Elmer). Microscopic structures were observed by a field-emission scanning electron microscope (FE-SEM; JSM-6700F, JEOL) and a transmission electron microscope (TEM; JEM-2200FS, JEOL) attached with an electron energy loss spectroscopy (EELS). X-Ray diffraction (XRD) patterns were measured by an X-Ray diffractometer (RINT-2500HFK, Rigaku) using $\text{CuK}\alpha$ radiation. Thermogravimetry measurements were carried out in air using a thermogravimetric thermal analyzer (TG8120, Rigaku).

2.1.3 Results and discussion

Figure 1 shows the synthesis procedure of the $\text{SiO}_2/\text{TiO}_2$ nanofibers schematically. Figure 2 shows the thermogravimetric (TG) curve of the TOCN/ $\text{SiO}_2/\text{TiO}_2$ sample. Excluding moisture and solvent weight, the fraction of inorganic component was 23 wt%. In contrast, in the case of the TOCN/ SiO_2 sample before TiO_2 deposition, the fraction of inorganic component was 6.0 wt%. The weight ratio of SiO_2 and TiO_2 in $\text{SiO}_2/\text{TiO}_2$ nanofibers was calculated as following equations derived from the result of the TG analyses.

$$\frac{W_{\text{SiO}_2}}{1+W_{\text{SiO}_2}} = 0.06 \quad (1)$$

$$\frac{W_{\text{SiO}_2} + W_{\text{TiO}_2}}{1+W_{\text{SiO}_2} + W_{\text{TiO}_2}} = 0.23 \quad (2)$$

where W_{SiO_2} and W_{TiO_2} is weight ratio of SiO_2 and TiO_2 to 1 g of TOCN, respectively. It was assumed that W_{SiO_2} did not change through the deposition of TiO_2 . From the relation above,

W_{SiO_2} and W_{TiO_2} were calculated to be 0.064 and 0.23. Therefore, the amount of TiO_2 deposition was about 4 times larger than that of SiO_2 in the SiO_2/TiO_2 nanofibers.

Figure 3 shows the XRD patterns of the SiO_2 and the SiO_2/TiO_2 nanofibers obtained after calcination at various temperatures. Although no apparent crystalline peaks were observed in the SiO_2 nanofibers after calcination at 500°C and in the SiO_2/TiO_2 nanofibers after calcination up to 400°C, the crystalline peaks assigned to anatase TiO_2 (JCPDS card no. 71-1167) were observed in the SiO_2/TiO_2 nanofibers obtained after calcination of the temperature between 450°C and 800°C. The peak widths of anatase were decreasing with increasing temperature, which indicated the growth of crystallites. It is well known that the transition from the anatase to the rutile phase in TiO_2 (JCPDS card no. 73-2224) typically occurs at less than 700°C [9]. The requirement of a higher temperature (about 1000°C) for this phase transition during calcination of the TOCN/ SiO_2/TiO_2 could be associated with the suppression by Si–O–Ti bond in the SiO_2/TiO_2 nanofibers [10]. Indeed, in the case of the SiO_2/TiO_2 nanofibers at 1000°C, the XRD peaks of cristobalite SiO_2 (JCPDS card no. 82-0512) were also observed.

Figure 4 shows FT-IR spectra of TOCN/ SiO_2/TiO_2 and spectra of SiO_2 and SiO_2/TiO_2 nanofibers obtained after calcination at various temperatures. Typical peaks of amorphous SiO_2 were observed in the sample of the SiO_2 nanofibers obtained after calcination at 500°C [11]. The peaks at 1250 and 1080 cm^{-1} are attributed to Si–O–Si asymmetric stretching modes. In addition, the peaks at 800 and 457 cm^{-1} are assigned to Si–O stretching mode and Si–O–Si rocking mode, respectively. In contrast, in the case of the SiO_2/TiO_2 nanofibers, two distinct absorption peaks between 500 and 950 cm^{-1} can be observed. The peak at around 950 cm^{-1} and the broad peak between 500 and 800 cm^{-1} are assigned to Si–O–Ti stretching mode and Ti–O stretching modes, respectively [12, 13]. The presence of the Si–O–Ti peak indicates that the condensation reaction of TTIP proceeded on SiO_2 . The absorption peaks of Si–O–Si and Si–O–Ti stretching modes

were blue-shifted with increasing calcination temperature. The intensity ratios of the peak of Si–O–Ti to that of Si–O–Si were also decreasing with increasing temperature. These results indicate that the fraction of Ti that forms the Si–O–Ti linkage was decreased [14], leading to the growth of TiO₂ grain [15]. The SiO₂/TiO₂ nanofibers calcined at 1000°C had new peaks at 797 and 615 cm⁻¹. They are attributed to Si–O–Si symmetric modes of cristobalite phase [16], which is the result corresponding to the presence of cristobalite peaks in XRD. The SiO₂/TiO₂ nanofibers calcined at the temperature up to 400°C showed C–H stretching peaks of –CH₃ or –CH₂– between 3000 and 2850 cm⁻¹ [17], which indicated that organic compounds still remained in the bodies. In the following, the discussion was focused on the SiO₂/TiO₂ nanofibers after calcination at the temperature higher than or equal to 500°C which is high enough to burn out the template of TOCN.

Figure 5 shows SEM images of the TOCN, the SiO₂ nanofibers after calcination at 500°C, and the SiO₂/TiO₂ nanofibers after calcination at the temperature between 500°C and 800°C. Similar to SiO₂ nanofibers, the SiO₂/TiO₂ nanofibers calcined at 500°C retained the original structures of the TOCN (Fig. 5a-c). However, the coarsening of the structure was observed with increasing temperature (Fig. 5c-e). It is seen that this coarsening was derived from the growth of crystallites of anatase TiO₂ observed in XRD and resulted in the decrease of Si–O–Ti bond observed in FT-IR.

The TEM image of the SiO₂ and SiO₂/TiO₂ nanofibers obtained through calcination at 500°C are shown in Fig. 6. In the case of the SiO₂/TiO₂ nanofibers, the diameter is approximately 8 nm, which is thicker than that of the SiO₂ nanofibers. Furthermore, the structures of the SiO₂/TiO₂ nanofibers seem to be nanocrystals linked with a chain shape (Fig. 6b). Figure 6c shows a high-magnification TEM image of a nanocrystal in a SiO₂/TiO₂ nanofiber, with the Fast Fourier-transformed (FFT) image of Fig. 6c shown in Fig. 6d. These

results indicate that the nanocrystal has a periodicity of 0.35 nm, corresponding to the lattice spacing of anatase (101). These results are in good agreement with the results of XRD. We also have observed an element distribution map by EELS of Ti L_{2,3} and Si L_{2,3} peaks (Fig. 6e). The observation area corresponds to Fig. 6b, and the distribution of Ti and Si is shown by blue and red colors, respectively. This map reveals that the SiO₂/TiO₂ nanofibers have core/shell structures. We also found that the structures of the core and shell are amorphous SiO₂ and TiO₂ nanocrystals, respectively. These results suggest that such heterostructures could be formed by the sequential deposition of TiO₂ and SiO₂ (Fig. 1); evidently, complex mixtures of TiO₂ and SiO₂ were not formed. Due to the shell structure of nanocrystalline anatase, the SiO₂/TiO₂ nanofibers are expected to have high photocatalytic activity [18].

2.1.4 Conclusion

It was demonstrated that SiO₂/TiO₂ nanofibers can be successfully synthesized by using TEMPO-oxidized cellulose nanofibers as templates. After the combustion of the TOCN through calcination in air, the SiO₂/TiO₂ nanofibers with diameters of approximately 8 nm were obtained. The structures of the SiO₂/TiO₂ nanofibers calcined at 500°C were core/shell structures composed of amorphous SiO₂ and anatase phase TiO₂ nanocrystals. In particular, the core of SiO₂ was irregularly covered with TiO₂ nanocrystals. With increasing the calcination temperature, TiO₂ crystalline size increased. Because the SiO₂/TiO₂ nanofibers have the extremely small dimension around several nanometers, it can be expected that these nanofibers perform as highly active photocatalyst due to their high surface-to-volume ratio.

References

1. X. Chen and S. S. Mao, *Chemical Review* **107**, 2891 (2007).
2. C. F. Goodeve and J. A. Kitchener, *Transactions of the Faraday Society* **34**, 570 (1938).
3. A. Fujishima and K. Honda, *Nature* **238**, 37 (1972).
4. M. Pelaez, N. T. Nolan, S. C. Pillai, M. K. Seery, P. Falaras, A. G. Kontos, P. S.M. Dunlop, J. W.J. Hamilton, J.A. Byrne, K. O'Shea, M. H. Entezari, and D. D. Dionysiou, *Applied Catalysis B: Environmental* **125**, 331 (2012).
5. M. Gem, F. Cao, J. Huang, S. Li, Z. Chen, K.-Q. Zhang, S. S. Al-Deyab, and Y. Lai, *Journal of Materials Chemistry A* **4**, 6772 (2016).
6. S.-J. Kim, Y. K. Cho, J. Seok, N.-S. Lee, B. Son, J. W. Lee, J. M. Baik, C. Lee, Y. Lee, and M. H. Kim, *ACS Applied Materials & Interfaces* **7**, 15321 (2015).
7. K. Nakata and A. Fujishima, *Journal of Photochemistry and Photobiology C: Photochemistry Reviews* **13**, 169 (2012).
8. S. W. Sheehan, H. Noh, G. W. Brudvig, H. Cao, and C. A. Schmuttenmaer, *Journal of Physical Chemistry C* **117**, 927 (2013).
9. D. A. H. Hanaor and C. C. Sorrell, *Journal of Materials Chemistry* **46**, 855 (2011).
10. C. He, B. Tian, and J. Zhang, *Journal of Colloid and Interface Science* **344**, 382 (2010).
11. J. Wang, B. Zou, and M. A. El-Sayed, *Journal of Molecular Structure* **508**, 87 (1999).
12. C. F. Smith, R. A. Condrate, and W. E. Votava, *Applied Spectroscopy* **29**, 79 (1975).
13. Y. Zhao, C. Li, X. Liu, F. Gu, H. Jiang, W. Shao, L. Zhang, and Y. He, *Materials Letters* **61**, 79 (2007).
14. A. N. Murashkevich, A. S. Lavitskaya, T. I. Barannikova, and I. M. Zharskii, *Journal of Applied Spectroscopy* **75**, 730 (2008).
15. A. Prison, A. Mohsine, P. Marchot, B. Michaux, O. V. Cantfort, and J. P. Pirard, *Journal of*

Sol-Gel Science and Technology **4**, 179 (1995) .

16. K. S. Finnie, J. G. Thompson, and R. L. Withers, *Journal of Physics and Chemistry Solids* **55**, 23 (1994).
17. H. A. Szymanski, *Interpreted Infrared Spectra*, (Springer US, 1967).
18. J. Zhang, P. Zhou, J. Liu, and J. Yu, *Physical Chemistry Chemical Physics* **16**, 20832 (2014).

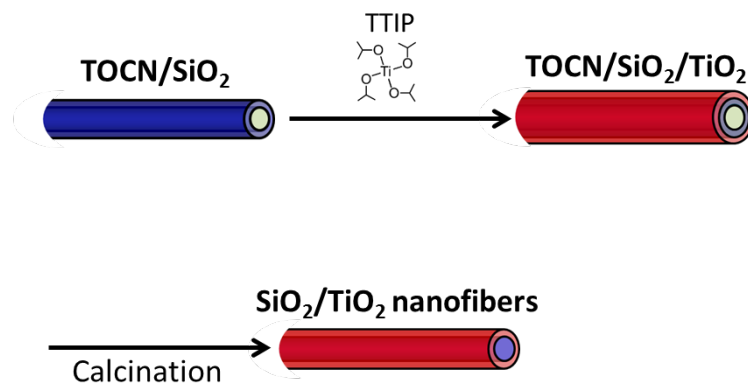


Fig. 1 Schematic procedure for synthesis of SiO₂/TiO₂ nanofibers.

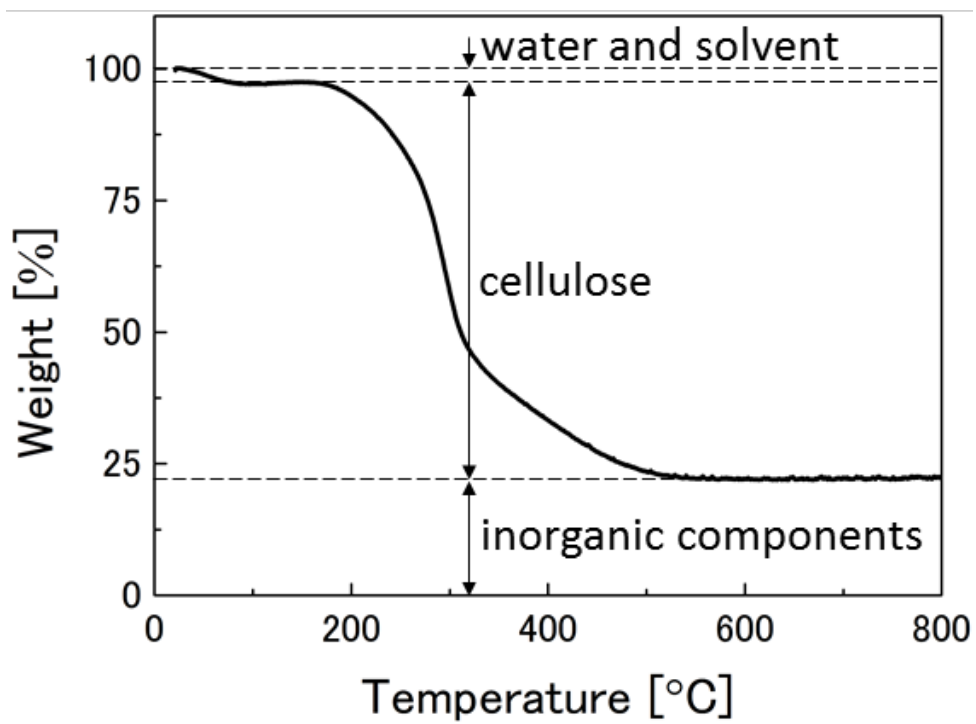


Fig. 2 Thermogravimetry curve of TOCN/SiO₂/TiO₂.

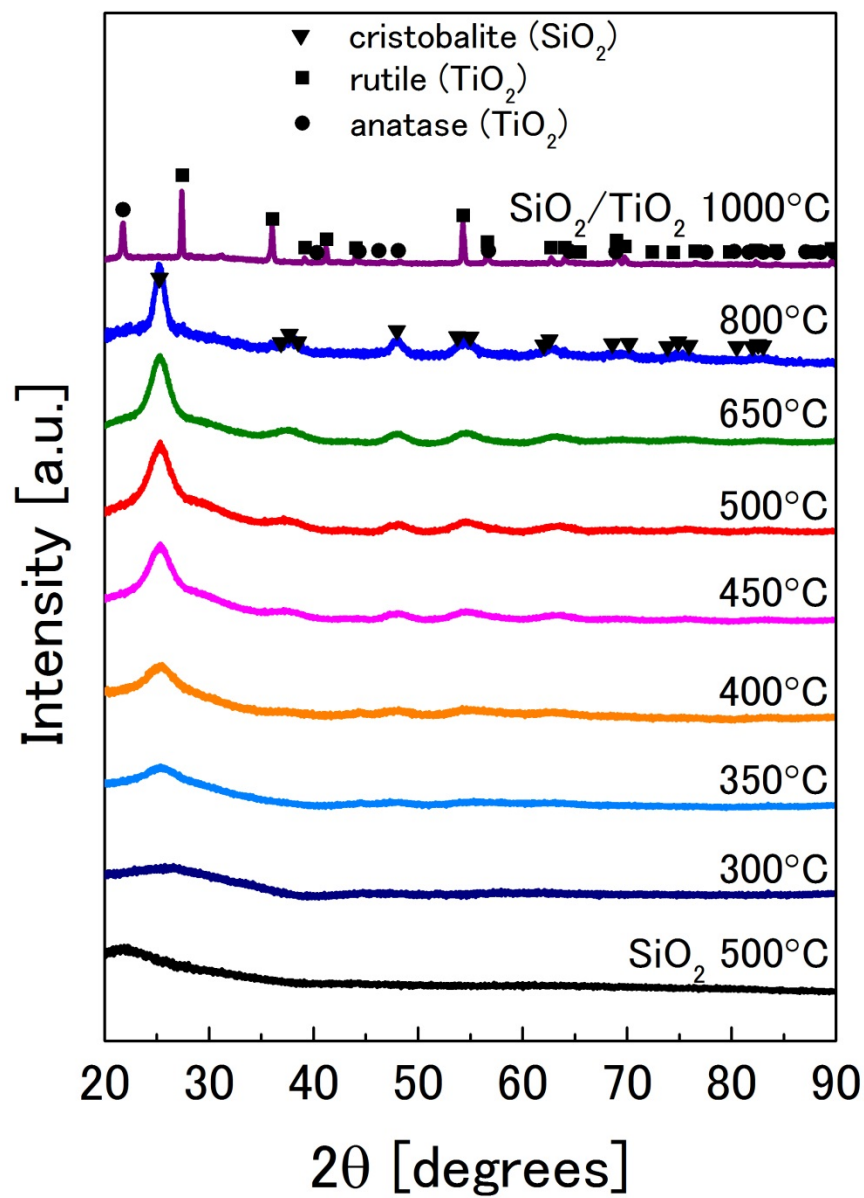


Fig. 3 XRD patterns of SiO_2 nanofibers and $\text{SiO}_2/\text{TiO}_2$ nanofibers.

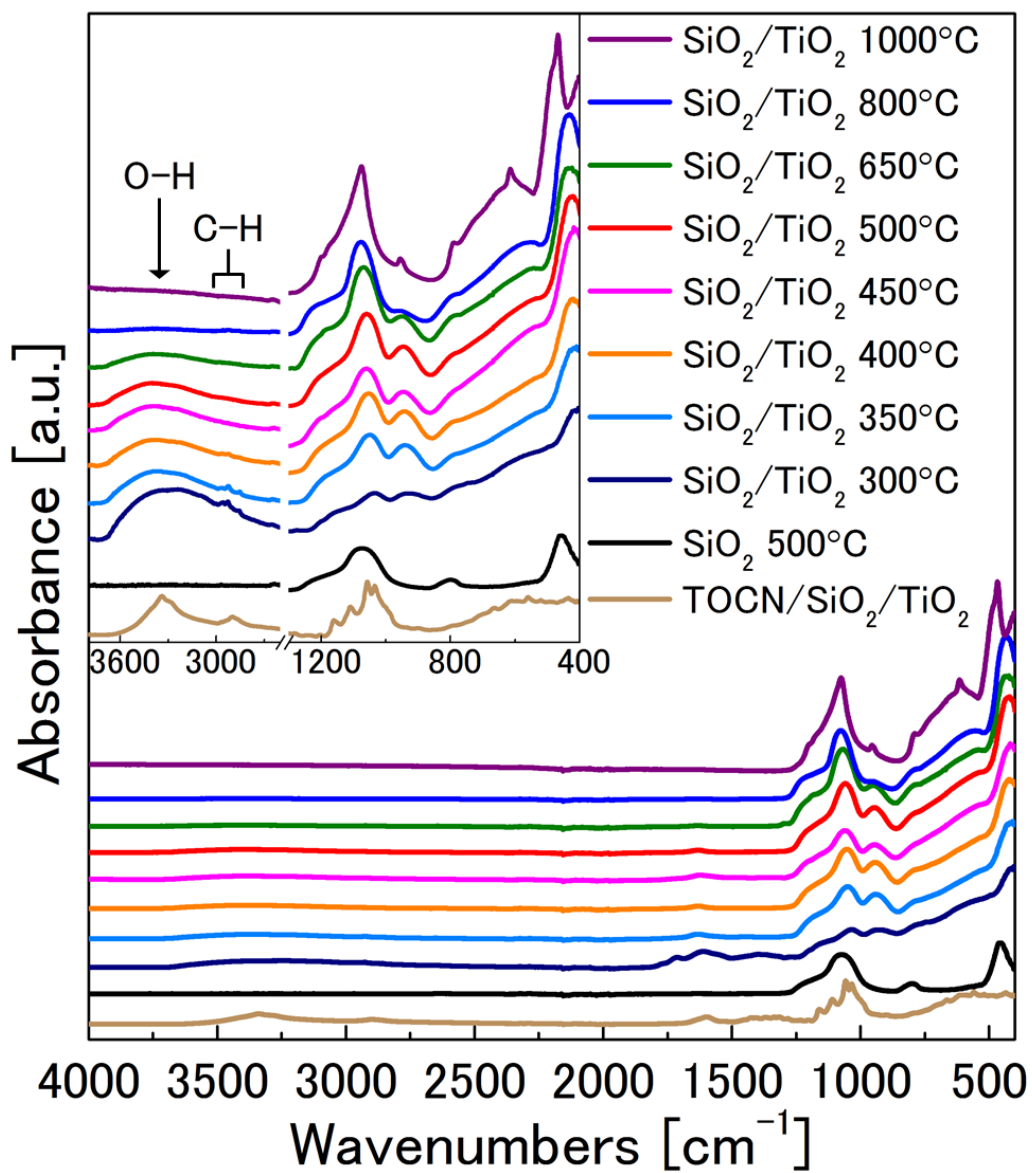


Fig. 4 FT-IR spectra of TOCN/SiO₂/TiO₂ and FT-IR spectra of SiO₂ nanofibers and SiO₂/TiO₂ nanofibers.

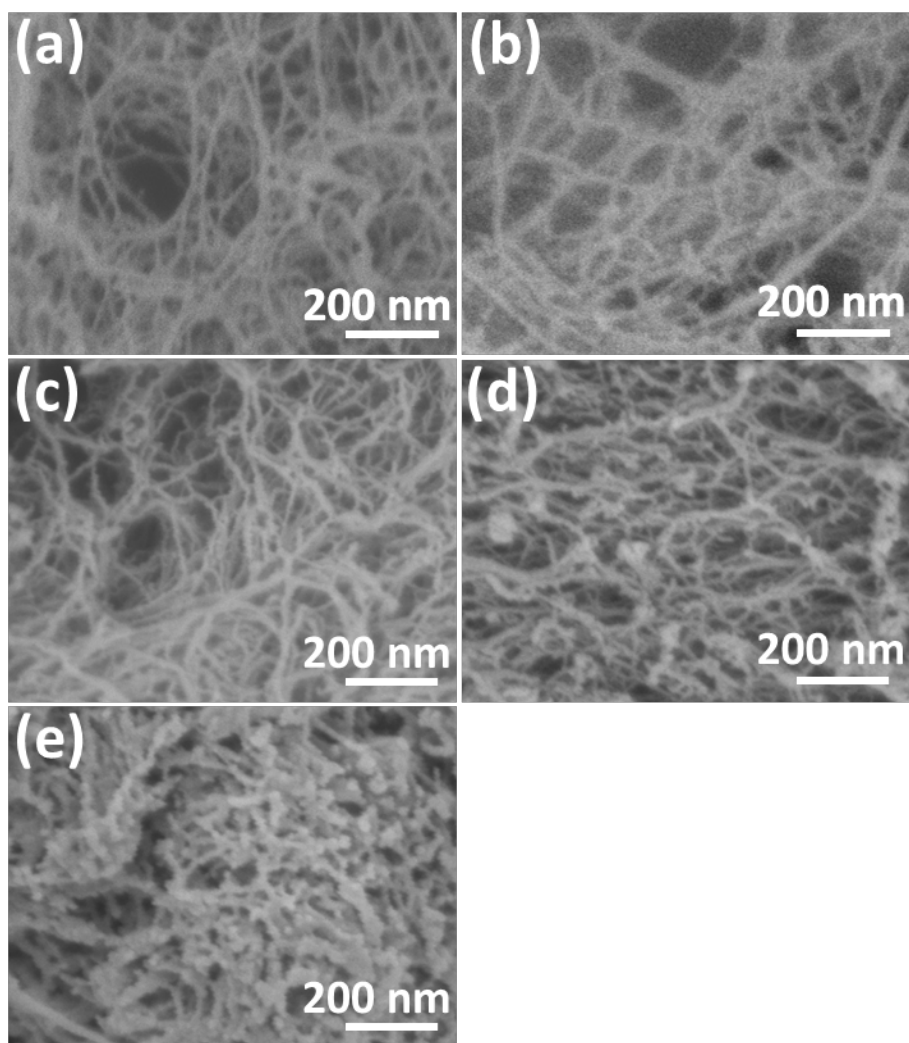


Fig. 5 FE-SEM images of **a** TOCN, **b** SiO₂ nanofibers after calcination of TOCN/SiO₂ at 500°C, **c-e** SiO₂/TiO₂ nanofibers after calcination of TOCN/SiO₂/TiO₂ at 500, 650, and 800°C, respectively.

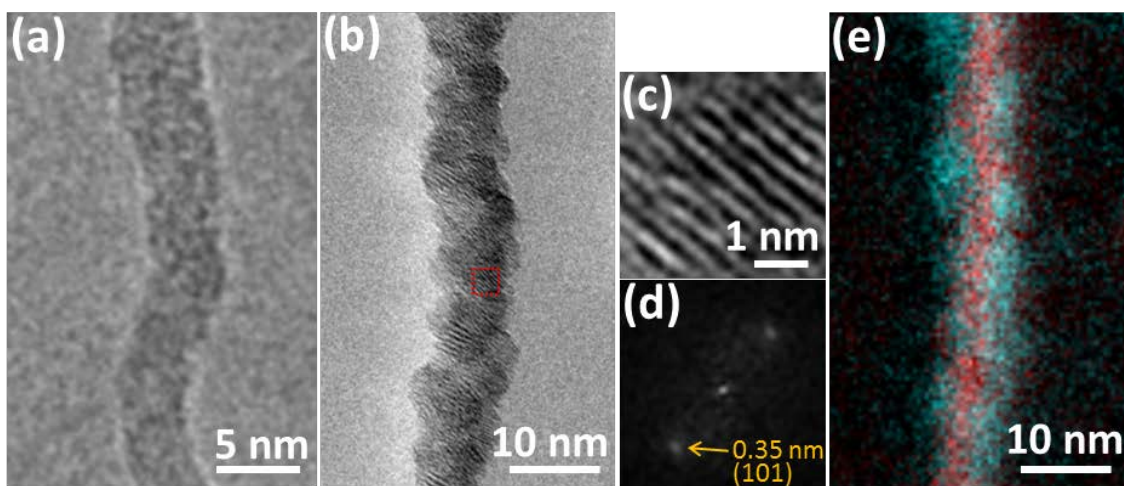


Fig. 6 TEM images of **a** SiO₂ nanofibers after calcination of TOCN/SiO₂ at 500°C, **b** SiO₂/TiO₂ nanofiber after calcination of TOCN/SiO₂/TiO₂ at 500°C, **c** high magnified image of dotted area in **b**. FFT image of **c** is also shown in **d**. **e** EELS elementary map corresponding to **b**. Blue and red colors indicate presence of Ti and Si elements, respectively.

2.2 Photocatalytic properties of SiO₂/TiO₂ nanofibers toward model organic pollutant of methylene blue

2.2.1 Introduction

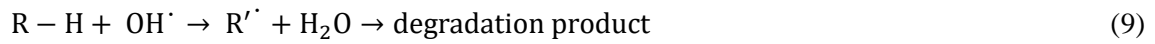
The shortage of clean water is an important issue worldwide. In order to overcome this large problem, water purification technologies with high efficiency and low cost is been studying eagerly over several decades. One of the most promising methods is “Advanced Oxidation Processes (AOPs)” as the innovative water treatment technologies. During the treatment water with AOPs, once generated highly reactive radicals such as OH radical (OH[•]) degrade organic pollutants in water. Among AOPs, photocatalytic degradation with semiconductor catalysts (TiO₂, ZnO, Fe₂O₃, CdS, and ZnS) is powerful one. In particular, most of the attention focuses on TiO₂ which is most active under the UV irradiation ranging from 300 to 390 nm and is non-toxic, cost effective, mechanically and chemically stable [2]. In general, it can be explained that photocatalytic degradation in aqueous condition proceeds by oxidizing adsorbed contaminants under the presence of dissolved oxygen. Overall reactions can be written as follows [3]:

Photoexcitation:

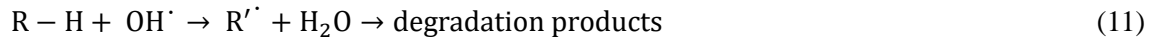


Degradation from oxygen and electron:





Degradation from hole:



The schematic of photocatalytic degradation is shown in Fig. 1. As noted above, the photocatalytic degradation of organic pollutants is largely attributed to hydroxyl radicals and holes. As reported in the previous section, SiO₂/TiO₂ core-shell nanofibers, which had diameters of approximately 8 nm, were composed of the core of amorphous SiO₂ and the shell of anatase TiO₂ nanocrystals. Because of a highly loose state and extremely small dimension, it was expected that the SiO₂/TiO₂ nanofibers are expected to perform as highly active photocatalyst for the water purification. To estimate the photocatalytic properties of the SiO₂/TiO₂ nanofibers, the photocatalytic degradation of methylene blue (MB) as a model pollutant was carried out in aqueous condition. The reference materials of porous TiO₂ particle with a similar specific surface area were used for the comparison to the synthesized SiO₂/TiO₂ nanofibers. In terms of optical, structural, and electrostatic properties, the photocatalytic properties in each sample were

researched. Furthermore, the detailed kinetics of degradation and the recyclability were also investigated

2.2.2 Experimental procedure

2.2.2.1 Reference sample of porous TiO₂ particles

For the comparison to SiO₂/TiO₂ nanofibers in the latter photocatalytic degradation test, a reference sample of porous TiO₂ particles with similar specific surface area was prepared by solvothermal synthesis [4]. A mixture of 1.0 mL TTIP and 30 mL acetone (Kishida Chemicals) was stirred for 30 min and poured into a Teflon-lined autoclave. After heating the mixture at 170°C for 12 h under autogenous pressure, the obtained precipitate was repeatedly washed with acetone using centrifugation and dried at 70°C for 12 h in air. The dried precipitate was calcined at 400°C for 4 h in air to remove organic residue.

2.2.2.2 Characterization

FT-IR spectra were measured by an FT-IR spectrometer equipped with an ATR accessory (Spectrum Two, Perkin Elmer). Microscopic structures were observed by a field-emission scanning electron microscope (FE-SEM; JSM-6700F, JEOL). X-Ray diffraction (XRD) patterns were measured by an X-Ray diffractometer (RINT-2500HFK, Rigaku) using CuK α radiation. Crystallite sizes are also estimated by Scherrer equation [5]. BET specific surface area [6] was characterized by using an N₂ adsorption-desorption apparatus (Tristar 3000, Shimadzu). Before the measurements of specific surface area, the sample was degassed at 150°C for 24 h under vacuum. UV-Vis absorbance spectra were obtained by the Kubelka-Munk transformation from diffuse reflectance spectra on a spectrophotometer (V-570, JASCO) with an integrating sphere.

Zeta potential was analyzed by a zeta potential analyzer (ELSZ-2Plus, Otsuka Electronics) with a pH titrator system.

2.2.2.3 Estimation of photocatalytic activity

The photocatalytic activity of the synthesized $\text{SiO}_2/\text{TiO}_2$ nanofibers and the reference sample of the porous TiO_2 particles were estimated by the degradation of methylene blue (MB, Wako Pure Chemicals). 1.0 mg of the $\text{SiO}_2/\text{TiO}_2$ nanofibers calcined at the various temperature or the porous TiO_2 particles was dispersed in 4.0 mL of 15 mg/L MB aqueous solution by sonication, and then stirred in the dark for 1 h which was sufficient time for adsorption equilibrium. After the suspension was transferred to a quartz glass cell, in order to avoid the intrinsic absorption of MB, light with a wavelength ranging from 300 to 500 nm through the short path filter (B390, HOYA) was irradiated by using a metal halide lamp. The light intensity and the irradiation time were 200 W/cm^2 and 360 min respectively. After irradiation for a certain time, 1 mL of the suspension was sampled and centrifuged. The absorbance spectrum of the supernatant was measured by a spectrometer (USB2000, Ocean optics) and the concentration of MB was then determined by the absorbance at 664 nm. After the measurement, for successive UV irradiation, the supernatant and precipitation were mixed again by sonication, and then the suspension was brought back to the quartz glass cell.

The formation of OH radicals in the suspension was detected by the photoluminescence method using terephthalic acid as probe molecule [7]. 1.0 mg of the $\text{SiO}_2/\text{TiO}_2$ nanofibers or the porous TiO_2 particles was dispersed in 4.0 mL of the mixture of 0.1 M terephthalic acid and 0.01 M NaOH aqueous solution and then stirred in the dark for 1 hour. After that, light irradiation was carried out by using a metal halide lamp with the same irradiation conditions in the photocatalytic degradation of MB. After irradiation for a certain time, 1 mL of the

suspension was sampled and centrifuged. The photoluminescence intensity of the reaction product, 2-hydroxy-terephthalic acid, was measured at 426 nm by a fluorescence spectrometer (Fluoromax-3, Horiba Jobin Yvon) with 312 nm excitation. To characterize more detailed photocatalytic activity, the relationship between the degradation rate and the concentration of MB was investigated for a certain sample.

The recyclability was also characterized. When the certain cycle of photocatalytic degradation of MB was finished, a sample was repeatedly washed with distilled water several times and dispersed again in 15 mg/mL of MB aqueous solution. Light was irradiated after the adsorption equilibrium of MB.

2.2.3 Results and discussion

Figure 2 shows the XRD, FT-IR and FE-SEM results of the synthesized reference porous TiO₂ sample. These porous nanoparticles were composed of anatase TiO₂ phase (Fig. 2a, b) (JCPDS card no. 71-1167) [8]. It was revealed that these particles had spherical shape which was constructed with a lot of anatase TiO₂ nanocrystals with many pores (Fig. 2c, d). The crystallite size of anatase TiO₂ of the SiO₂/TiO₂ nanofibers and porous the TiO₂ particles was estimated by Scherrer equation using the (101) peaks (Table 1). As described in the previous section, the adequate calcination temperature of the SiO₂/TiO₂ nanofibers to burn out the template of TOCN and to bring enough crystallinity of TiO₂ for photocatalytic activity is equal to or higher than 500°C.

Figure 3a shows the UV-Vis absorbance spectra of the SiO₂/TiO₂ nanofibers and reference sample of porous TiO₂ particles. The SiO₂/TiO₂ nanofibers had the absorption edge shorter in wavelength than the reference sample of porous TiO₂ particles. Furthermore, apparent differences in the slope of the curves ranging from 320 to 360 nm were observed. It is known

that the composite material of SiO₂ and TiO₂ shows relatively smaller absorbance than the simple body of TiO₂ [9]. With increasing calcination temperature, the absorption edge of the SiO₂/TiO₂ nanofibers was slightly red-shifted. Since the crystallite sizes of the anatase phase in the SiO₂/TiO₂ nanofibers are small, this result could be interpreted in terms of the quantum size effect [10]. The anatase phase with a smaller crystallite size formed through lower calcination temperature indicated a wider band gap leading to a shorter optical absorption edge. The band gap energy of anatase TiO₂, which is an indirect semiconductor, was estimated from absorbance spectra (Fig. 3b) [10]:

$$\alpha = \frac{B_i(h\nu - E_g)^2}{h\nu} \quad (13)$$

$$(\alpha h\nu)^{\frac{1}{2}} \propto (h\nu - E_g) \quad (14)$$

where α is the optical absorbance, $h\nu$ is photon energy, B_i is a absorption constant, and E_g is the indirect band gap energy (Table 1). The measured values of BET specific surface areas were also listed in Table 1. The value of the reference porous TiO₂ particles was similar to those of the SiO₂/TiO₂ nanofibers. When the calcination temperature was increased, the crystallite sizes increased from 3.9 to 8.0 nm and the specific surface area decreased from 158 to 103 m²/g. The changes in these values indicate the growth of the TiO₂ grain corresponding to the blue shift of Si–O–Ti peaks as shown in the previous section.

Figure 4 shows the experimental schematic of photocatalytic degradation of methylene blue (MB). The concentration of MB was calculated by the measured optical coefficient of MB at 664 nm using the linear relation (Fig. 5). Curves of the attenuation of MB concentration versus light irradiation time are plotted in Fig. 6. The MB concentration was normalized by the

concentration after adsorption equilibrium in dark. The SiO₂/TiO₂ nanofibers calcined at the temperature below 500°C exhibited relative slow attenuation because of lower crystallinities (Fig. 6a) [11]. As mentioned above, the discussion will be focused on the SiO₂/TiO₂ nanofibers calcined at the temperature higher than or equal to 500°C. The adsorbed amount of MB after equilibrium was listed in Table 1. The photocatalytic degradation of an organic pollutant can be commonly described by the Langmuir-Hinshelwood model [12, 13]. A pollutant, which is adsorbed following Langmuir isotherm, is degraded on the surface of a photocatalyst. The degradation rate equation can be expressed as follows:

$$r = -\frac{dC}{dt} = \frac{k_r K C}{1 + K C} \approx k_r K C = k_{app} C \quad (15)$$

$$\frac{C}{C_{eq}} = e^{-k_{app} t} \quad (16)$$

where r is the rate of the degradation of MB, k_r is the true constant of reaction rate, K is the adsorption constant of MB, k_{app} is the apparent first-order degradation rate, C is the concentration of MB, and C_{eq} is the concentration of MB after adsorption equilibrium. r is approximated by $k_{app} C$ in the case that C is low. In our report, the attenuation curves of MB concentration decreased exponentially (Fig. 6b), which enable us to deal the degradation reaction as an apparent first order reaction and compare the photocatalytic abilities of each sample by their k_{app} , simply. Hence, although the adsorbed amount of MB is different in each sample, the intrinsic kinetics must be little affected by the concentration of MB after the adsorption equilibrium. The values of k_{app} were calculated by the attenuation curves and were also listed in Table 1. Compared to the degradation of MB without any sample, those of every sample were higher. Furthermore, the k_{app} for the SiO₂/TiO₂ nanofibers were higher than that

for the reference porous TiO₂ particles, in spite of the lower optical absorbance of the SiO₂/TiO₂ nanofibers (Fig. 3). The higher photocatalytic activities for the SiO₂/TiO₂ nanofibers calcined at each temperature could be caused by the high adsorbability of MB (Table 1).

In experiments, the pH value of the MB aqueous solution became 5.2 in the applied concentration. Around this pH value, the zeta potential of the SiO₂/TiO₂ nanofibers calcined at various temperatures was largely negative and similar to amorphous SiO₂ nanoparticles (Sigma-Aldrich), however that of the reference sample of porous TiO₂ particles was positive (Fig. 7) owing to the lower pH value than the isoelectric point of anatase phase TiO₂ nanoparticles [14]. This result reveals the difference in the adsorption abilities between the SiO₂/TiO₂ nanofibers and the porous TiO₂ particles, implying a contradiction with the zeta potential of SiO₂ covered with TiO₂ [15]. Indeed, in the case of the SiO₂/TiO₂ nanofiber calcined at 500°C, the core of SiO₂ was irregularly covered with TiO₂ nanocrystals as shown in the previous section. Accordingly, SiO₂ was partially exposed to the surface of the SiO₂/TiO₂ nanofibers and played an important role in the photocatalytic degradation. It is supposed that the same goes for the SiO₂/TiO₂ nanofibers calcined at 650°C and 800°C.

It is known that MB is degraded by active oxygen species such as OH radicals produced on the surface of photoexcited TiO₂ [12, 16]. The production of OH radicals by the SiO₂/TiO₂ nanofibers was lower than that by the porous TiO₂ particles (Fig. 8), because of the less surface of TiO₂ due to the exposure of SiO₂ and less optical absorbance. In spite of lower production of OH radicals in the SiO₂/TiO₂ nanofibers, active oxygen species could easily attack on MB adsorbed on SiO₂ because of the closeness to SiO₂ from TiO₂, leading to the efficient degradation [17-20]. As a result, the SiO₂/TiO₂ nanofibers showed high photocatalytic activity for cationic pollutants such as MB. It should be noted that the lower specific surface area caused by the higher calcination temperature of the SiO₂/TiO₂ nanofibers can realize the lower

photocatalytic activity. Furthermore, the dramatic decrease of k_{app} in the SiO₂/TiO₂ nanofibers calcined at the temperature from 650°C to 800°C could also reflect the huge grain growth of TiO₂ as shown in the previous section. That grain growth brought the large distance between activated oxygen species on TiO₂ and adsorbed MB on SiO₂, which reduced the efficiency of the degradation.

The recycling test was conducted and the SiO₂/TiO₂ nanofibers calcined at 500°C showed the good recyclability (Fig. 9). Slight deteriorations seem to be caused by material loss through the washing using centrifugation. As mentioned above, the photocatalytic degradation follows the Langmuir-Hinshelwood model. The linear form of Langmuir-Hinshelwood gives following equation:

$$\frac{1}{r_0} = \frac{1}{k_r} + \frac{1}{k_r K} \frac{1}{C_{eq}} \quad (17)$$

where r_0 is the initial rate of the degradation of MB. The plot of $1/r_0$ on the $1/C_{eq}$ after the results of photocatalytic degradation of different initial MB concentration was linearly represented for the SiO₂/TiO₂ nanofibers calcined at 500°C (Fig. 10). The k_r and K was calculated from the slope and the intercept were 0.085 mgL⁻¹min⁻¹ and 0.94 mg⁻¹L, respectively.

2.2.4 Conclusion

In this chapter, by using methylene blue (MB) as a model pollutant, the photocatalytic degradation properties of SiO₂/TiO₂ nanofibers are reported. The reference samples of porous TiO₂ particles with similar specific surface area were used for comparison. In spite of lower optical absorption and lower generation of OH radicals, SiO₂/TiO₂ nanofibers performed much faster degradation than porous TiO₂ particles. This result could be attributed to partially exposed

SiO₂. In applied aqueous solution, SiO₂ possesses negative charge and adsorb the MB as a cationic pollutant electrostatically. The adsorbed MB became spatially close photocatalytic site of TiO₂, leading to efficient degradation. It was found out that the material system of complexing SiO₂ with functional oxides is promising and can be diverted into wider range of disciplines relevant to surface phenomena.

References

1. Y. Deng and R. Zhao, *Current Pollution Reports* **1**, 167 (2016).
2. M. N. Chong, B. Jin, C. W. K. Chow, and C. Saint, *Water Research* **44**, 2997 (2010).
3. U. I. Gaya and A. H. Abdullah, *Journal of Photochemistry and Photobiology C: Photochemistry Reviews* **9**, 1 (2008).
4. B. Liu, L. Liu, X. Lang, H. Wang, X. W. Lou, and E. S. Aydil, *Energy & Environmental Science* **7**, 2592 (2014).
5. A. L. Patterson, *Physical Review* **56**, 978 (1939).
6. S. Brunauer, P. H. Emmett, and E. Teller, *Journal of the American Chemical Society* **60**, 309 (1938).
7. T. Hirakawa and Y. Nosaka, *Langmuir* **18**, 3247 (2002).
8. Y. Zhao Y, C. Li, X. Liu, and F. Gu, *Materials Letters* **61**, 79 (2007).
9. S. Hu, F. Li, and Z. Fan, *Bulletin of the Korean Chemical Society* **33**, 1895 (2012).
10. H. Lin, C. P. Huang, W. Li, C. Ni, S. I. Shah, and Y. Tseng, *Applied Catalysis B: Environmental* **68**, 1 (2006).
11. K. Tanaka, M. F. V. Capule, and T. Hisanaga, *Chemical Physics Letters* **187**, 73 (1991).
12. A. Houas, H. Lachheb, M. Ksibi, E. Elaloui, C. Guillard, and J. M. Herrmann, *Applied Catalysis B: Environmental* **31**, 145 (2001).
13. C. S. Turchi and D. F. Ollis, *Journal of Catalysis* **122**, 178 (1990).
14. K. Suttiponpanit, J. Jiang, M. Sahu, S. Suvachittanont, T. Charinpanitkul, and P. Biswas, *Nanoscale Research Letters* **6**, 27 (2011).
15. J. Lee, S. Kong, W. Kim, and J. Kim, *Materials Chemistry and Physics* **106**, 39 (2007).
16. S. Lakshmi, R. Renganathan, and S. Fujita, *Journal of Photochemistry and Photobiology A: Chemistry* **88**, 163 (1995).

17. L. Melone, L. Altomare, I. Alfieri, A. Lorenzi, L. D. Nardo, and C. Punta, *Journal of Photochemistry and Photobiology A: Chemistry* **261**, 53 (2013).
18. C. He, B. Tian, and J. Zhang, *Journal of Colloid and Interface Science* **344**, 382 (2010).
19. F. Chen, J. Zhao, and H. Hidaka, *International Journal of Photoenergy* **5**, 209 (2003).
20. M. V. Liga, S. J. Maguire-Boyle, J. Jafry, A. R. Barron, Q. Li, *Environmental Science & Technology* **47**, 6463 (2013).

Table 1 Crystallite size, indirect band gap, BET specific surface area, adsorbed amount of MB in dark, and apparent first order rate constant of MB degradation (k_{app}) of SiO₂/TiO₂ nanofibers and reference sample of porous TiO₂ particles.

	Crystallite size [nm]	Band gap [eV]	BET specific surface area [m ² /g]	MB adsorbed in dark [mg/g]	k_{app} [1/min]
SiO ₂ /TiO ₂ 800°C	8.0	3.31	103	27	5.4×10^{-3}
SiO ₂ /TiO ₂ 650°C	4.4	3.35	107	36	1.1×10^{-2}
SiO ₂ /TiO ₂ 500°C	3.9	3.36	158	37	1.2×10^{-2}
porous TiO ₂ particles	9.4	3.29	138	1.3	1.9×10^{-3}

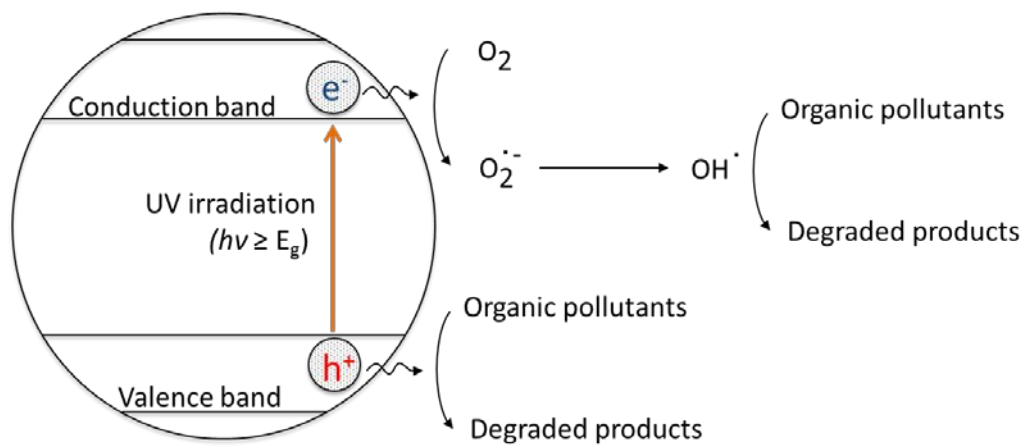


Fig. 1 Schematic diagram of photocatalytic degradation of organic pollutants.

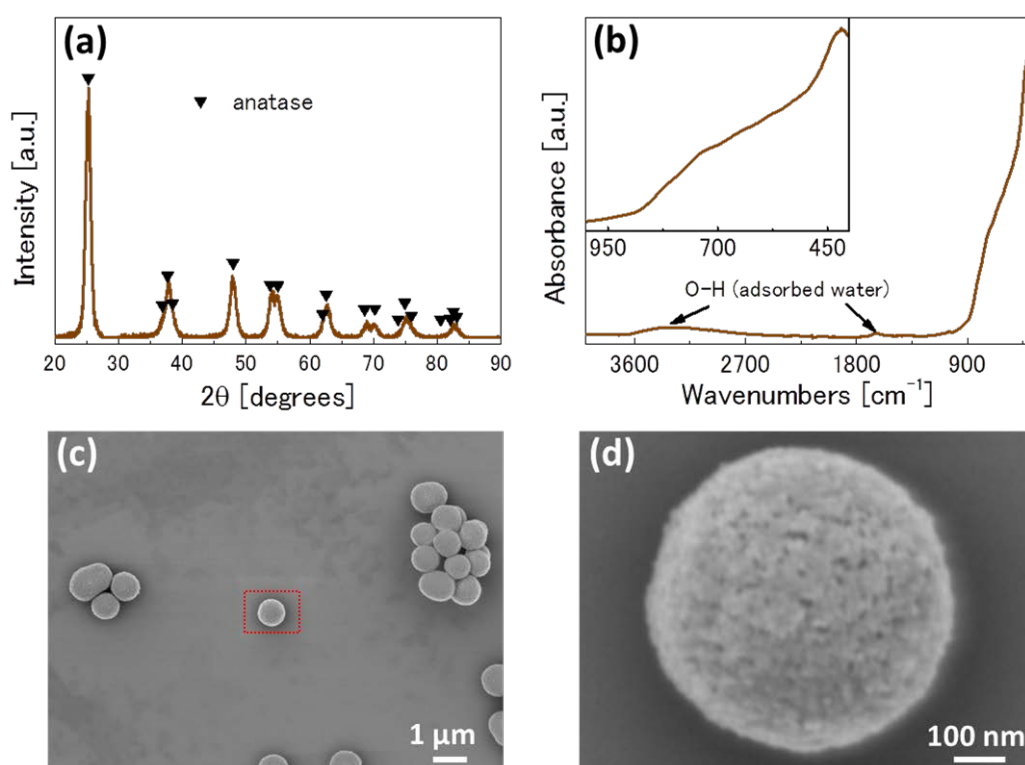


Fig. 2 **a** XRD pattern, **b** FT-IR spectrum, and **c** FE-SEM image of porous TiO₂ particles. **d** is high-magnified image of dotted area in **c**.

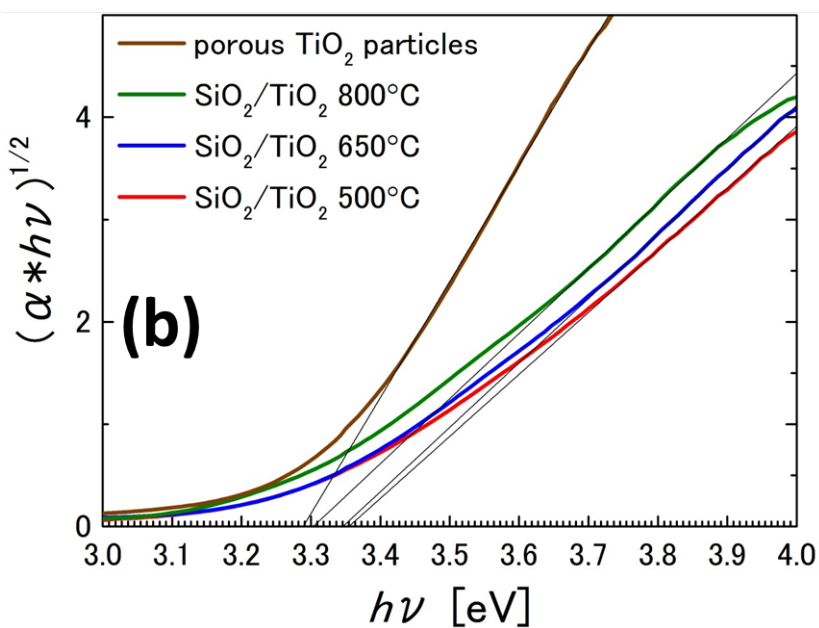
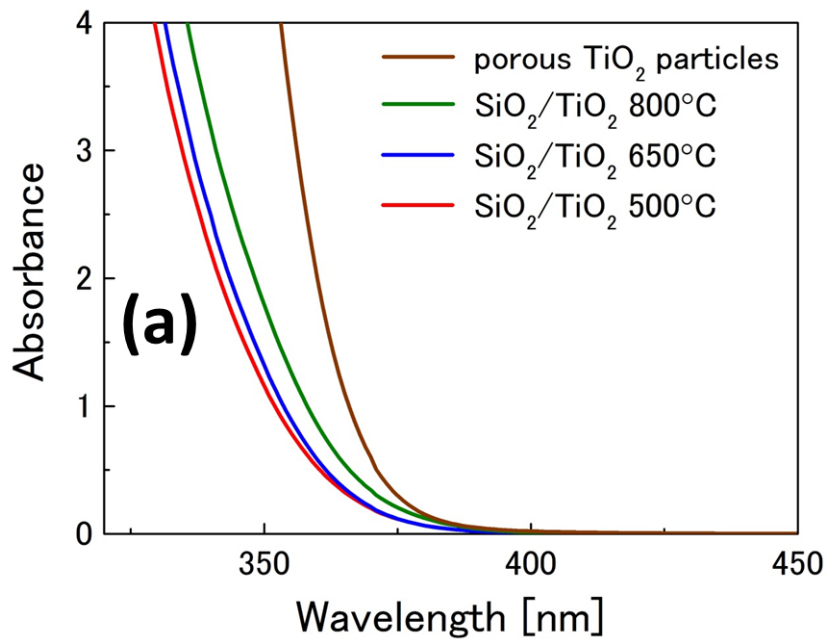


Fig. 3 a UV-Vis absorbance spectra of porous TiO₂ particles and SiO₂/TiO₂ nanofibers.
b Plots of $(\alpha h\nu)^{1/2}$ versus $h\nu$ for determination of band gap

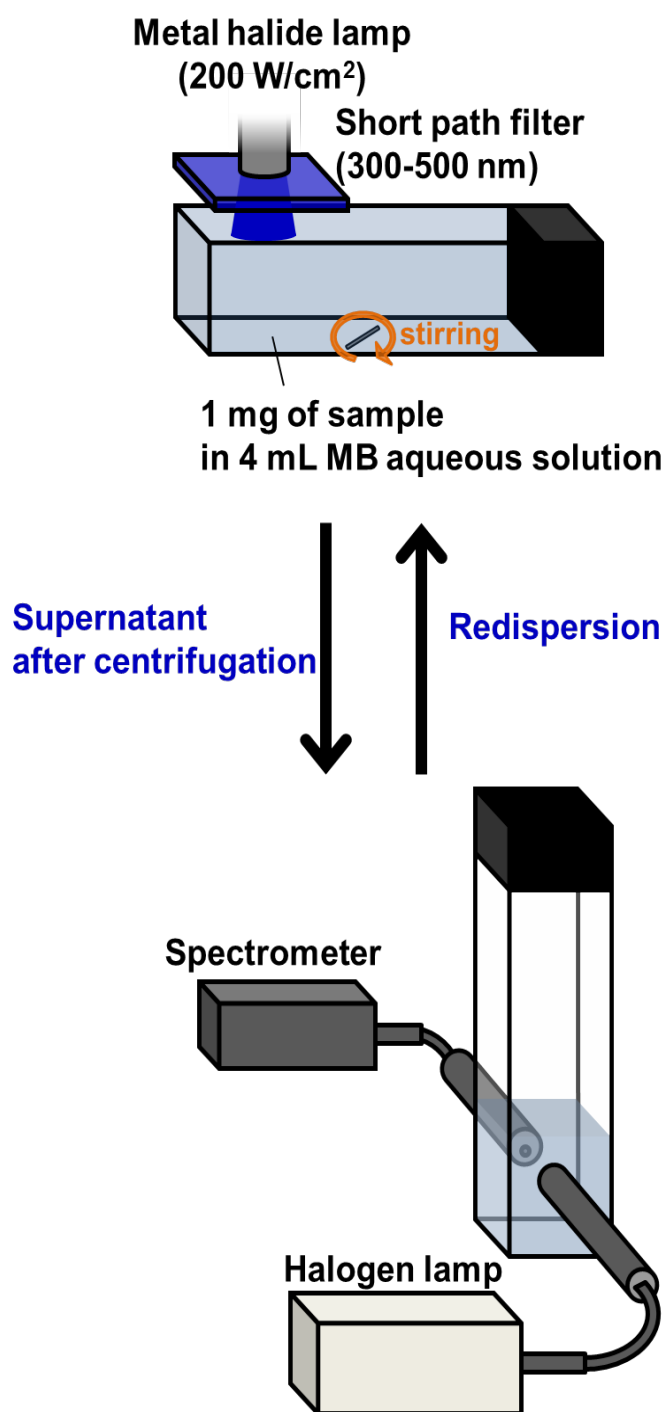


Fig. 4 Schematic of experimental setup for photocatalytic degradation of MB.

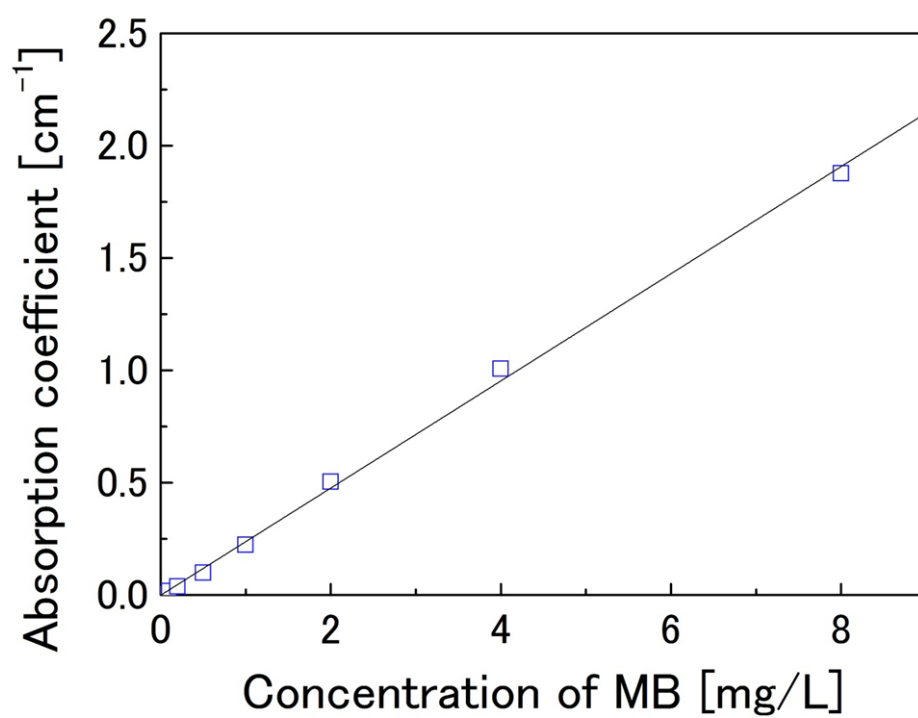


Fig. 5 Linear relationship between concentration of methylene blue (MB) and optical absorption coefficient at 664 nm ($R^2 = 0.9984$).

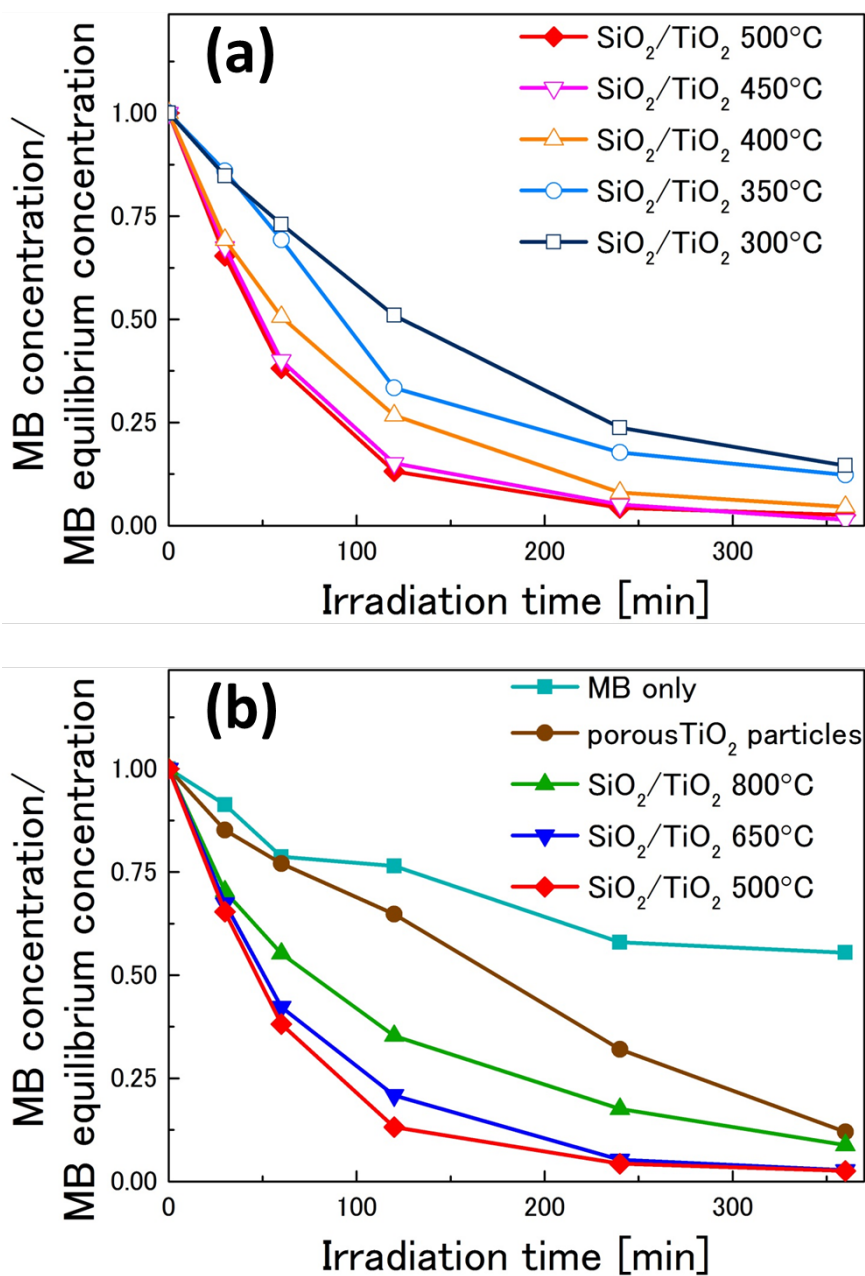


Fig. 6 Degradation of methylene blue (MB) under irradiation of a metal halide lamp **a** with SiO₂/TiO₂ nanofibers calcined at temperature between 300°C and 500°C, **b** with SiO₂/TiO₂ nanofibers calcined at temperature between 500°C and 800°C or porous TiO₂ particles. Degradation of MB without any photocatalytic sample is also shown in **b**.

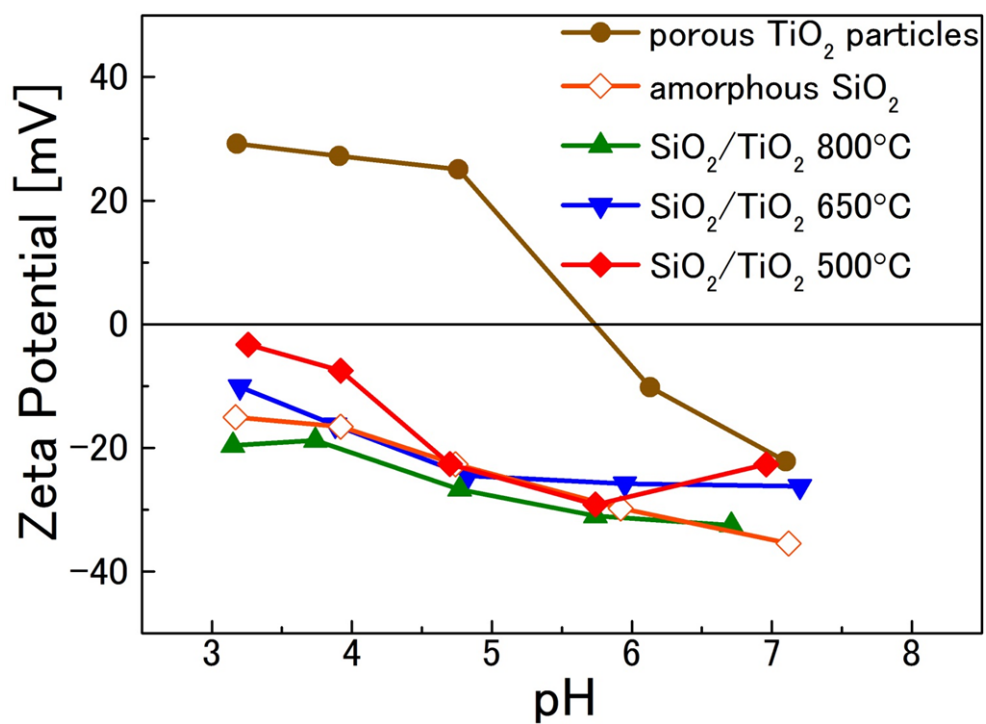


Fig. 7 Zeta potential of porous TiO₂ particles, amorphous SiO₂ nanoparticles, and SiO₂/TiO₂ nanofibers calcined at temperature between 500 °C and 800°C at various pH values.

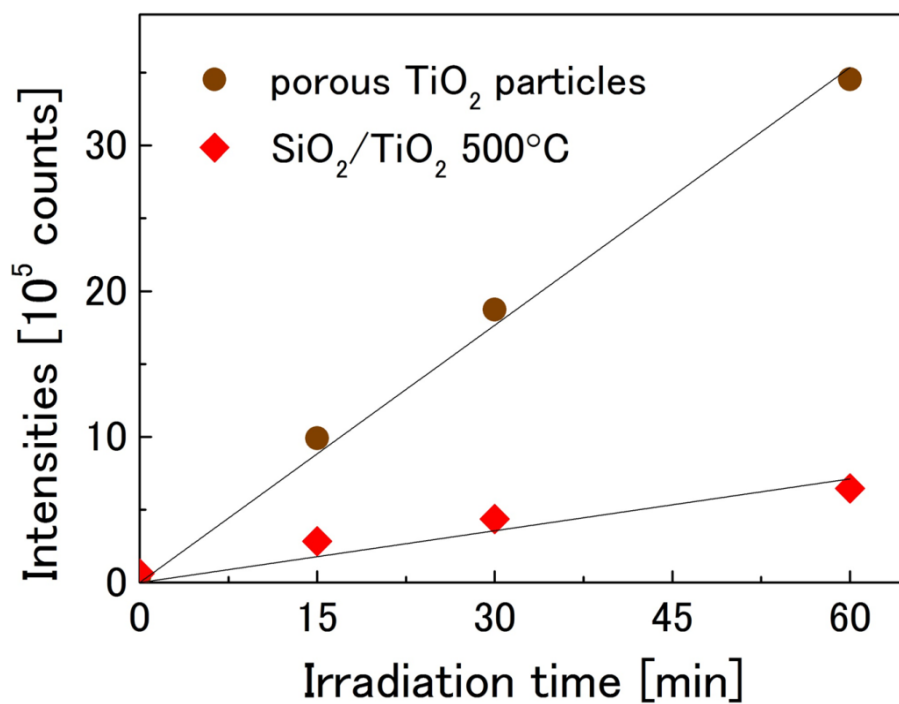


Fig. 8 Hydroxyl radical production monitored by photoluminescence intensity of 2-hydroxy-terephthalic acid.

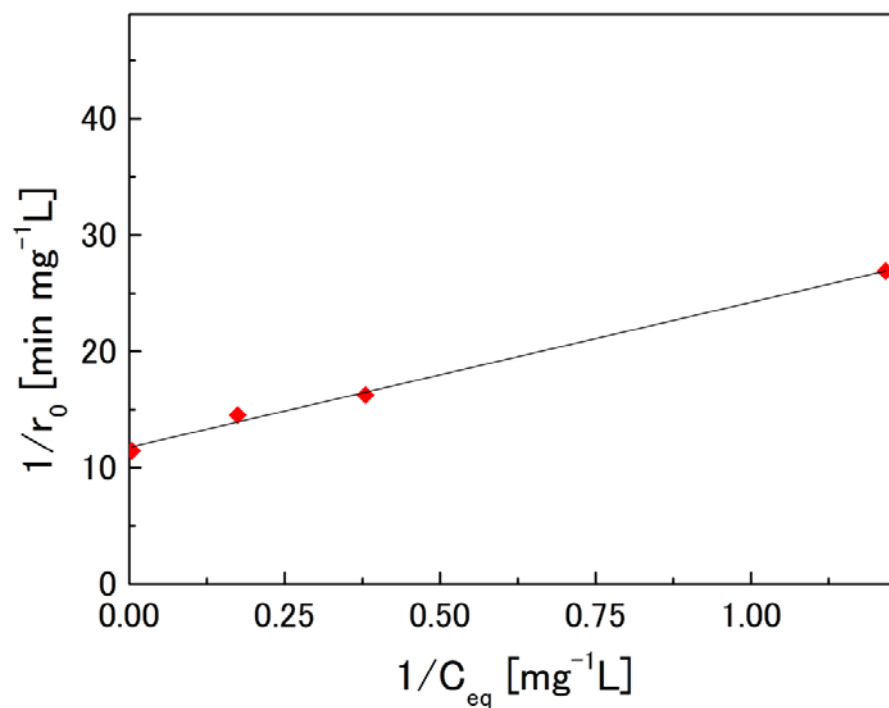


Fig. 9 Initial photocatalytic degradation rate as function of MB equilibrium concentration with SiO₂/TiO₂ nanofibers calcined at 500°C.

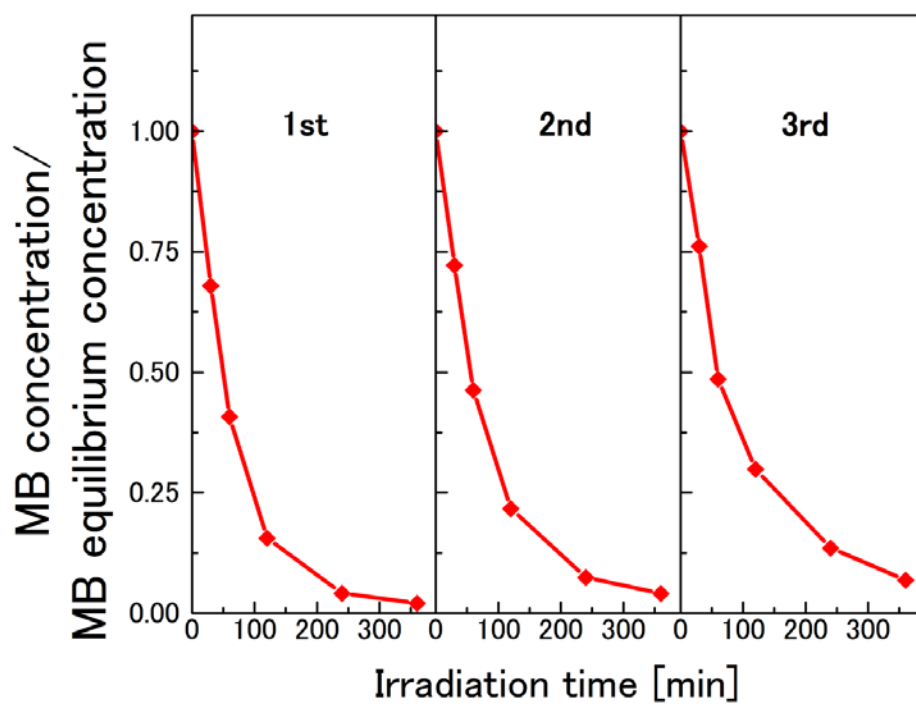


Fig. 10 Recyclability of SiO₂/TiO₂ nanofibers calcined at 500°C for MB photocatalytic degradation.

Chapter 3

Synthesis and gas sensing properties of SiO₂/SnO₂ nanofibers using TOCN as templates

3.1 Synthesis of SiO₂/SnO₂ nanofibers using TOCN as templates and effect of acetylacetone to stabilize Sn precursor

3.1.1 Introduction

SnO₂, which is an n-type wide band gap semiconductor, is attractive material because of its transparency, catalytic property, semiconductivity as reviewed before [1, 2]. Therefore, they applied for many uses, for examples, transparent electrodes [3], Li-ion batteries [4], oxidative catalysts [5], and gas sensors [6, 7]. The unique surface phenomenon of SnO₂, which is utilized for the catalyst and gas sensor, is derived from its dual valency which means the reversible transformation between Sn⁴⁺ and Sn²⁺ at the surface [1, 2].

From a perspective of the application for gas sensor, 1D nanostructures can indicate beneficial effects such as good gas diffusivities [8] and long-term durabilities [9], resulting in superior gas sensing materials. Moreover, it is well known that SnO₂ with a lower crystallite size brings a higher sensitivity as a gas sensor [10, 11]. Thus, the controlling the dimension is one of the most effective ways for designing SnO₂ nanomaterials.

Generally in sol-gel process, the reactivity of metal alkoxides is suppressed by stabilizing agents such as carboxyl acid, polyalcohol, and β -diketone [12-14]. Particularly in terms of the synthesis of SnO₂ nanoparticles, it was reported that several stabilizers (e.g. tetraethylene glycol, benzoylacetone, acetylacetone) were effective to avoid coarsened structures and to obtain small crystallites [15-17].

Here, the synthesis of SiO₂/SnO₂ nanofibers was reported with diameters of approximately 10 nm using TOCN as template. In the experiment, the TOCN covered with SiO₂ (in the following, TOCN/SiO₂) was used as starting materials. The additional deposition of SnO₂ was carried out by sol-gel reactions using tin (IV) isopropoxide via the formation of covalent Si-O-Sn bond. In some synthesis conditions, acetylacetonone, which is one of β -diketone, was used as a stabilizer to form less reactive tin acetylacetonate in the deposition process. After the deposition, TOCN/SiO₂ coated with SnO₂ were calcined in air to burn out the TOCN and then as-deposited SnO₂ was simultaneously crystallized, leading to SiO₂/SnO₂ core-shell nanofibers composed of the core of amorphous SiO₂ and the shell of rutile SnO₂ nanocrystals. The structural differences which reflected the synthesis procedures were investigated.

3.1.2 Experimental procedure

3.1.2.1 Synthesis of SiO₂/SnO₂ nanofibers

To deposit SnO₂ onto the TOCN/SiO₂ surface, the hydrolysis and condensation reactions of tin alkoxide were employed. Certain amount of acetylacetonone (acac, Kishida Chemicals), 3.06 mL of 28% NH₃ aqueous solution (Kishida Chemicals) were added to ethanol dispersion containing 0.128 g of TOCN/SiO₂. After the further dilution with ethanol and addition of 0.928 mL of 10w/v% tin (IV) isopropoxide in isopropanol (Alfa Aesar), the mixture was stirred for 12 h at room temperature under an argon atmosphere. In the exceptional cases, distilled water was used instead of NH₃ aqueous solution with maintaining the total amount of water. The amount of ethanol for the dilution was modified to make the total weight of the mixture 128 g. Acac/Sn molar ratios were changed from 0 to 1000. After washing repeatedly by isopropanol (Kishida Chemicals) using centrifugation at 4000 rpm, TOCN/SiO₂ covered with SnO₂ were dried with a super critical dryer (SCRD 4, Rexam) using CO₂. SiO₂/SnO₂ nanofibers were obtained after

calcination of the dried sample at temperatures between 500°C and 800°C for 4 h in air via the combustion of the templates TOCN.

3.1.2.2 Characterization

Measurements of X-Ray diffraction (XRD) patterns were carried out by an X-Ray diffractometer (RINT-2500HFK, Rigaku). The crystallite size of SnO₂ was calculated by Scherrer's equation [18] with rutile SnO₂ (101) peak. Observations of microscopic structures were conducted by a field-emission scanning electron microscope (FE-SEM; JSM-6700F, JEOL), a transmission electron microscope (TEM; JEM-2200FS, JEOL), and a scanning transmission electron microscope (STEM; JEM-ARM₂00F, JEOL) with an energy-dispersive X-ray spectrometer (EDS; JED-2300T, JEOL). FT-IR spectra were measured by an FT-IR spectrometer equipped with an ATR accessory (Spectrum Two, Perkin Elmer). Thermogravimetry measurements were carried out in air using a thermogravimetric thermal analyzer (TG8120, Rigaku). BET specific surface areas [19] were determined by using an N₂ adsorption-desorption apparatus (Tristar 3000, Shimadzu) after degassing at 150°C. X-ray photoelectron spectroscopy (XPS) measurements were performed on XPS microprobe spectrometer (PHI 5000 Versa Probe II, Ulvac-Phi). All XPS spectra were calibrated using a C 1s peak which is assumed at 284.8 eV [20]. In some cases, the commercial nanoparticles such as SnO₂ nanoparticles (Sigma-Aldrich) and SiO₂ nanoparticles (Sigma-Aldrich) were also analyzed for comparison.

3.1.3 Results and discussion

Figure 1 shows the synthesis procedure of the SiO₂/SnO₂ nanofibers schematically. Figure 2 shows XRD patterns of SiO₂ and SiO₂/SnO₂ nanofibers synthesized with various acac/Sn molar

ratios and successively calcined at 500°C. All SiO₂/SnO₂ nanofibers had rutile phase SnO₂ (JCPDS card no. 41-1445), in contrast to no crystalline peaks in SiO₂. Inset denotes the relationship between acac/Sn ratios and crystallite sizes. It should be noted that the SiO₂/SnO₂ nanofibers obtained by the acac/Sn ratio of 500 shows the smallest crystallite size of 3.2 nm. In the exceptional cases without NH₃, the crystallite sizes remained still high.

Figure 3 shows FE-SEM images of TOCN, SiO₂ nanofibers, and SiO₂/SnO₂ nanofibers with various acac/Sn ratios. The SiO₂/SnO₂ nanofibers with the acac/Sn ratio of 500 maintained the fine structure derived from TOCN, however, the considerably coarse grains were obtained in other conditions. These coarsening are corresponding to the large crystallite sizes in the inset of Fig. 2. From these results, it was revealed that the use of NH₃ and appropriate amount of acac can suppress the undesirable large grains. The generation of such coarse grains would be interpreted as follows; since a homogeneous nucleation via a self-condensation of tin isopropoxide occurred, these nuclei grew and then attached onto the surface of the nanofibers. Here the effect of acac can be explained by the formation of tin acetylacetonate. Such tin acetylacetonate, which is less reactive than tin alkoxide [16, 17], suppressed self-condensation and finally caused the selective deposition on the nanofibers surface. In this study, since the formation of acetylacetonate occurred at the same time as the hydrolysis of tin isopropoxide, much more amount of acac compared to the stoichiometric acac/Sn molar ratio, which is up to 2, was required. It is assumed that the basicity of NH₃ helped the formation of tin acetylacetonate through the deprotonation of acac [21]. On the other hand, it is expected that NH₃ also acted as base for the dissolution of small nuclei derived from the self-condensation. Since acac is weak acid, the too much amount as acac/Sn ratio of 1000 caused the insufficiency of basicity for the dissolution of nuclei derived from the self-condensation, leading to the coarsening of SnO₂ crystallites.

The effect of acac also could be estimated by the relationship between acac/Sn molar ratio and SnO₂/SiO₂ weight ratio (Fig. 4). When the acac/Sn ratio was 100, the deposited amount of SnO₂ was maximum value. This result can be explained by the stabilizing effect of acac due to the washing process with centrifugation. In the centrifugation with applied condition, although the nanofibers and the SnO₂ deposited on the nanofibers could be precipitated, SnO₂ nanoparticles without deposition on the nanofibers, which were originated from the homogenous nucleation, could not be precipitated. Due to the formation of stable tin acetylacetonate, the amount of the heterogeneous nuclei of SnO₂ was increased, resulting in the higher SnO₂/SiO₂ weight ratio. In the case that acac/Sn ratio was more than 100, both homogenous and heterogeneous nucleation sites were decreased, leading to the lower weight ratio of SnO₂/SiO₂.

To control the crystallite size of the deposited SnO₂, the effects of the calcination temperature were also investigated. Figure 5, 6 shows the XRD patterns and the FT-IR spectra of the SiO₂/SnO₂ nanofibers with acac/molar ratio of 500 after calcination at various temperatures. The results of the SiO₂ nanofibers calcined at 500°C were also shown. In the XRD patterns, the peaks of rutile SnO₂ in the SiO₂/SnO₂ nanofibers were sharpen according to the increase of the calcination temperature. It should be noted that no phase transition was observed in these calcination conditions (Fig. 5). The crystallite sizes calculated from peak widths were listed in Table.1. The higher temperature brought the larger crystallites sizes because of the grain growth.

In the FT-IR spectra (Fig. 6), the peaks at 1250 and 1080 cm⁻¹ are attributed to Si–O–Si asymmetric stretching modes. In addition, the peaks at 800 and 457 cm⁻¹ are assigned to Si–O stretching mode and Si–O–Si rocking mode, respectively [22]. In the case of the SiO₂/SnO₂ nanofibers, the peak at around 970 cm⁻¹ and the broad peak between 700 and 400 cm⁻¹ are

assigned to Si–O–Sn stretching mode and typical SnO₂ absorption, respectively [23, 24]. The presence of Si–O–Sn peak can be interpreted by the existence of the covalent bonding between SiO₂ and SnO₂. This Si–O–Sn peak was decreased with increasing in the calcination temperature.

In the XPS spectra of the SiO₂/SnO₂ nanofibers, the chemical shifts in binding energy of Sn 3d were observed depending on the presence of SiO₂ and the calcination temperatures (Fig. 7). It is speculated that these shifts were derived from the Si–O–Sn bond as reported in the system of SnO₂ thin film deposited on SiO₂ substrate [25]. The chemical shifts got weaker with the increasing calcination temperature, because of the decrease of Si–O–Sn bond (Fig. 6). The BET specific surface areas are shown in Table. 1. The SiO₂/SnO₂ nanofiber calcined at 500°C exhibited very high value of 322 m²/g, though those calcined at higher temperature exhibited lower value.

The FE-SEM images of the SiO₂ and the SiO₂/SnO₂ nanofibers calcined at various temperatures are shown in Fig. 8a-8d. The coarsening of the structure was observed with increasing temperature. In particular, the SiO₂/SnO₂ nanofibers calcined at 800°C indicated the large grains in the dimension of several microns. These coarsening were corresponding to the increment in the crystallite sizes of SnO₂ calculated from the XRD peaks (Fig. 5), the decrease in Si–O–Sn bond observed in the FT-IR spectra (Fig. 6), and the decrease of the BET specific surface area (Table 1). The TEM image of the SiO₂/SnO₂ nanofibers calcined at 500°C is also shown in Fig. 8e. The diameter of the SiO₂/SnO₂ nanofibers was approximately 8 nm. Figure 8f shows a high-magnification TEM image of a nanocrystal in a SiO₂/SnO₂ nanofiber, with the Fast Fourier-transformed (FFT) image of Fig. 8f shown in Fig. 8g. These results indicate that the nanocrystals have a periodicity of 0.33 nm, corresponding to the lattice spacing of (110) in rutile SnO₂. These results are also in good agreement with the results of XRD. The result of

STEM observation and its EDS element distribution map are shown in Fig. 8h and i. The observed diameter was approximately 10 nm, which was almost same as that in the TEM image. The distributions of Si and Sn are shown by red and green colors, where overlapped area is shown by yellow color. From element distribution map (Fig. 8i) and previous characterizations (Fig. 5, 6), it was revealed that the SiO₂/SnO₂ nanofibers have the core-shell structure which is composed of the amorphous SiO₂ core and the rutile SnO₂ nanocrystals shell.

Figure 9 shows the zeta potential of amorphous SiO₂ nanoparticles, SnO₂ nanoparticles, and the SiO₂/SnO₂ nanofibers calcined at 500°C. Although the SnO₂ nanoparticles showed the isoelectric between 4 and 5, the SiO₂/SnO₂ nanofibers showed the behavior as same as the SiO₂ nanoparticles. Hence, it seemed that SiO₂ in the SiO₂/SnO₂ nanofibers partially exposed at the surface in analogy with the SiO₂/TiO₂ nanofibers reported in previous chapter.

3.1.4 Conclusion

It was demonstrated that SiO₂/SnO₂ nanofibers were synthesized successfully using TEMPO-oxidized cellulose nanofibers (TOCN) as templates. After the combustion of the TOCN through calcination, the SiO₂/SnO₂ nanofibers composed of the amorphous SiO₂ core and the rutile SnO₂ shell were obtained. The detailed microscopic and crystalline structures were investigated in relation to the deposition condition of SnO₂. The key factor was the molar ratio of acac/Sn and the presence of NH₃. The optimal molar ratio of acac/Sn was 500 under the use of NH₃. Since such optimized SiO₂/SnO₂ nanofibers keep the fine structure derived from TOCN, it is expected that the crystallite size is controllable. Indeed, the synthesized nanofibers had very thin diameters of approximately 10 nm and the smallest crystallite size of rutile SnO₂ was to be 3.2 nm. As a result, it can be expected that the SiO₂/SnO₂ nanofibers exhibit high sensitivity to several gaseous species because of the very small crystallites.

References

1. M. Batzill and U. Diebold, *Progress in Surface Science* **79**, 47 (2005).
2. S. Das and V Jayaraman, *Progress in Materials Science* **66**, 112 (2014).
3. Z. M. Jarzebski and J. P. Marton, *Journal of the Electrochemical Society* **123**, 333C (1976).
4. D. Deng, M. G. Kim, J. Y. lee, and J. Chao, *Energy & Environmental Science* **2**, 818 (2009).
5. M. J. Fuller and M. E. Warwick, *Journal of Catalysis* **29**, 441 (1973).
6. N. Barsan, M. S.-Berberich, and W. Göpel, *Fresenius' Journal of Analytical Chemistry* **365**, 287 (1999).
7. T. Sahn, A. Gurlo, N. Barsan, and U. Weimer, *Sensors and Actuators B* **118**, 78 (2006).
8. D.-J. Yang, I. Kamienchick, D. Y. Youn, A. Rothschild, and I.-D. Kim, *Advanced Functional Materials* **20**, 4258 (2010).
9. V. V. Sysoev, T. Schneider, J. Goschnick, I. Kiselev, W. Habicht, H. Hahn, E. Strelcov, and A. Kolmakov, *Sensors and Actuators B* **139**, 699 (2009).
10. C. N. Xu, J. Tamaki, N. Miura, and N. Yamazoe, *Sensors and Actuators B* **3**, 147 (1991).
11. N. Yamazoe and K. Shimano, *Journal of the Electrochemical Society* **155**, J93 (2008).
12. G. Yi and M. Sayer, *Journal of Sol-Gel Science and Technology* **6**, 75 (1996).
13. M. B. González, A. Wu, and P. M. Vilarinho, *Chemistry of Materials* **18**, 1737 (2006).
14. A. E. Danks, S. R. Hall, and Z. Schnepp, *Materials Horizons* **3**, 91 (2016).
15. M. Yuasa, K. Suematsu, K. Yamada, K. Watanabe, T. Kida, N. Yamazoe, and K. Shimano, *Crystal Growth & Design* **16**, 4203 (2016).
16. M. J. H.-Smith, T. A. Wark, C. J. Brinker, *Coordination Chemistry Reviews* **112**, 81 (1992).
17. S. Monredon, A. Cellot, F. Ribot, C. Sanchez, L. Armelao, L. Gueneau, and L. Delattre, *Journal of Materials Chemistry* **12**, 2396 (2002).

18. A. L. Patterson, *Physical Review* **56**, 978 (1939).
19. S. Brunauer, P. H. Emmett, and E. Teller, *Journal of the American Chemical Society* **60**, 309 (1938).
20. D. Barreca, S. Garon, E. Tondello, and P. Zanella, *Surface Science Spectra* **7**, 81 (2000).
21. M. Seco, *Journal of Chemical Education* **66**, 779 (1989).
22. J. Wang, B. Zou, and M. A. E.-Sayed, *Journal of Molecular Structure* **508**, 87 (1999).
23. P. Shah, A. V. Ramaswamy, K. Lazar, and V. Ramaswamy, *Applied Catalysis A General* **273**, 239 (2004).
24. D. Amalric-Popescu and F. Bozon-Verduraz, *Catalysis Today* **70**, 139 (2001).
25. V. M. Jiménez, J. A. Mejías, J. P. Espinós, and A. R. González-Elipe, *Surface Science* **366**, 545 (1996).

Table 1 Crystallite size and BET specific surface area of SiO₂/SnO₂ nanofibers with acac/Sn molar ratio of 500 and calcined at various temperatures.

Calcination temperature [°C]	Crystallite size [nm]	BET specific surface area [m ² /g]
800°C	22	139
650°C	12	174
500°C	3.2	322

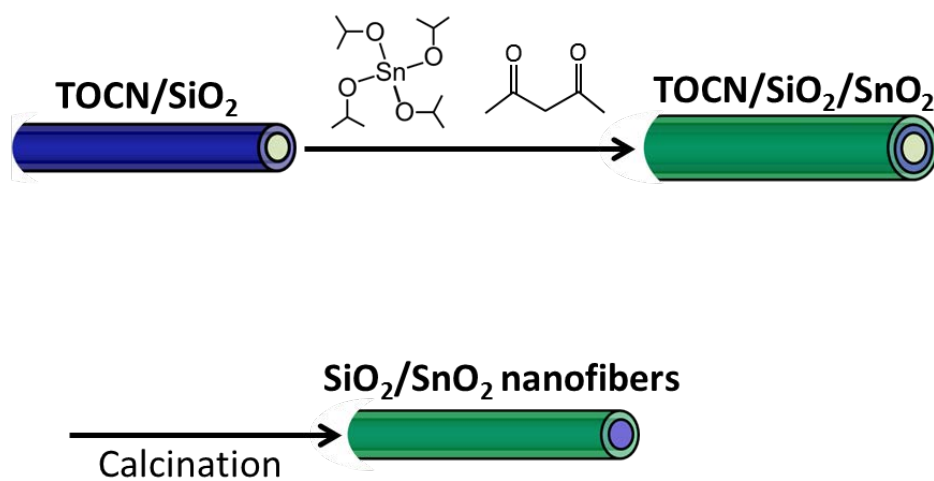


Fig. 1 Schematic procedure for synthesis of $\text{SiO}_2/\text{SnO}_2$ nanofibers.

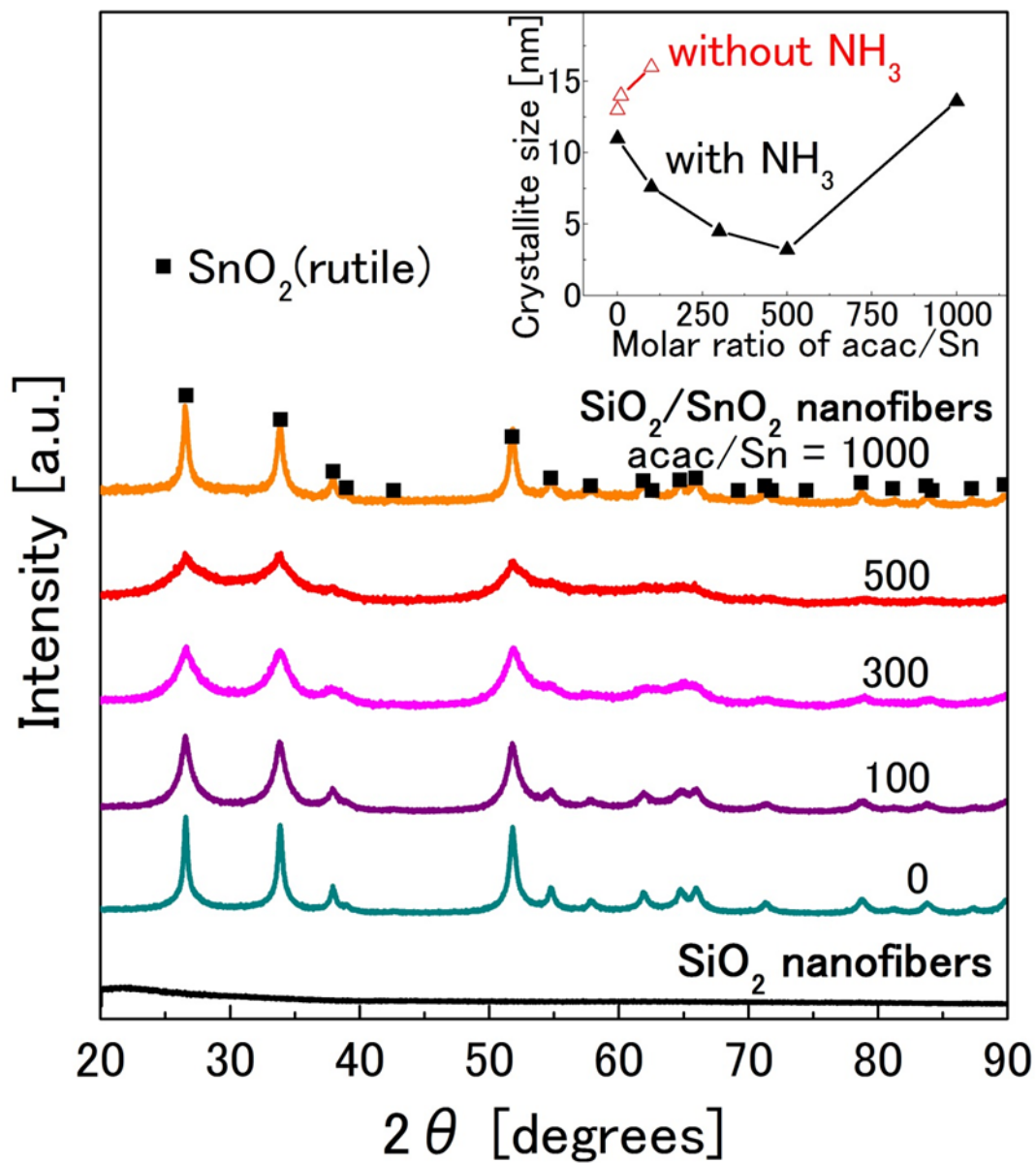


Fig. 2 XRD patterns of SiO₂ and SiO₂/SnO₂ nanofibers synthesized with various acac/Sn molar ratios. All samples were calcined at 500°C. Inset plot indicate relationship between acac/Sn molar ratios and crystallite size of SnO₂. Red-colored plots indicate results of SiO₂/SnO₂ nanofibers without use of NH₃ as exceptional cases.

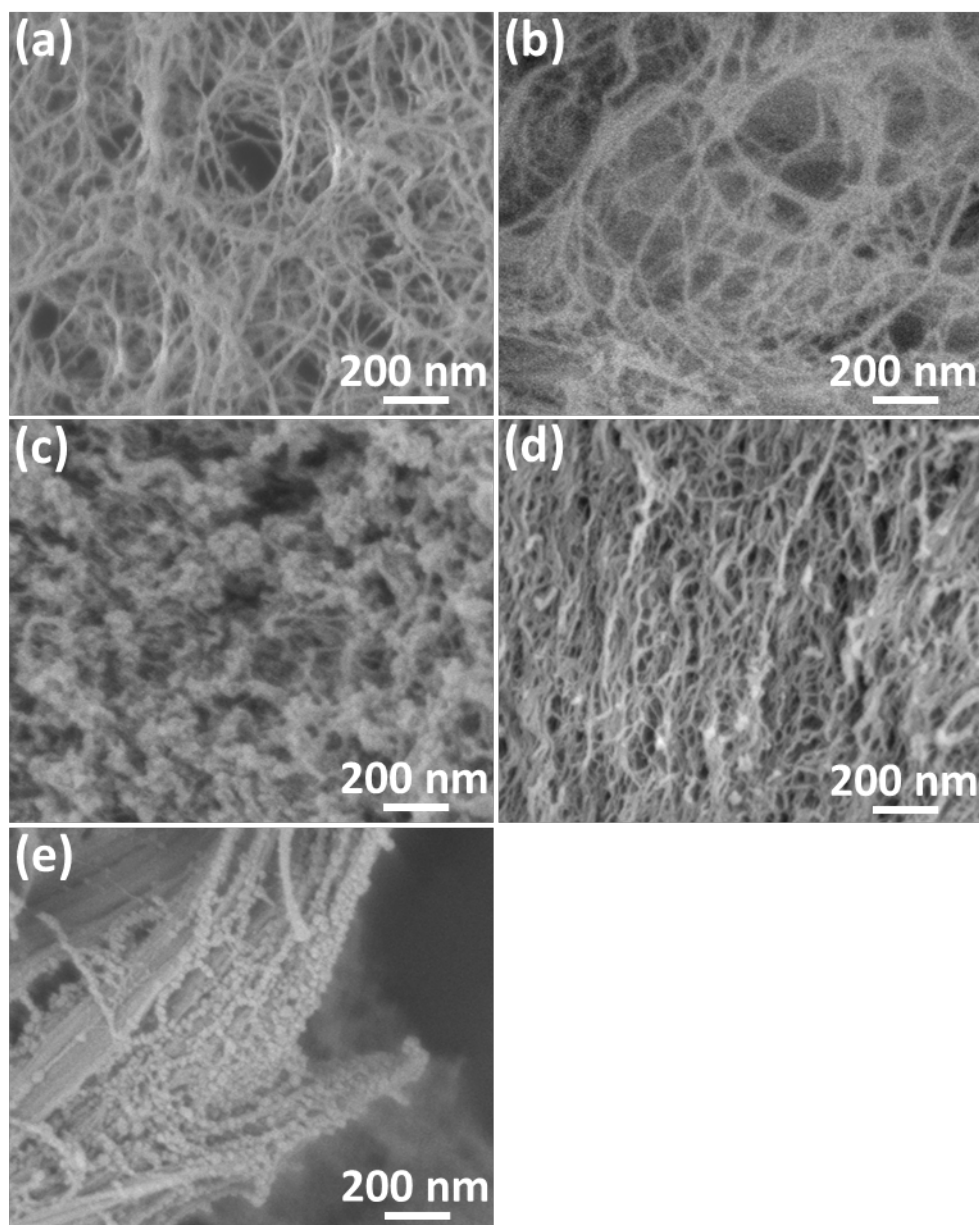


Fig. 3 FE-SEM images of **a** TOCN, **b** SiO₂ nanofibers, **c-e** SiO₂/SnO₂ nanofibers synthesized with acac/Sn molar ratio of 0, 500, and 1000, respectively. All samples except for TOCN were calcined at 500°C.

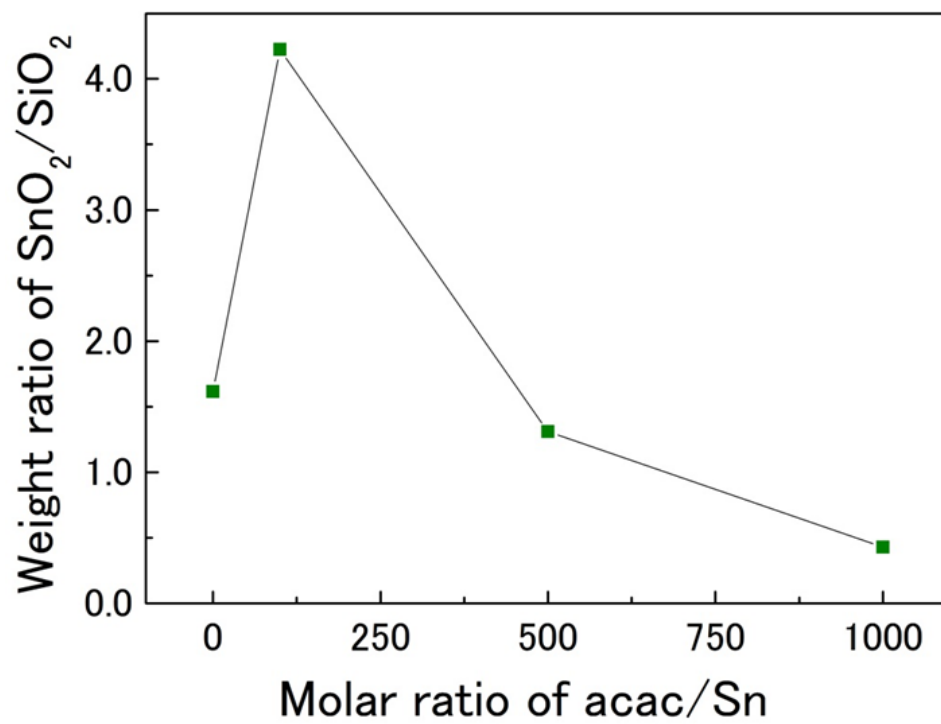


Fig. 4 Plots of weight ratios of SnO₂ to SiO₂ in SiO₂/SnO₂ nanofibers synthesized with various acac/Sn molar ratios.

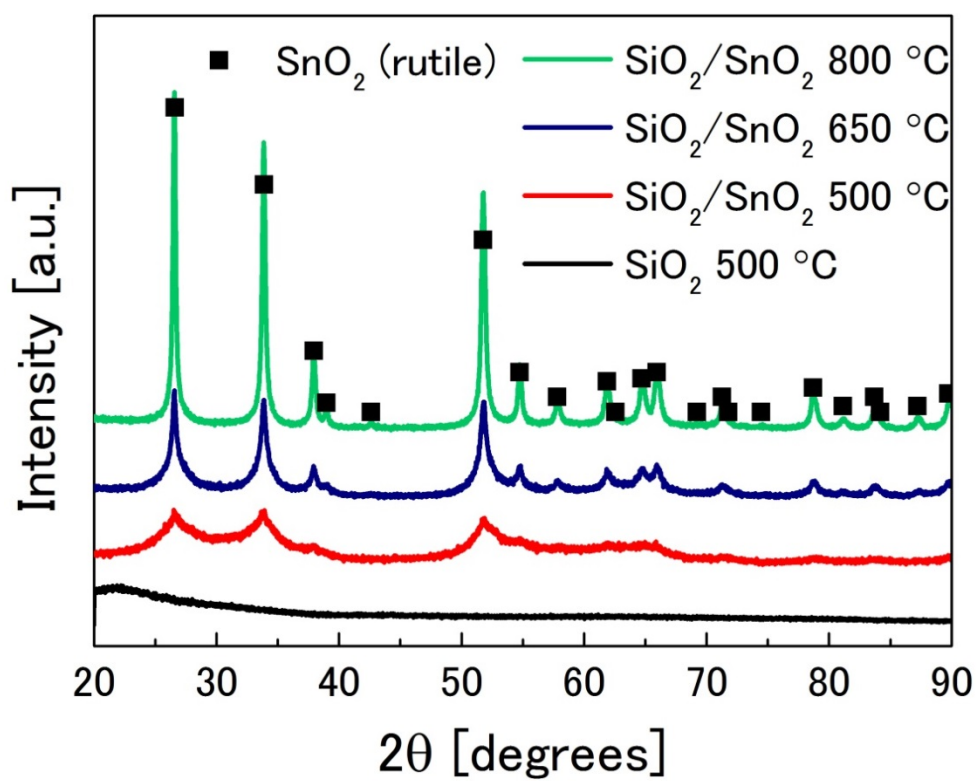


Fig. 6 XRD patterns of SiO₂ nanofibers calcined at 500°C and SiO₂/SnO₂ nanofibers synthesized with acac/Sn ratio of 500 and calcined at various temperatures.

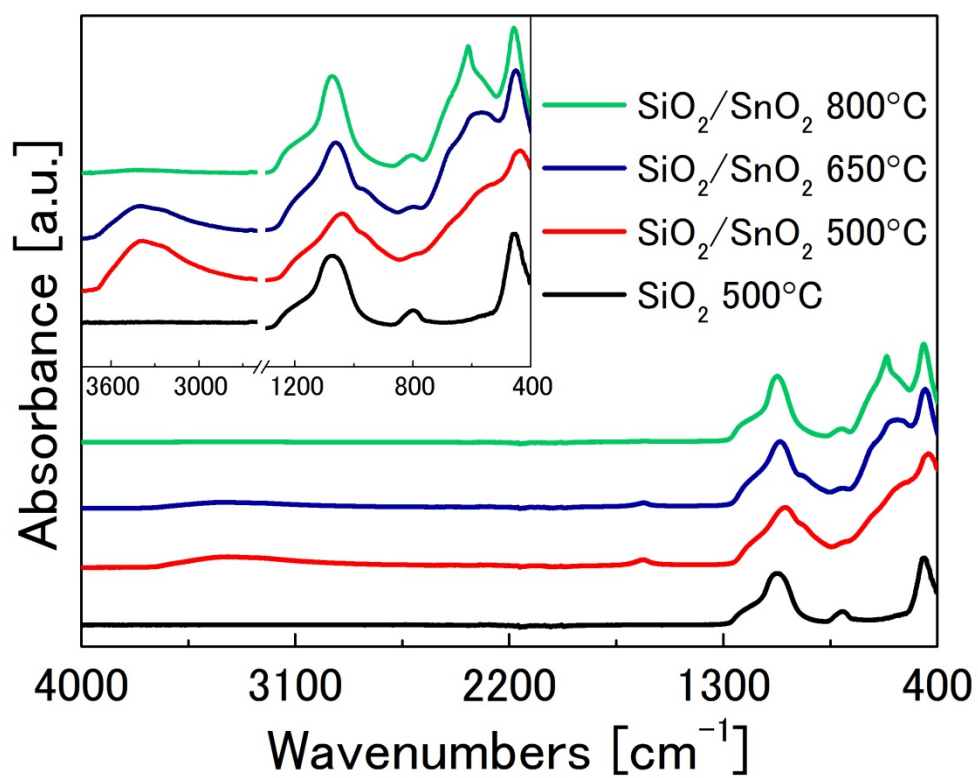


Fig. 5 FT-IR spectra of SiO_2 nanofibers calcined at 500°C and $\text{SiO}_2/\text{SnO}_2$ nanofibers synthesized with acac/Sn ratio of 500 and calcined at various temperatures.

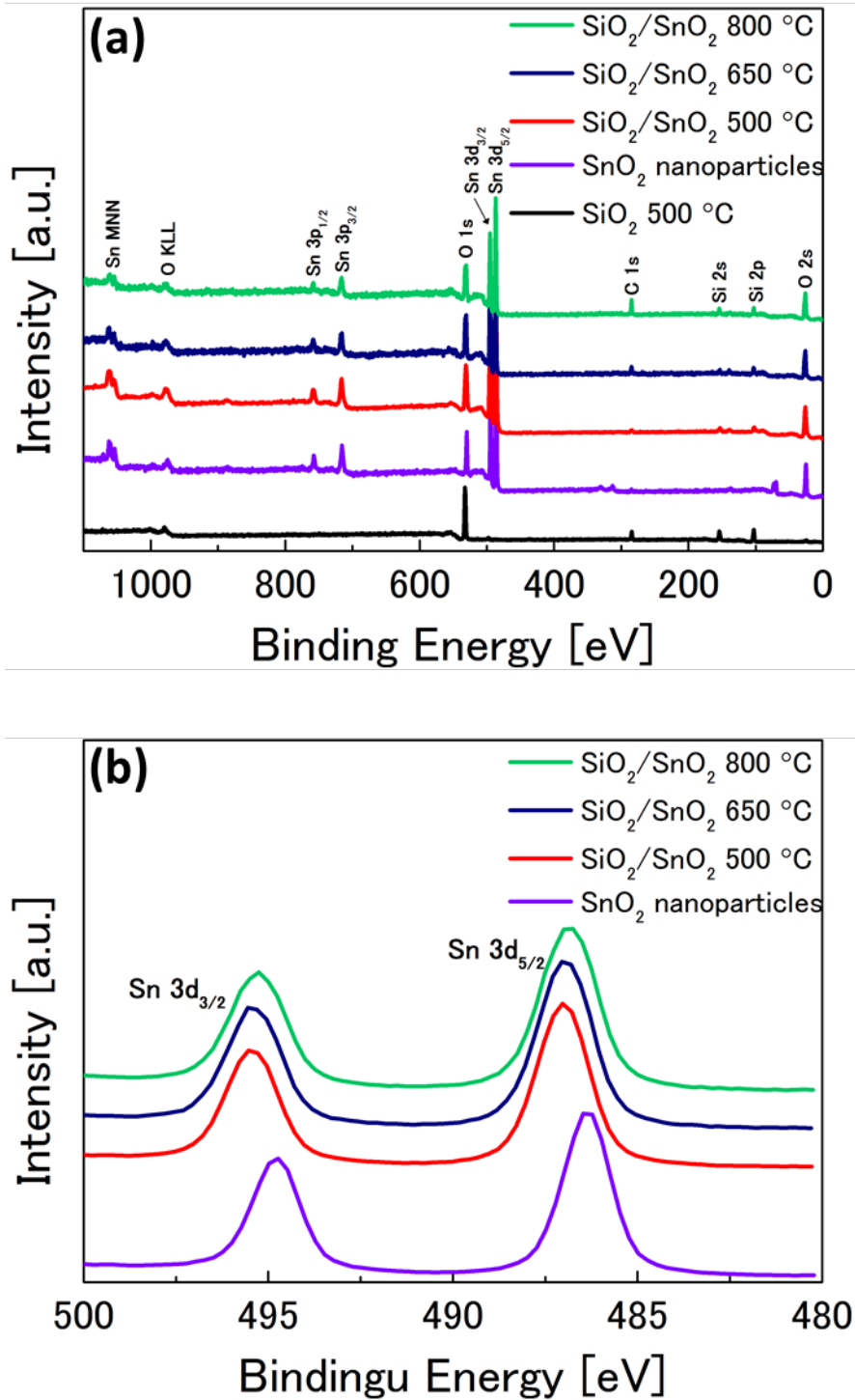


Fig. 7 XPS patterns of SnO₂ nanoparticles, SiO₂ nanofibers calcined at 500°C, and SiO₂/SnO₂ nanofibers synthesized with acac/Sn ratio of 500 and calcined at various temperatures. (a) Survey spectra and (b) high resolution spectra for Sn 3d.

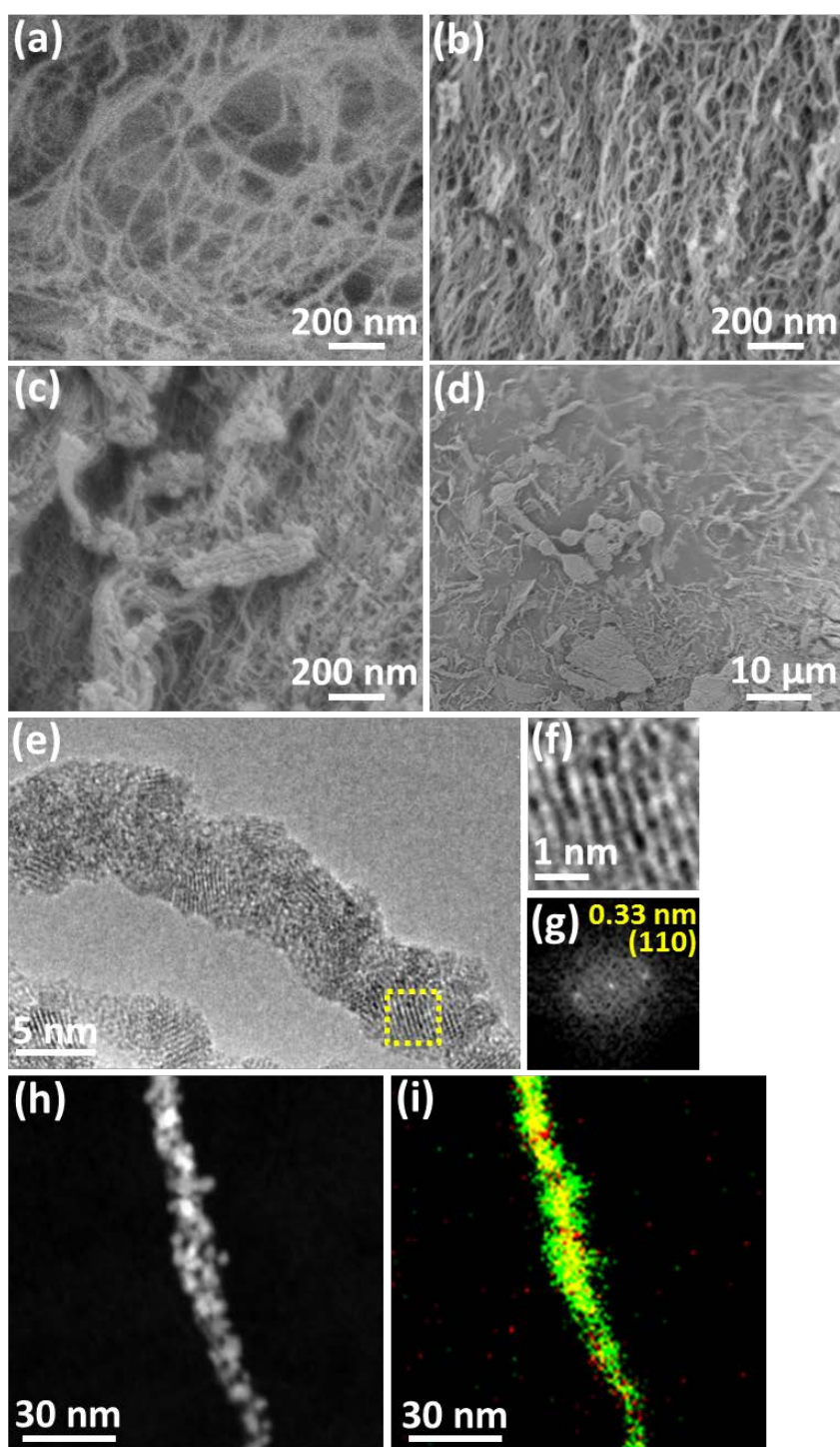


Fig. 8 FE-SEM images of **a** SiO_2 nanofibers calcined at 500°C , **b-d** $\text{SiO}_2/\text{SnO}_2$ nanofibers synthesized with acac/Sn molar ratio of 500 and calcined at 500 , 650 , and 800°C , respectively. **e** TEM image of **b** and **f** high magnified image of dotted area in **e**. FFT image of **f** is shown in **g**. **h** STEM image of **b**. **i** EDS elementary map corresponding to **h**. Red, green, and yellow colors indicate presence of Si, Sn, and both, respectively.

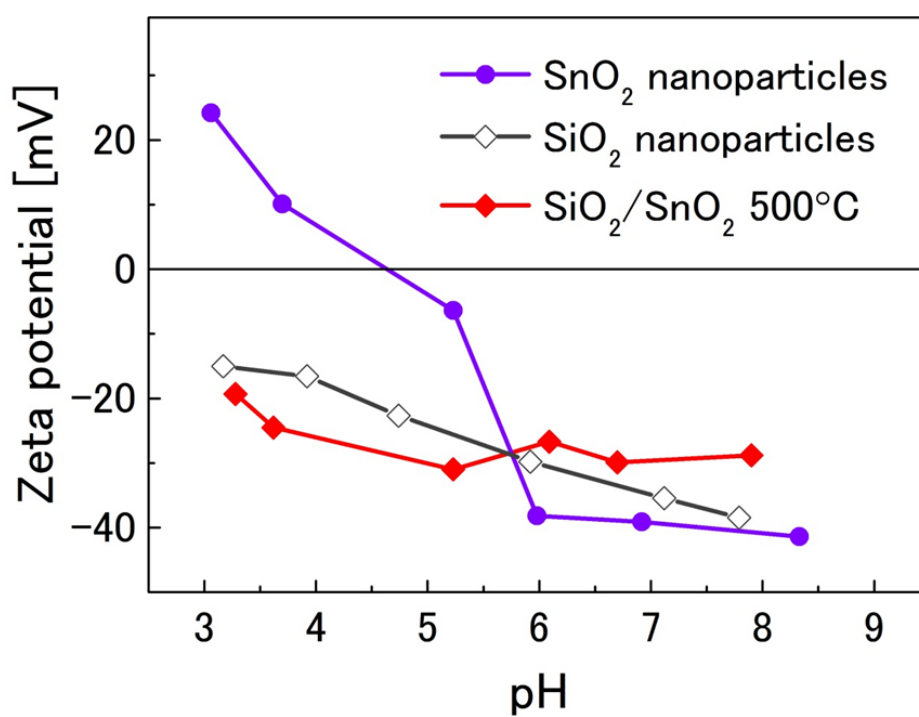


Fig. 9 Zeta potential of SiO₂ nanoparticles, SnO₂ nanoparticles, and SiO₂/SnO₂ nanofibers synthesized with acac/Sn molar ratio of 500 after calcination at 500°C.

3.2 Effect of synthesis condition of SiO₂/SnO₂ nanofibers on gas sensing properties toward ethanol

3.2.1 Introduction

Gas sensors are devices to detect certain gaseous molecules. Nowadays, the demand for gas sensors is increasing over a wide range of fields including chemical and petrochemical industry, environmental field, medical institution and hospital, food and drink industry, semiconductor manufacturing, agriculture, and power generation [1]. In the past, several types of gas sensor have been developed such as electrochemical type, optical type, and chemiresistive type. These three types of gas sensors have different advantages and disadvantages (Table 1) [2-4]. Among them, although the selectivity is not high, chemiresistive gas sensors have gained widespread use because of its durability, cost-effectiveness, fabrication simplicity, and high sensitivity [4].

Metal oxides or conductive polymers are generally used for chemiresistive sensors. In particular, metal oxides are superior in terms of their high thermal and temporal stability, ability to function in harsh environment, and high operation temperature ruling out the effect of environmental changes [1]. Therefore, metal oxides are accepted as suitable materials for chemiresistive sensors.

In 1962, Seyama et al. reported that the gas detection was possible with a ZnO thin film [5], which was the first report on a metal oxide chemiresistive sensor. After that, Taguchi fabricated the first metal oxide chemiresistive sensor device for a practical application using SnO₂ [6]. After the several decades passed, there have been many researches for gas sensor by using various metal oxides such as SnO₂, ZnO, TiO₂, WO₃, In₂O₃, Fe₂O₃, CuO, NiO, Co₃O₄, Cr₂O₃, and Mn₃O₄ [4].

They can be divided into two groups into bulk-sensitive materials and surface-sensitive materials by their sensing principles [7]. Under the introduction of a reducing analyte gas,

bulk-sensitive materials such as TiO₂ decrease their resistance via the formation of bulk oxygen vacancies, however, surface-sensitive materials such as SnO₂ decrease their resistance via the elimination of chemisorbed oxygens after the oxidation reaction with the analyte, despite of the existence of the bulk oxygen defects. In all metal oxides, SnO₂ is most investigated material due to its chemical inertness, low cost, non-toxicity, and high sensitivity [4, 8]. The formation of O⁻, which is representative chemisorbed oxygen at the surface of several metal oxides, can be expressed as follows [9]:



The conduction electrons are transferred to the surface and are trapped by chemisorbed oxygens, leading to the formation of an electron-depleted layer as shown in Fig. 1. The electric resistance can be expressed by following equation [9]:

$$R/R_0 = \exp(qV_s/kT) \quad (2)$$

where R₀ is resistance without any chemisorbed oxygen, qV_s is potential energy barrier, k is Boltzmann constant, and T is temperature. When a reducing gas is introduced, following reaction occurs.



After the reaction, the barrier height decreases due to the consumption of O⁻ as shown in Fig. 2a, resulting in the decrease of the electrical resistance. On the other hand, when crystallites become so small that the depleted layer prevails over the whole crystallite, the energy level at the center of the crystallite shifts as shown in Fig. 2b [10, 11]. It is known that the latter case

brings a large resistance change. Therefore, smaller crystallite size is preferable to achieve a higher sensitivity [12].

Here, the properties of SiO₂/SnO₂ nanofibers as chemiresistive gas sensors were evaluated by using ethanol as analyte gas. Ethanol is one of volatile organic compounds (VOCs). The sensing of ethanol in breath is applicable in the monitoring the blood alcohol concentration [13] and in the detection of laryngeal cancer [14]. The sensor element was fabricated by forming SiO₂/SnO₂ nanofibers to be a sheet. The nanofiber sheet was placed on a ceramic heater and resistance change under the repetitive exposure to ethanol gas which was prepared by saturated vapor ethanol diluted with dry air. Furthermore, here we have investigated the effect of synthesis procedure in SiO₂/SnO₂ nanofibers on the gas sensing properties.

3.2.2 Experimental procedure

3.2.2.1 Preparation of SiO₂/SnO₂ nanofibers sheet as sensor element

The properties as a chemiresistive gas sensor were evaluated about SiO₂/SnO₂ nanofibers synthesized with or without the use of acetylacetone (acac). The calcination temperature was to be 500°C. The SiO₂/SnO₂ nanofibers were pressed to be 1 mm thick with zirconia plates and then cut to be a size of 8 mm × 13 mm. The weight of resulted sheets was about 10 mg.

3.2.2.2 Evaluation of gas sensing properties

Figure 3 shows the schematics of an evaluation system of gas sensing properties. The gas sensing properties of the SiO₂/SnO₂ nanofibers were roughly estimated by the resistance change of the nanofibers sheet during repeated exposure to the atmosphere containing ethanol. The gold electrode was deposited on the nanofibers sheet by a magnetron sputtering (MSP-30T, Vacuum Devices) with a glass mask. In order to measure the resistance, the electrode of the nanofibers

sheet was connected to a digital multimeter (model 2000, Keithley) with silver wires. The nanofibers sheet was placed on a ceramic heater with a size of 10 mm × 20 mm inside a silica glass tube and the measurements were carried out at the operation temperatures between 150°C and 450°C. The synthetic air as a carrier gas was passed through ethanol solution (Kishida Chemicals) iced at 0°C, mixed by the saturated ethanol vapor with partial pressure of about 0.015 atm [15]. To obtain the ethanol gas concentration ranging from 250 ppm to 1000 ppm, the synthetic air including ethanol gas of 15000 ppm was diluted with even more the synthetic air. The total gas flow rate was maintained to be 300 sccm by using a mass flow controllers (MFC; SEC-E40, Horiba STEC). The digital multimeter and the mass flow controllers were controlled using a homemade LabView program. The front panel and block diagram of the program is shown in Fig. 4 and 5, respectively. The sensitivity of gas sensor is defined as follows [16]:

$$\text{Sensitivity} = R_a/R_g \quad (4)$$

where R_a is electrical resistance in air and R_g is electrical resistance under ethanol gas.

3.2.3 Results and discussion

Figure 6a shows the resistance changes of the SiO₂/SnO₂ nanofibers synthesized with acac under the repetitive exposure toward 1000 ppm ethanol gas, operating at various temperatures. Figure 6b shows the calculated sensitivities corresponding to the resistance changes of Fig. 6a. From these results, it was elucidated that the optimum temperature which brought the highest sensitivity was 400°C. At the temperature lower than 400°C, it is conceivable that lower reactivity of the oxidation on the SnO₂ surface resulted in lower sensitivities. On the other hand, at the temperature higher than 400°C, the reactivity was so high that the ethanol gas could not penetrate inside the nanofiber sheet, resulting in lower sensitivity [17]. Additionally, at the

higher temperature, the desorption of chemisorbed oxygens could be dominant leading to lower sensitivity [18].

Figure 7 shows the resistance changes of the SiO₂/SnO₂ nanofibers synthesized with or without acac under the repetitive exposure to 1000 ppm ethanol gas. It was revealed that the SiO₂/SnO₂ nanofibers synthesized with acac indicated the larger resistance change, corresponding to the significantly high sensitivity of 228, compared to those synthesized without acac. This value was about ten times higher than that of the SiO₂/SnO₂ nanofibers synthesized without acac.

Figure 8 shows the relationship between the sensitivity of the SiO₂/SnO₂ nanofibers synthesized with acac and the ethanol concentration. From this graph, the detection limit extrapolated to be 22 ppm [19]. Table 2 summarizes their sensitivities and crystallite sizes. These results clearly show that the ethanol gas sensitivity was enhanced by the suppression of the crystallite size. Since the crystallite sizes of SnO₂ in the SiO₂/SnO₂ nanofibers with or without acac were so small, these nanofibers are expected to follow the model shown in Fig. 2b [12, 20]. Assuming that O⁻ is the only chemisorbed oxygen and one ethanol reacts with one O⁻, the reaction and the sensitivity can be expressed as follows [21, 22]:



$$\text{Sensitivity} = R_a/R_g = (3cC_{\text{EtOH}})^{1/2} a^{-1/2} \quad (6)$$

where c is constant, C_{EtOH} is the concentration of ethanol, and a is the radius of crystallite. The relationships of the sensitivities to the crystallite sizes and to the concentration roughly followed Eq.6, though they did not precisely. There were some possible causes for the difference between the experimental results and the theory. One possibility is that ethanol reacts

with more than one O^- . It was reported that ethanol do not reacted with uniform quantities O^- at the surface of SnO_2 [23]. Moreover, other possibility is that the temperature inhomogeneity in the nanofibers sheet owing to the unidirectional heating with a ceramic heater. To understand the substantial gas sensing properties, the investigations by using the analyte molecules such as H_2 or CO which reacts with only one chemisorbed oxygen are required. Furthermore, the homogenous heating such as a tube furnace is appropriate for the evaluation system of gas sensing properties.

3.2.4 Conclusion

The properties of the SiO_2/SnO_2 nanofibers as chemiresistive gas sensors were estimated. The SiO_2/SnO_2 nanofibers were formed to be a sheet and the resistance change correlated with repetitive exposure to ethanol gas under certain operation temperature was measured. The optimum temperature showing the highest sensitivity was $400^\circ C$. It was notable that the SiO_2/SnO_2 nanofibers synthesized with acac exhibited the excellent sensitivity about ten times larger than that of the SiO_2/SnO_2 nanofibers synthesized without acac toward 1000 ppm ethanol. It is anticipated that the SiO_2/SnO_2 nanofibers can be diverted to detect other analyte gas with high sensitivity. The enhancement of the sensitivity for SiO_2/SnO_2 nanofibers synthesized with acac can be interpreted in terms of the suppression of the crystallite size of SnO_2 . The behavior of gas sensitivity regarding to the gas concentration and the crystallite size was slightly different from the previously proposed theoretical model. Further investigations are required for the interpretation of the gas sensing properties of the SiO_2/SnO_2 nanofibers.

References

1. G. Korotcenkov, Handbook of Gas Sensor Material, Vol. 1 (Springer, 2013).
2. D. M. Wilson, S. Hoyt, J. Janata, K. Booksh, and L. Obando, IEEE Sensors Journal **1**, 256 (2001).
3. T. Hübert, L. B.-Brett, G. Black, and U. Banach, Sensors and Actuators B: Chemical **157**, 329 (2011).
4. G. Neri, Chemosensors **3**, 1 (2015).
5. T. Seiyama, A. Kato, K. Fujiishi, and M. Nagatani, Analytical Chemistry **34**, 1502 (1962).
6. N. Taguchi, Gas detecting device, US Patent 3, 631, 436 (1971).
7. M. Batzill and U. Diebold, Progress in Surface Science **79**, 47 (2005).
8. S. Das and V. Jayaraman, Progress in Material Science **66**, 112 (2014).
9. N. Barsan and U. Weimar, Journal of Electroceramics **7**, 143 (2001).
10. A. Rothschild and Y. Komem, Journal of Applied Physics **95**, 6374 (2004).
11. N. Yamazoe and K. Shimano, Journal of The Electrochemical Society **155**, J85 (2008).
12. N. Yamazoe and K. Shimano, Journal of The Electrochemical Society **155**, J93 (2008).
13. K. Mitsubayashi, K. Yokoyama, T. Takeuchi, and I. Karube, Analytical Chemistry **66**, 3297 (1994).
14. R. A. García, V. Morales, S. Martín, E. Vilches, and A. Toledano, Chromatographia **77**, 501 (2014).
15. N. A. Lange, Lange's Handbook of Chemistry, 10th ed. (McGraw-Hill Book Company, 1967).
16. J. Watson, K. Ihokura, and G. S. V. Coles, Measurement Science and Technology **4**, 711 (1993).
17. G. Sakai, N. Matsunaga, K. Shimano, and N. Yamazoe, Sensors and Actuators B **80**, 125

(2001).

18. N. Yamazoe, J. Fuchigami, M. Kishikawa, T. Seiyama, *Surface Science* **86**, 335 (1979).
19. R. Xing, L. Xu, J. Song, C. Zhou, Q. Li, D. Liu, and H. W. Song, *Scientific Reports* **5**, 10717 (2015).
20. K. Suematsu, M. Yuasa, T. Kida, N. Yamazoe, and K. Shimano, *Journal of The Electrochemical Society* **159**, J136 (2012).
21. H. Ogawa, M. Nishikawa, and A. Abe, *Journal of Applied Physics* **53**, 4448 (1982).
22. N. Yamazoe and K. Shimano, *Sensors and Actuators B* **138**, 100 (2009).
23. H.-W. Cheong and M.-J. Lee, *Journal of Ceramic Processing Research* **7**, 183 (2006).

Table 1 Comparison of three types of gas sensors.

	Electrochemical	Optical	Chemiresistive (Metal oxide)	Chemiresistive (Polymer)
Sensitivity	Low	High	Moderate	Moderate
Selectivity	High	High	Moderate	Low
Lifetime	Short	Long	Long	Long
Size	Moderate	Large	Small	Small
Cost	Low	High	Low	Low
Physical change	Electromotive force	Transmission	Resistance	Resistance

Table 2 SnO₂ crystallite sizes and sensitivities to ethanol of SiO₂/SnO₂ nanofibers synthesized with or without acac.

Molar ratio of acac/Sn	Crystallite size [nm]	Sensitivity to 1000 ppm ethanol
0	11	22.1
500	3.2	228

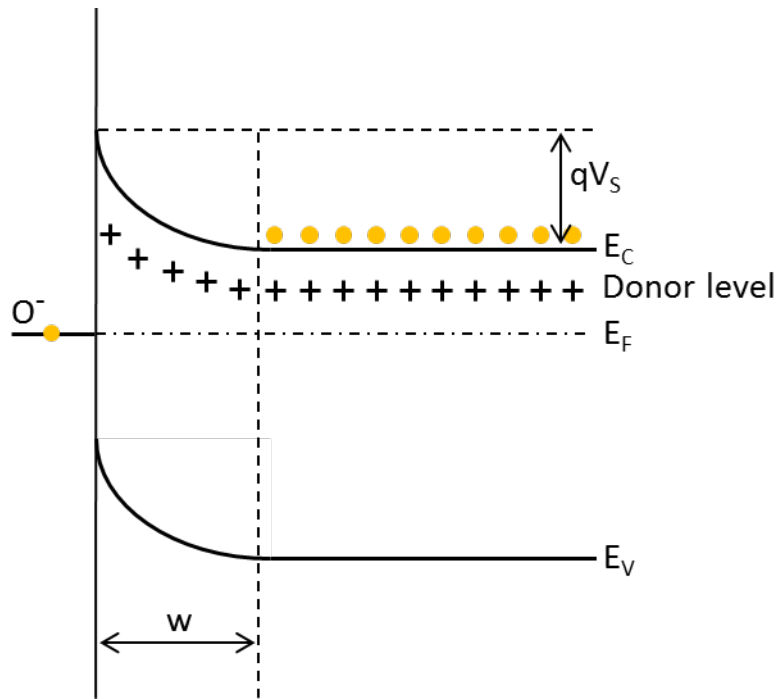


Fig. 1 Schematic diagram of electron-depleted layer in wide-bandgap semiconductor after chemisorption of oxygen on surface sites. E_C , E_V , and E_F denote energy of conduction band, valence band, and Fermi level, respectively. While w denotes thickness of electron-depleted layer, and qV_S denotes potential energy barrier.

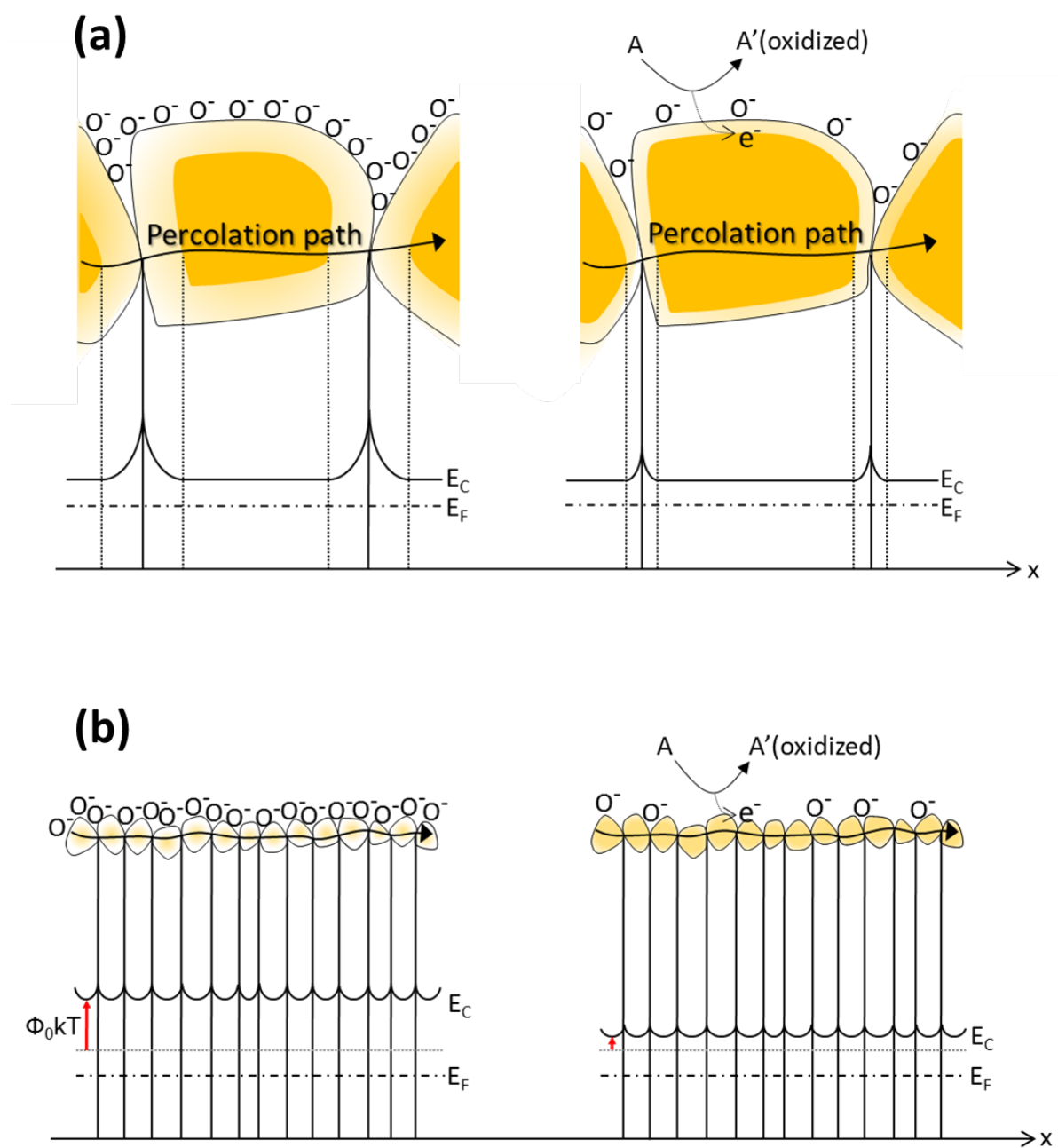


Fig. 2 Structural and band model showing contact regions of crystallites in chemiresistive gas sensor. Left- and right-hand sides represent before and after exposure to reducing gas, respectively. **a** The case that crystallite radius is much larger than thickness of electron-depleted layer. **b** The case that crystallite radius is smaller than thickness of electron-depleted layer. $\Phi_0 kT$ denotes energy shift at center of crystallite from E_C .

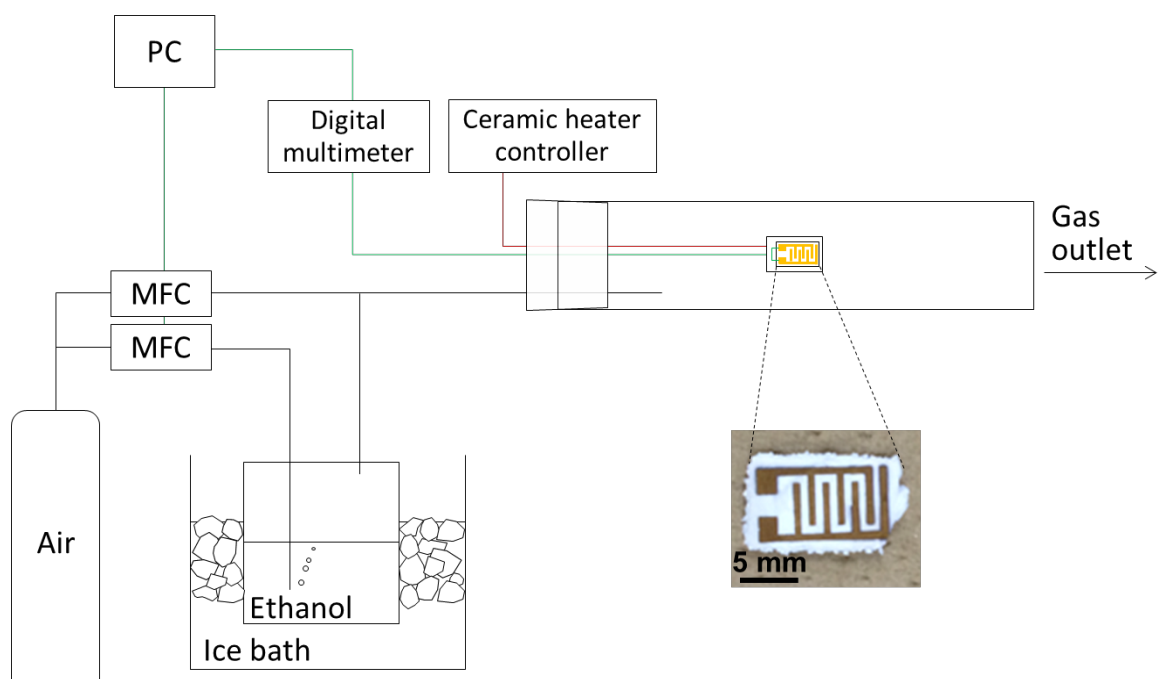


Fig. 3 Schematic of evaluation system of gas sensing property.

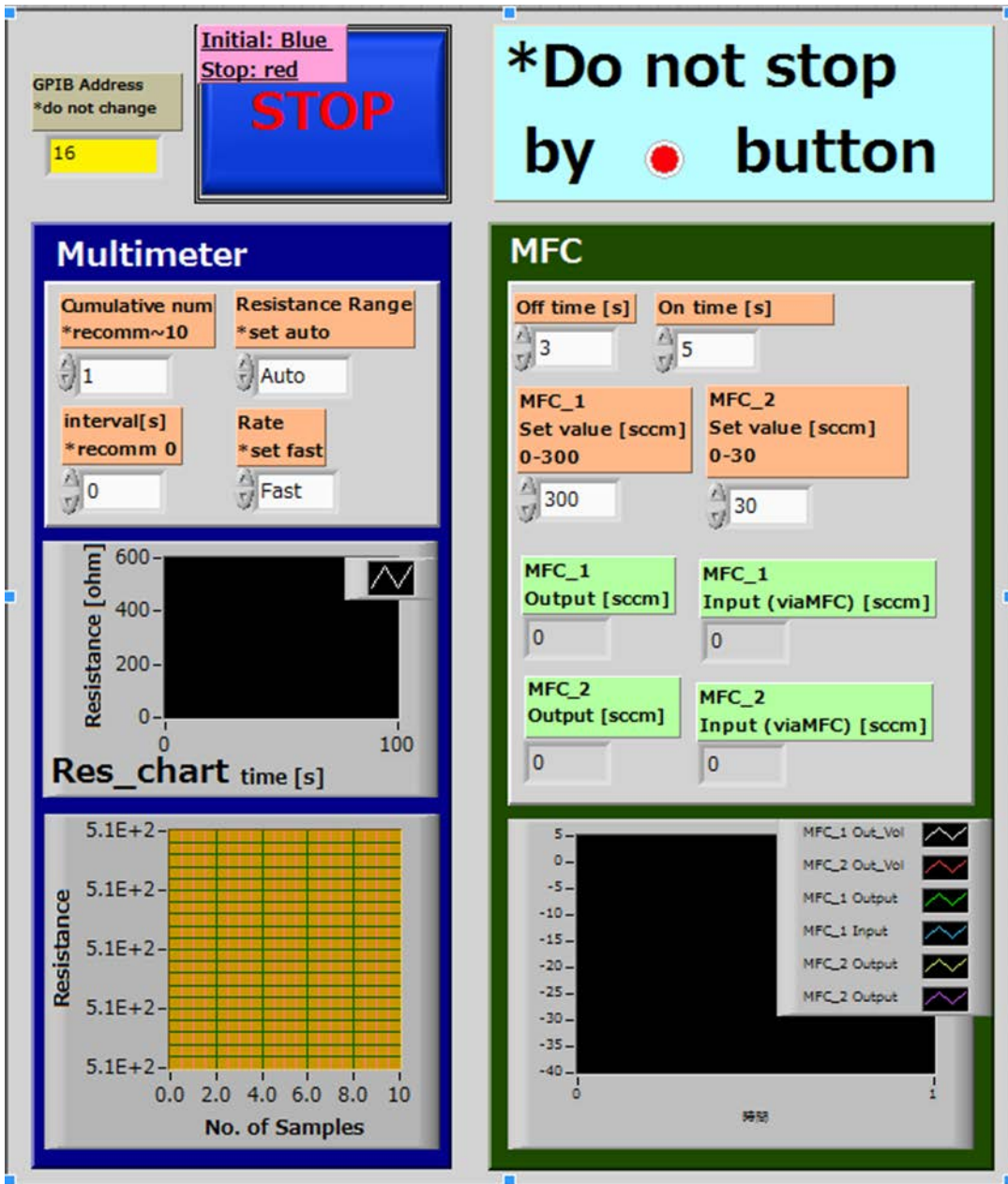


Fig. 4 Front panel of Labview program.

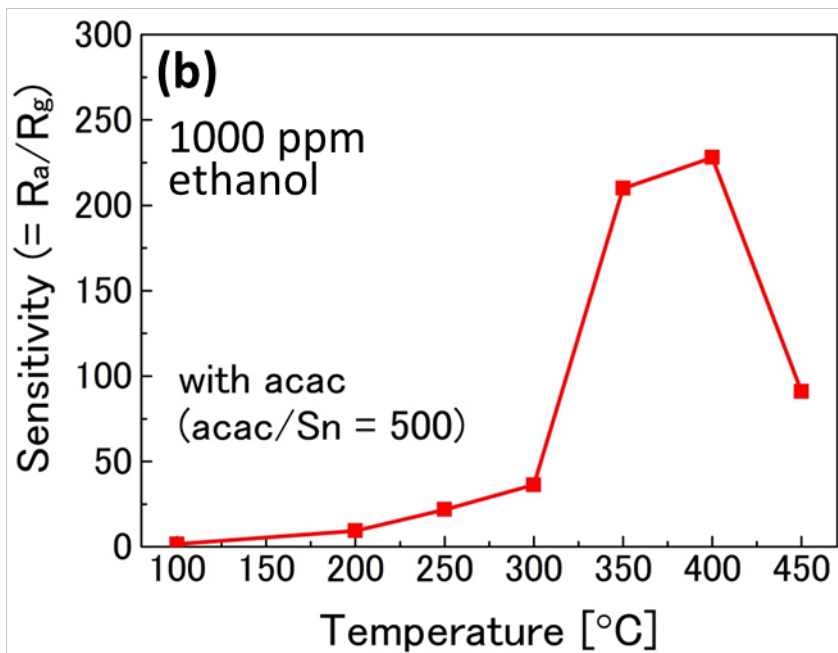
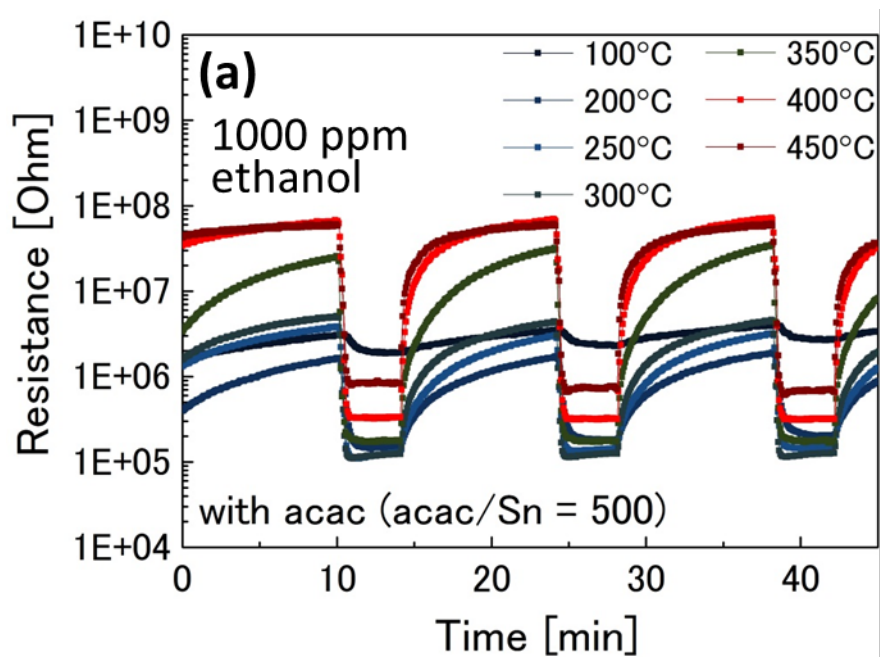


Fig. 6 a Repetitive response to 1000 ppm ethanol under various operation temperatures, and **b** plots of sensitivities to 1000 ppm ethanol under various operation temperatures, about $\text{SiO}_2/\text{SnO}_2$ nanofibers synthesized with acac.

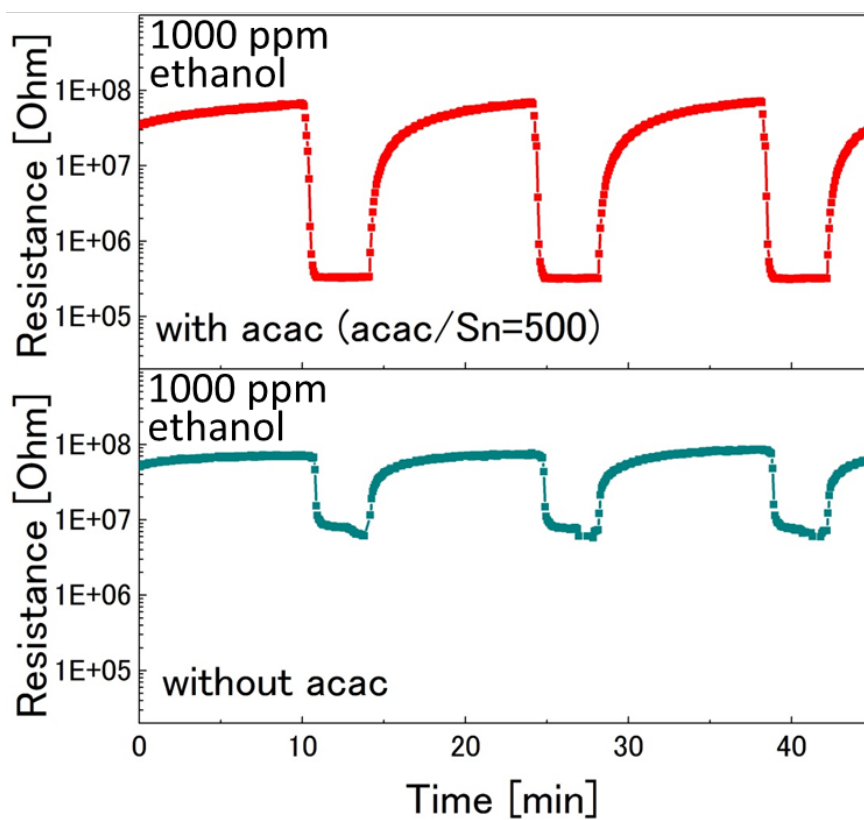


Fig. 7 Repetitive response to 1000 ppm ethanol operating at 400°C, about SiO₂/SnO₂ nanofibers synthesized with or without acac.

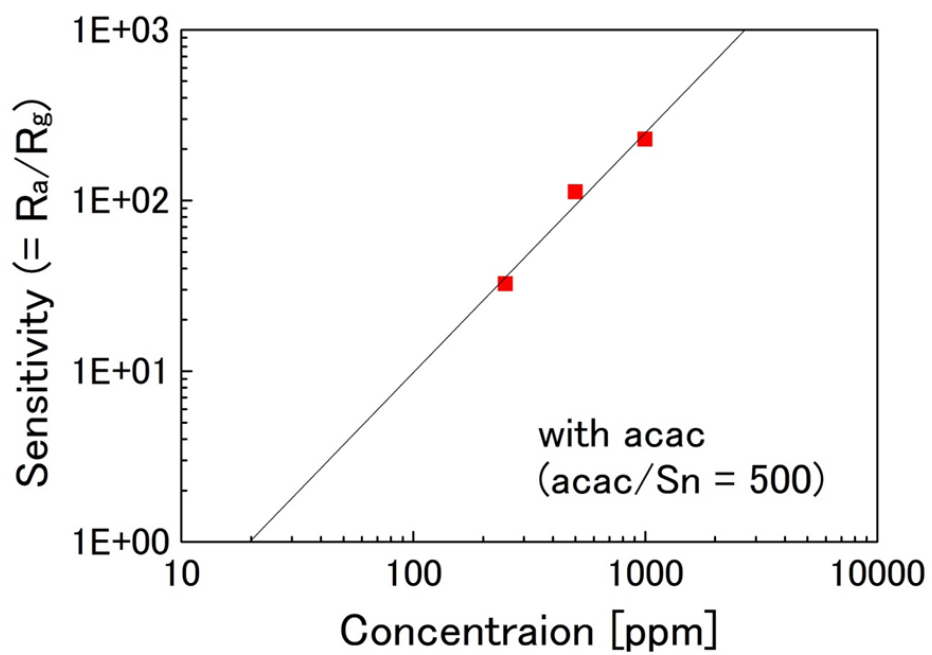


Fig. 8 Sensitivities of SiO₂/SnO₂ nanofibers synthesized with acac under various ethanol concentration.

3.3 Advantage in gas sensing properties of SiO₂/SnO₂ nanofibers compared to conventional SnO₂ nanoparticles

3.3.1 Introduction

To improve the sensitivity, durability, and selectivity for the metal oxide chemiresistive gas sensors, many researchers have investigated the combination of a metal cation and a metal oxide. [1-4]. In some cases, a trivalent cation such as Al or Fe was doped into SnO₂ to improve the sensitivity through the enlargement of depleted layer derived from the decreased carrier density [5, 6]. In other cases, by carrying an oxide semiconductor such as p-type Cr₂O₃ or n-type TiO₂ on a SnO₂ surface, the gas sensitivities were improved through the formation of p-n or n-n junction derived from the difference of Fermi levels at their interface [7, 8]. The p-n junction enlarged the electron-depleted layer, making the resistance change larger after the introduction of reducing molecules. While, the n-n junction produced the electron-accumulated layer on the SnO₂ side, which increased the amount of chemisorbed oxygen atoms directly related to sensor responses.

Meanwhile, in spite of none of electrical interactions, it was empirically reported that the complexing with SiO₂ was effective to improve the properties of SnO₂ based gas sensors. The SnO₂ particles coated with thin SiO₂ achieved the good selectivity to H₂ because only H₂ was permitted to pass through the SiO₂ layer due to its extremely small molecular size [9]. Moreover, the composite of SiO₂ and SnO₂ showed the enhanced sensitivity, because SiO₂ hindered the neck formation between SnO₂ domains, the electron-depleted layer on the SnO₂ surface remained sufficiently [10, 11]. Furthermore, unexpectedly the optimum temperature for the highest gas sensitivities of the composite of SnO₂ and mesoporous silica was changed compared to the conventional SnO₂ nanoparticles [12, 13]. Until now, the mechanisms of such phenomena are not fully understood.

These clearly indicate that the presence of SiO₂ effects on the gas sensitivities of SiO₂/SnO₂ nanofibers. In addition, the porous structure accomplished by the nanofibers is suitable as a gas sensor for larger molecules in terms of the diffusion path [14]. To evaluate the detailed gas sensing properties, compared to the conventional SnO₂ nanoparticles, the screen-printed sensor elements with SiO₂/SnO₂ nanofibers were exposed to H₂ or CO analyte gas under various temperatures. Although these molecular sizes of analyte gases are different, leading to their diffusivity, both react with one chemisorbed oxygen (such as O⁻) in the same way as follows:



Particularly, in the experiments, the relations between the operating temperature and the sensitivity to H₂ and CO analyte gases were investigated.

3.3.2 Experimental procedure

3.3.2.1 Reference sample of SnO₂ nanoparticles

For the comparison to SiO₂/SnO₂ nanofibers in the gas sensing, a reference sample of SnO₂ nanoparticles was prepared by the conventional hydrothermal treatment of hydrated gel [15, 16]. The hydrated SnO₂ gel was precipitated by adding 1.0 M aqueous solution of NH₄HCO₃ (Wako Pure Chemical) toward 1.0 M aqueous solution of SnCl₄. The precipitated gel was washed by deionized water repeatedly with centrifugation. Then the washed gel was suspended in deionized water adjusted with the pH value of 10.5 using ammonia aqueous solution (Wako Pure Chemical). Then, the suspension was transferred to an autoclave and heated at 200°C for 3

h. After the hydrothermal treatment, the suspension was followed by drying at 120°C for 12 h and subsequently calcined at 700°C for 3 h in air.

3.3.2.2 Characterization

X-Ray diffraction (XRD) patterns were measured by an X-Ray diffractometer equipped with CuK α source (RINT-2500HFK, Rigaku). Crystallite sizes are also estimated by Scherrer equation [17]. FT-IR spectra were measured by an FT-IR spectrometer equipped with an ATR accessory (Spectrum Two, Perkin Elmer). Microscopic structures were observed by a field-emission scanning electron microscope (FE-SEM; JSM-6700F, JEOL). BET specific surface areas [18] and pore distributions [19] were characterized by using an N₂ adsorption-desorption apparatus (Tristar 3000, Shimadzu).

3.3.2.3 Preparation of sensor element

To obtain the paste of the SiO₂/SnO₂ nanofibers or the SnO₂ reference nanoparticles, α -terpineol (Wako Pure Chemicals) was used as a binder. The SiO₂/SnO₂ nanofibers were synthesized using acetylacetone (acac, Kishida Chemicals) with the acac/Sn ratio of 500 followed by calcination at 500°C. Then, these pastes were screen-printed on an alumina plate (9 mm \times 13 mm \times 0.38 mm) with interdigitated Au electrodes. The binder was eliminated by the heat treatment at 480°C for 5 h. This temperature was lower than the calcination temperature of the SiO₂/SnO₂ nanofibers. Finally the thick film sensor elements for the evaluation were obtained. The sensor elements were placed in a silica reaction tube and the resistance changes accompanied by the introduction of the H₂ or CO analyte gas were measured under various temperatures.

3.3.2.4 Estimation of gas sensing properties

Figure 1 shows a schematic of the estimation system of gas sensing properties. A sensor element fabricated by the screen-printing method is also shown. Resistance changes under the introduction of H₂ or CO analyte gas were monitored by a digital multimeter (model 2701, Keithley). The H₂ or CO analyte gas including air (Taiyo Nippon Sanso) was further diluted with synthetic air (Taiyo Nippon Sanso) to be 200 ppm with mass flow controllers (Horiba Stec). Sequentially, the analyte gas was introduced toward a sensor element in a reaction tube under heating by a tube furnace. The operating temperatures were changed from 300°C to 450°C in the case of H₂ analyte gas. In the case of CO analyte gas, the temperatures were set to be no higher than 400°C, to avoid the reduction of lattice oxygen [20]. All measurements were carried out after the refreshing at 480°C for 3 h to eliminate adsorbed residues derived from analytes and the cooling down to a operation temperature with the rate of 0.556°C/min. The gas sensitivity, is conventionally defined as follows [21]:

$$\text{Sensitivity} = R_a/R_g \quad (4)$$

where R_a is electrical resistance for clean air and R_g is electrical resistance for target analyte gas.

3.3.3 Results and discussion

Figure 2 shows the characterization results of the SiO₂/SnO₂ nanofibers and the reference SnO₂ nanoparticles. From the XRD patterns (Fig. 2a), the both structures of SnO₂ in the SiO₂/SnO₂ nanofibers and in the reference SnO₂ nanoparticles were rutile SnO₂ (JCPDS card no. 41-1445) and the crystallite sizes were 3.2 nm and 15 nm, respectively. FT-IR spectra shows the broad peak between 700 and 400 cm⁻¹ derived from typical SnO₂ absorption [22] in both the

SiO₂/SnO₂ nanofibers and the SnO₂ nanoparticles, besides the peaks derived from amorphous SiO₂ [23] and Si–O–Sn bond [24] in the SiO₂/SnO₂ nanofibers (Fig. 2b). FE-SEM images revealed that the SnO₂ reference nanoparticles were the aggregates of formless particles in comparison to the SiO₂/SnO₂ nanofibers (Fig. 2c, d). The SiO₂/SnO₂ nanofibers had the larger pore volume than the SnO₂ nanoparticles. Particularly the pore size distribution at below about 10 nm pore size in nanofibers was quite different from that in nanoparticles (Fig. 2e). The crystallite sizes and the specific surface areas for the SiO₂/SnO₂ nanofiber and SnO₂ reference nanoparticles were summarized in Table 1.

Figure 3 shows the resistance of the sensor element in clean air at the various operating temperatures. Over whole operating temperatures, the SiO₂/SnO₂ nanofibers exhibited higher resistance by three order of magnitude than that for the SnO₂ nanoparticles. This is due to the presence of insulating SiO₂ (Fig. 2b) and their larger pore volume (Fig. 2d, 2e). Both of the resistance values were monotonically decreased with increasing in the operating temperature, which was corresponding to the previously reported typical features of semiconducting materials such as a screen-printed SnO₂ thick film [25].

Figure 4 shows the response of the resistance for sensor elements under the introduction of H₂ or CO analyte gas at various temperatures. Figure 5 also shows the plots of the sensitivities to the analyte gases under various operating temperatures. In the case of the SnO₂ reference nanoparticles, the behavior of sensitivity to temperature was almost same as previous reports [26], where the suitable operating temperature was no more than about 350°C. On the other hand, the sensitivity of the SiO₂/SnO₂ nanofibers was dramatically increased at higher temperature of 400°C. This phenomenon is similar to the previous report in which the optimum temperature shifted higher for the mechanically mixed composite of SiO₂ and SnO₂ compared to the conventional SnO₂ behavior [12]. Of course, the significantly high sensitivity for the

SiO₂/SnO₂ nanofibers can be interpreted by the smaller crystallite size and the larger pore volume (Table 1, Fig. 2) [14, 27]. Since two analyte gases were differed in molecular sizes, the diffusivities should change, however the difference was not so sufficient. More detailed estimation by using larger molecular gas such as toluene is required.

Two reasons can be suggested for the improvement of the sensitivity in the case of nanofibers at higher temperature of 400°C as follows: One is the low reactivity of chemisorbed oxygens with analyte gas. Generally, the sensitivity should become higher with increasing temperature [28]. The fact that high temperature was required for raising the sensitivity implies the low reactivity of chemisorbed oxygen atoms at the surface of the SiO₂/SnO₂ nanofibers. Other is the retention of chemisorbed oxygen atoms even at high operating temperature. It is known that the chemisorbed oxygen atoms at the SnO₂ surface happen to desorb at about 400°C, leading to the lower sensitivity [29]. The excellent sensitivity at the high operating temperature for the SiO₂/SnO₂ nanofibers means that the chemisorbed oxygen atoms still remained. It should be noted that the shifting to the high temperature side of the operating temperature of gas sensor could be caused by the changes in the interaction of SnO₂ with chemisorbed oxygen atoms. This interesting gas sensing properties of the SiO₂/SnO₂ nanofibers are useful for detecting the less reactive gases such as methane [30] and suppressing SnO₂ surface poisoning [31]. To understand the detailed mechanisms, further investigations such as a temperature programmed desorption (TPD) are required.

3.3.4 Conclusion

The properties of the SiO₂/SnO₂ nanofibers as chemiresistive gas sensors were evaluated compared to the SnO₂ nanoparticles. The resistance change under the introduction of H₂ or CO as an analyte gas were measured with the thick film sensor elements prepared by screen-printing.

Surprisingly, the $\text{SiO}_2/\text{SnO}_2$ nanofibers exhibited the extremely high sensitivity at high operating temperature where the SnO_2 nanoparticles did not work well both to H_2 and CO . This unique feature seems to be derived from the presence of SiO_2 . Apart from the basic understanding the mechanisms, the $\text{SiO}_2/\text{SnO}_2$ nanofibers can be applied as a sensor element material at high operating temperature.

References

1. N. Yamazoe, Y. Kurokawa, and T. Seiyama, *Sensors and Actuators* **4**, 283 (1983).
2. G. Korotchenkov, *Sensors and Actuators B: Chemical* **107**, 209 (2005).
3. A. Afzal, N. Cioffi, L. Sabbatini, and L. Torsi, *Sensors and Actuators B: Chemical* **171**, 25 (2012).
4. T. Li, W. Zeng, and Z. Wang, *Sensors and Actuators: B* **221**, 1570 (2015).
5. C. Xu, J. Tamaki, N. Miura, and N. Yamazoe, *Sensors and Actuators B* **3**, 147 (1991).
6. K. Suematsu, M. Yuasa, T. Kida, N. Yamazoe, and K. Shimano, *Journal of The Electrochemical Society* **159**, J136 (2012).
7. S.-W. Choi, A. Katoch, J.-H. Kim, and S. S. Kim, *ACS Applied Materials & Interfaces* **6**, 17723 (2014).
8. W. Zeng, T. Liu, and Z. Wang, *Physica E* **43**, 633 (2010).
9. G. Tournier and C. Pijolat, *Sensors and Actuators B* **106**, 553 (2005).
10. K. Wada and M. Egashira, *Sensors and Actuators B* **53**, 147 (1998).
11. A. Tricoli, M. Graf, and S. E. Pratsinis, *Advanced Functional Materials* **18**, 1969 (2008).
12. G. Li and S. Kawi, *Sensors and Actuators B* **59**, 1 (1998).
13. J. Yang, K. Hidajat, and S. Kawi, *Journal of Materials Chemistry* **19**, 292 (2008).
14. G. Sakai, N. Matsunaga, K. Shimano, and N. Yamazoe, *Sensors and Actuators B* **80**, 125 (2001).
15. N. S. Baik, G. Sakai, N. Miura, and N. Yamazoe, *Journal of the American Ceramic Society* **83**, 2983 (2000).
16. N. S. Baik, G. Sakai, N. Miura, and N. Yamazoe, *Sensors and Actuators B* **63**, 74 (2000).
17. A. L. Patterson, *Physical Review* **56**, 978 (1939).
18. S. Brunauer, P. H. Emmett, and E. Teller, *Journal of the American Chemical Society* **60**,

- 309 (1938).
19. E. P. Barrett, L. G. Joyner, and P. P. Halenda, *Journal of the American Chemical Society* **73**, 373 (1951).
 20. R. Sasikala, N. M. Gupta, and S. K. Kulshreshtha, *Catalysis Letters* **71**, 69 (2001).
 21. J. Watson, K. Ihokura, and G. S. V. Coles, *Measurement Science and Technology* **4**, 711 (1993).
 22. D. Amalric-Popescu and F. Bozon-Verduraz, *Catalysis Today* **70**, 139 (2001).
 23. J. Wang, B. Zou, and M. A. E.-Sayed, *Journal of Molecular Structure* **508**, 87 (1999).
 24. P. Shah, A. V. Ramaswamy, K. Lazar, and V. Ramaswamy, *Applied Catalysis A General* **273**, 239 (2004).
 25. N. Yamazoe, K. Shimano, and C. Sawada, *Thin Solid Films* **515**, 8302 (2007).
 26. N. S. Baik, G. Sakai, K. Shimano, N. Miura, and N. Yamazoe, *Sensors and Actuators B* **65**, 97 (2000).
 27. N. Yamazoe and K. Shimano, *Journal of The Electrochemical Society* **155**, J93 (2008).
 28. G. Sakai, N. Matsunaga, K. Shimano, and N. Yamazoe, *Sensors and Actuators B* **80**, 125 (2001).
 29. N. Yamazoe, J. Fuchigami, and M. Kishikawa, *Surface Science* **86**, 335 (1979).
 30. D. Kohl, *Sensors and Actuators* **18**, 71 (1989).
 31. B. Ruhland, T. Beker, and G. Müller, *Sensors and Actuators B* **50**, 85 (1998).

Table 1 Crystallite size and BET specific surface area of SiO₂/SnO₂ nanofibers with acac/Sn molar ratio of 500 and calcined at various temperatures.

	Crystallite size [nm]	BET specific surface area [m ² /g]
SnO ₂ nanoparticles	15	32.0
SiO ₂ /SnO ₂ nanofibers	3.2	322

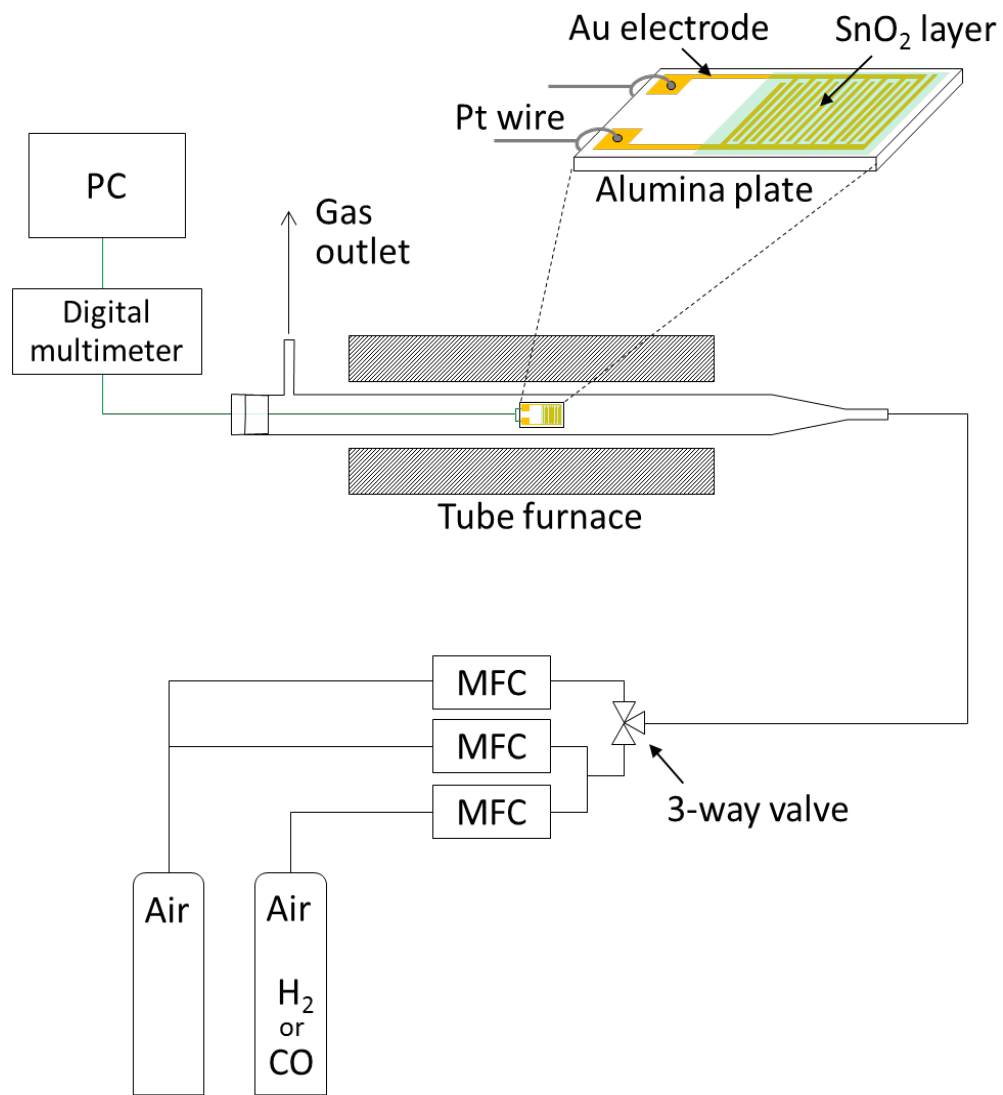


Fig. 1 Schematic of estimation system of gas sensing properties. A schematic of sensor element fabricated by the screen-printing method is also shown.

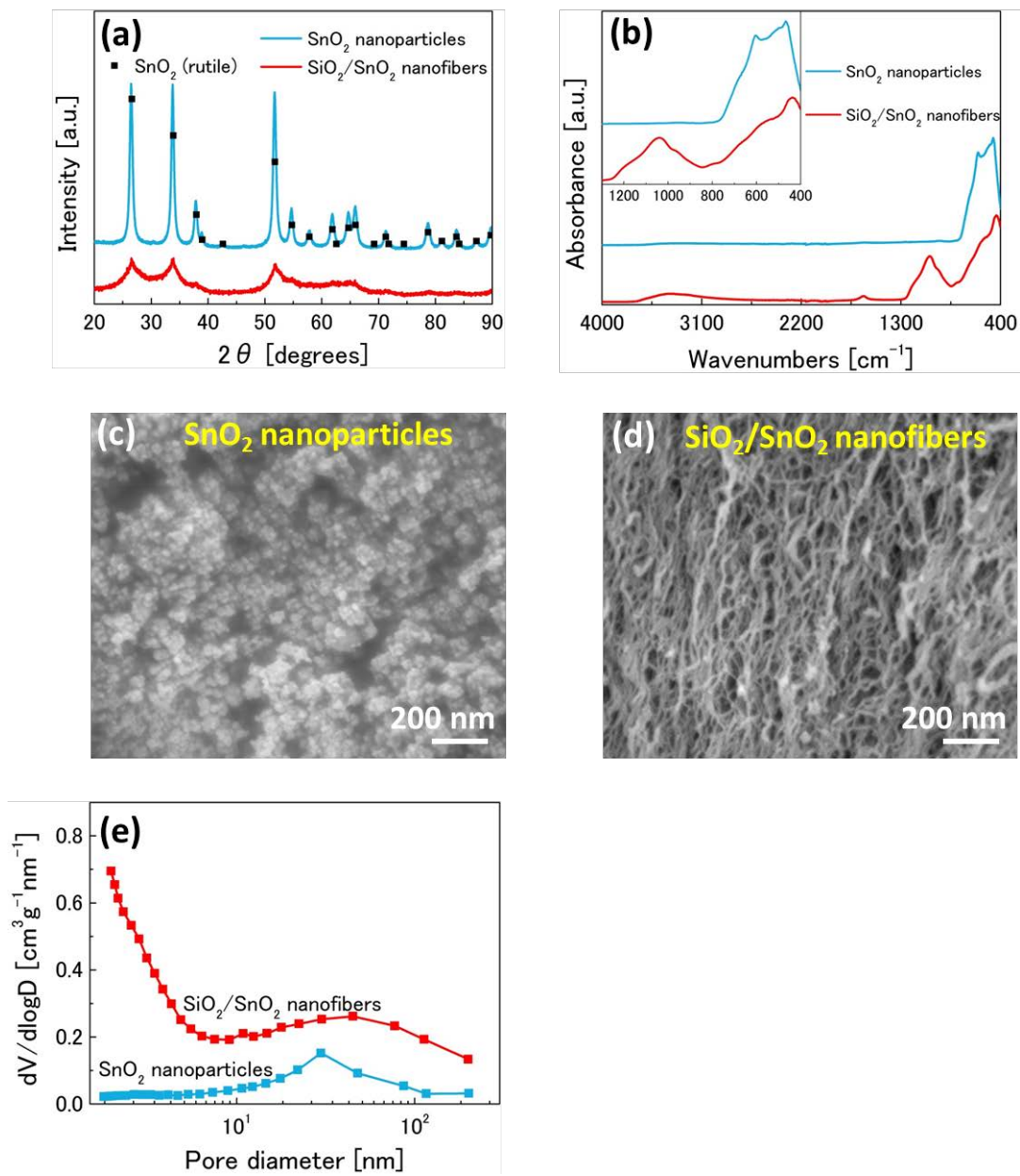


Fig. 2 **a** XRD patterns, **b** FT-IR spectra, **c**, **d** FE-SEM images, and **e** pore size distributions of SiO₂/SnO₂ nanofibers and SnO₂ nanoparticles.

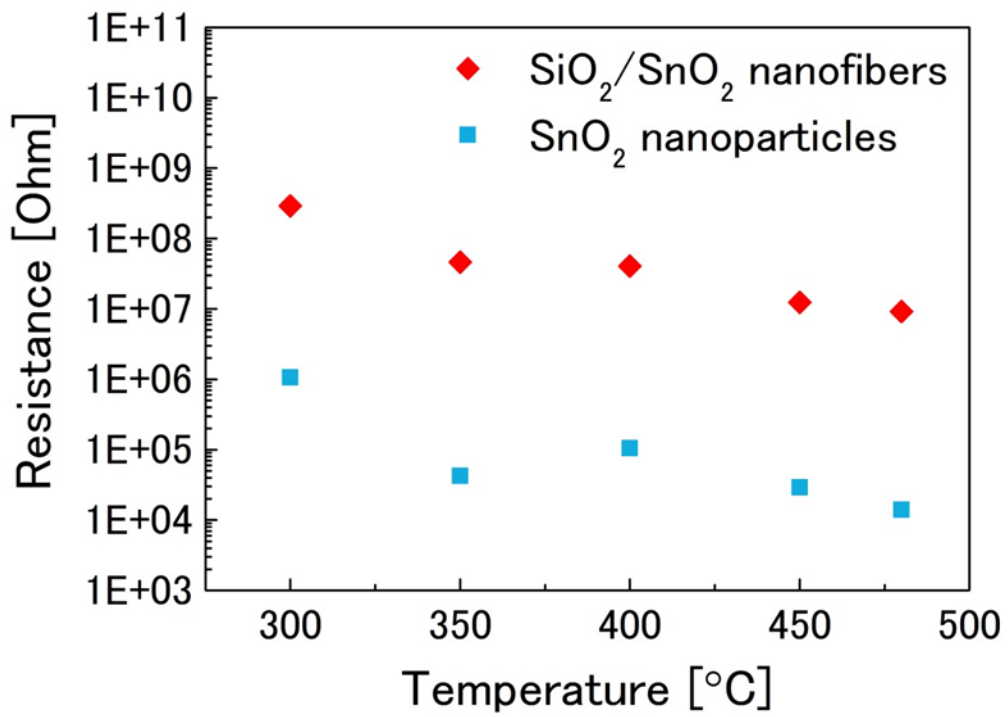


Fig. 3 Resistance in synthetic air as a function of operating temperatures.

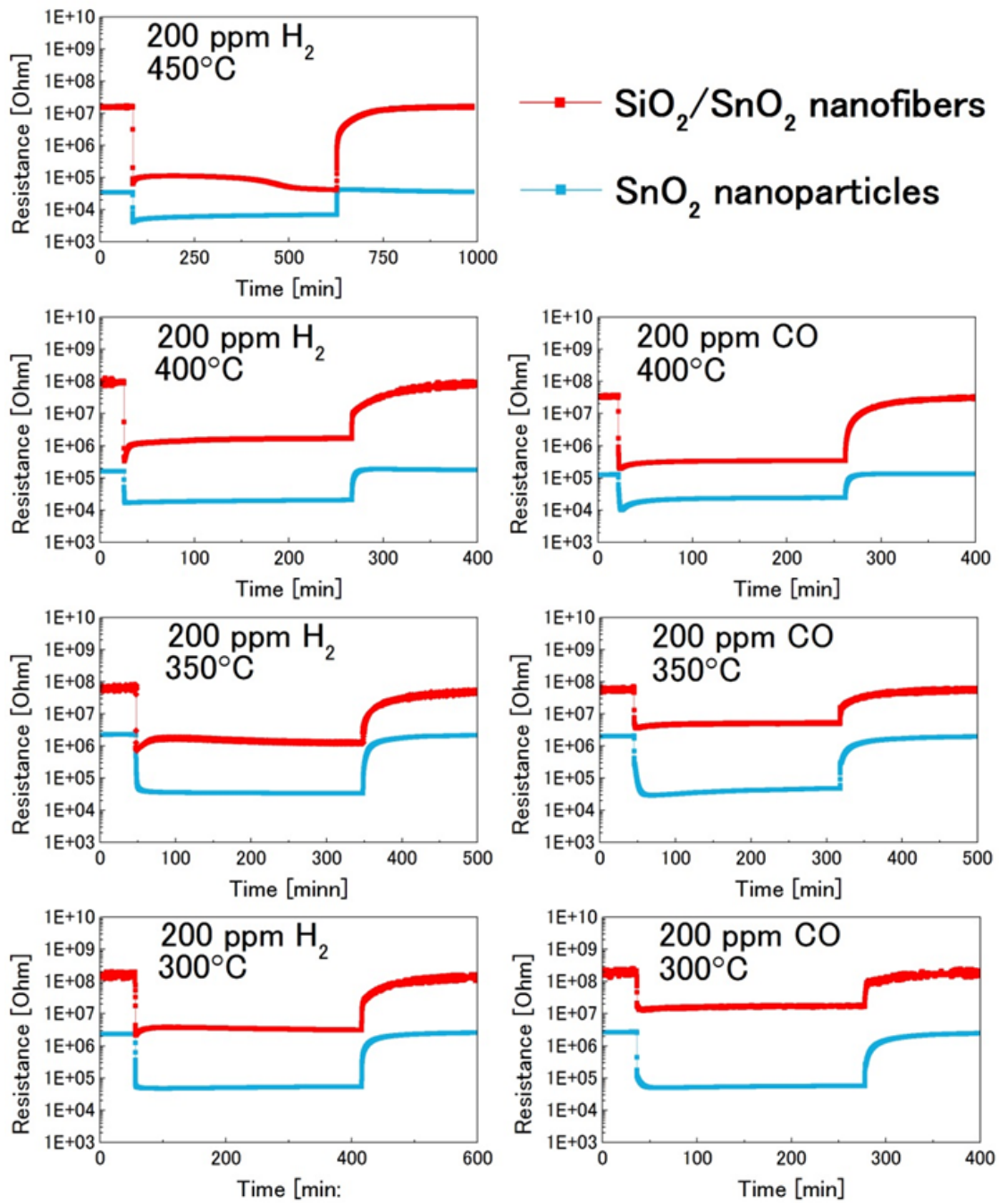


Fig. 4 Responses of the resistance for the sensor elements to 200 ppm H₂ or CO analyte gas under various operation temperatures.

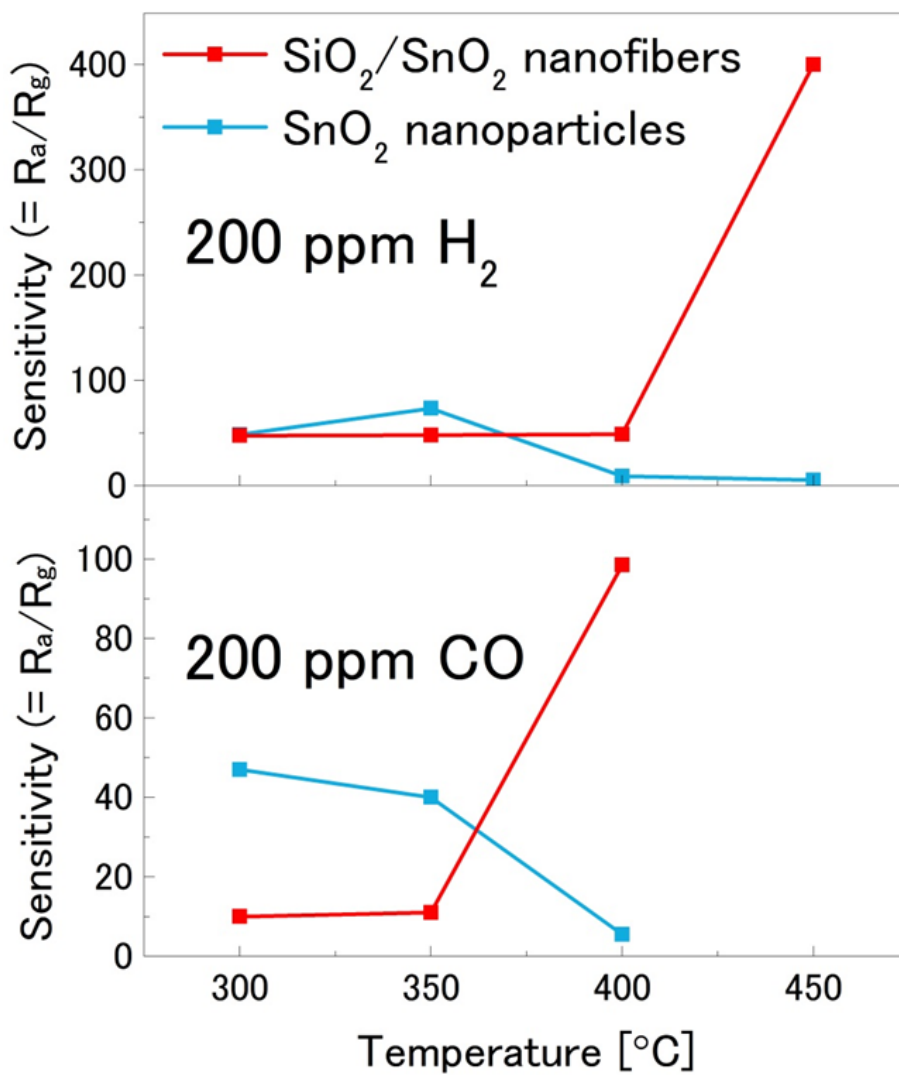


Fig. 5 Plots of sensitivity for sensor elements to 200 ppm H₂ or CO analyte gas under various operating temperatures.

3.4 Gas sensing properties of SiO₂/SnO₂ nanofibers under humid conditions

3.4.1 Introduction

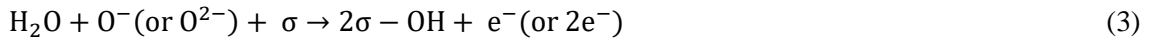
SnO₂ is one of key materials being widely used in applications such as transparent electrodes, catalysts, and gas sensors [1-3]. As a gas sensor, one can sense present gases from the electric resistance change derived from the catalytic reaction of chemisorbed oxygen molecules on SnO₂ with analytes. Oxygen molecules are dissociatively adsorbed to surface Sn⁴⁺ ions or oxygen vacancies and they turn into the form of O⁻ and/or O²⁻ [4]. The relationship between the electric resistance and oxygen partial pressure was expressed as following equations [5]:

$$\frac{R}{R_0} = \frac{3}{a} (K_1 P_{O_2})^{1/2} + c \quad (\text{in the form of } O^-) \quad (1)$$

$$\frac{R}{R_0} = \left\{ \frac{1}{4} c^2 + \frac{6N_D}{a} (K_2 P_{O_2})^{1/2} \right\}^{1/2} + c \quad (\text{in the form of } O^{2-}) \quad (2)$$

where R and R₀ are electrical resistance in the atmosphere with and without oxygen, respectively, a is crystallite radius, K₁ and K₂ was equilibrium constants of oxygen adsorption, P_{O₂} is oxygen partial pressure, N_d is donor density, and c is constant. The electric resistance is largely depending on P_{O₂} reflecting major adsorbed oxygen. O⁻ brings proportional resistance to square root of P_{O₂} and O²⁻ brings that to fourth root of P_{O₂}. Actually, O⁻ and O²⁻ are competitively adsorbed and their component is dependent on the temperature and the atmosphere [4, 6]. In a dry condition, the major adsorbed species is O²⁻ at 350°C and over, whereas O⁻ also adsorbed below this temperature.

On the other hand, in a humid atmosphere, water vapor adsorbed dissociatively to the same sites as oxygen and turns into hydroxyl groups [7, 8]. This reaction is called hydroxyl poisoning and is expressed as follows:



where σ is common adsorption site in oxygen and water vapor, $\sigma - \text{OH}$ is adsorbed hydroxyl group and e is carrier electron. Previous researches demonstrated that the electric resistance in humid condition was proportional to square root of P_{O_2} , indicating major adsorbed oxygen is O^- after O^{2-} was preferentially substituted with O^- [4, 9]. Because water vapor impedes the oxygen adsorption and donates electron conversely to oxygen, humid condition lowers the sensing performance significantly. To decrease the effect of water vapor, complexing with other components is promising way to bring water vapor tolerance. Especially, dispersed Pd particles bring O^{2-} adsorption sites and leads to suppression of susceptibility to water vapor [9]. In other case, doped Sb cation acted as a hydroxyl absorber and SnO_2 retains O^{2-} , leading to high tolerance to water vapor [10]. It is known that some other elements or materials (e.g. Al, Ti, CuO, NiO) also act as hydroxyl absorbers for SnO_2 -based gas sensor [11-14].

We previously synthesized the core-shell $\text{SiO}_2/\text{SnO}_2$ nanofibers using TMEPO-oxidized cellulose nanofibers as templates [15]. Although it was reported the complexing with SiO_2 led to higher selectivity and sensitivity [16-18], there has not been successful reports on the use of SiO_2 as hydroxyl absorbers in spite of its high affinity to water [19].

To investigate the tolerance of the $\text{SiO}_2/\text{SnO}_2$ nanofibers to water vapor, the gas sensing properties in humid conditions were evaluated.

3.4.2 Experimental procedure

The detailed synthesis procedure of materials and the fabrication process of a sensor element were reported in previous section. In particular, the SiO₂/SnO₂ nanofibers were synthesized using acetylacetone (acac, Kishida Chemicals) with the acac/Sn molar ratio of 500 followed by calcination at 500°C.

Figure 1 shows a schematic of the evaluation system of gas sensing properties. Electric resistance changes under the introduction of H₂ or CO analyte gas containing certain amount of water vapor were monitored by a digital multimeter (model 2701, Keithley). The H₂ or CO analyte gas including air (Taiyo Nippon Sanso) was further diluted with synthetic air (Taiyo Nippon Sanso) to be 200 ppm with mass flow controllers (Horiba Stec). Then, the flow was divided into two flows. One flow, which was blown into distilled water, was mixed with the other dry flow to prepare humid flow containing from 0 to 3 vol% water vapor. Sequentially, the analyte gas was introduced toward a sensor element in a reaction tube under heating by a tube furnace. The humidity in the outlet gas was monitored with a humidity sensor (TR-77Ui, T&D Corporation). The operating temperatures were 450°C or 400°C in the case of H₂ analyte gas. In the case of CO analyte gas, the temperatures were set to be no higher than 400°C, to avoid the reduction of lattice oxygen in SnO₂ [20]. All measurements were carried out after the refreshing at 480°C for 1 h in dry air and subsequently for 2 h in 3 vol% humid air to eliminate adsorbed residues derived from analytes, and then the cooling down to a operation temperature with the rate of 0.556°C/min. The gas sensitivity is conventionally defined as follows [21]:

$$\text{Sensitivity} = R_a/R_g \quad (4)$$

where R_a is electrical resistance for clean air and R_g is electrical resistance for target analyte gas. The dependence of the resistance on oxygen partial pressures (P_{O_2}) was also investigated by

introducing the mixture of N₂ (Taiyo Nippon Sanso) and O₂ (Taiyo Nippon Sanso), where P_{O₂} was monitored with a stabilized zirconia cell [6].

3.4.3 Results and Discussion

Figure 2 shows the electric resistances of the sensor elements in synthetic air containing various concentration of water vapor at 450°C and 400°C. In both temperatures, the resistances once decreased rapidly with the introduction of water vapor and decreased continuously with increasing humidity, reflecting hydroxyl poisoning as shown in Eq. 3. At 450°C, the decrements in the resistances with increasing humidity were lower than that at 400°C because the hydroxyl groups desorbs at higher temperature [22]. Meanwhile at 400°C, the SiO₂/SnO₂ nanofibers indicated clearly slow decreasing gradient of the resistances to the humidity compared to that for the SnO₂ nanoparticles. This tolerance to water vapor is presumed to be brought to by partially exposed SiO₂.

Figure 3 shows the electric resistance change of sensor elements under the introduction of H₂ or CO at 400°C or 450°C. The corresponding sensitivities are also shown in Figure 4.

Although in humid conditions, the sensitivities for the SiO₂/SnO₂ nanofibers were steeply decreased, a higher sensitivities compared to that for SnO₂ nanoparticles were nonetheless achieved. At 450°C, the sensitivities to H₂ in both samples were less affected by the increment of humidity due to the hydroxyl groups desorption. Whereas at 400°C, the sensitivities both to H₂ and CO for the SnO₂ nanoparticles were slightly decreased. It should be noted that the sensitivities both to H₂ and CO for the SiO₂/SnO₂ nanofibers exhibited little change by the increment of humidity. These results are consistent with the relationship between the electric resistances and the concentration of water vapor as shown in Fig. 2.

As it for the former studies [10-14], the SiO₂ seemed to act as an absorber for water molecules through hydrogen bonding or hydroxylation [19]. On the contrary, there was the report that SiO₂-SnO₂ nanocomposites containing SiO₂ up to 5 wt% did not exhibit any tolerance to water vapor [23]. Meanwhile in this study, the SiO₂/SnO₂ nanofibers had higher weigh ratio about 43 wt% and the exposed area of SiO₂ was sufficient to influence the zeta potential as described in previous section. Such situations enable to presume that the larger area of SiO₂ affected the surface reaction relating to water vapor.

The resistance changes depending on P_{O₂} in dry and humid condition at 450°C and 400°C are shown in Fig. 5 and 6, respectively. At 450°C, where hydroxyl groups desorbs, the resistances both of the SiO₂/SnO₂ nanofibers and the SnO₂ nanoparticles were proportional to P_{O₂}^{1/4} in dry and humid conditions, which indicated the major adsorbed oxygen was O²⁻ regardless of the presence of the water vapor. On the other hand at 400°C, the behavior of each sample was clearly different. The resistances of the SnO₂ nanoparticles was proportional to P_{O₂}^{1/4} in dry condition but to P_{O₂}^{1/2} in humid condition. This relationship indicates that the major adsorbed oxygen was changed from O²⁻ to O⁻ similarly to the previous report [6]. However, the resistances of the SiO₂/SnO₂ nanofibers were neither proportional to P_{O₂}^{1/4} nor P_{O₂}^{1/2} in dry and humid condition, which means that O²⁻ and O⁻ adsorbed competitively regardless of humidity [6]. It is worth noting that O²⁻ still remained in humid condition at the surface of the SiO₂/SnO₂ nanofibers, which supports strongly the role of SiO₂ as an absorber for water molecules in the similar way to Sb doping [10].

Although the gas sensing properties of the SiO₂/SnO₂ nanofibers evaluated in this study is suitable for the practical use, further characterizations such as TPD and DRIFT analyses are required for understanding the fundamental mechanism.

3.4.4 Conclusion

The gas sensing properties of the SiO₂/SnO₂ nanofibers to H₂ and CO in humid conditions were evaluated compared to the conventional SnO₂ nanoparticles. It was revealed that the resistances and sensitivities of the SiO₂/SnO₂ nanofibers were less affected by the humidity than conventional SnO₂ nanoparticles. The major adsorbed oxygen species were estimated by the relationship between the resistance and oxygen partial pressure (P_{O_2}). Surprisingly, the major oxygen species of the SiO₂/SnO₂ nanofibers remained both O²⁻ and O⁻ under the introduction of water vapor at 400°C. While the dominant oxygen species of the SnO₂ nanoparticles was changed from O²⁻ to O⁻. It can be interpreted that SiO₂ partially exposed to the surface of the SiO₂/SnO₂ nanofibers acted as water absorbers to hinder hydrogen poisoning to adjacent SnO₂. Although the detailed mechanism of this tolerance to water vapor was not clear yet, such properties are suitable for the gas sensor in practical use.

References

1. Z. M. Jarzebski and J. P. Marton, *Journal of the Electrochemical Society* **123**, 333C (1976).
2. M. J. Fuller and M. E. Warwick, *Journal of Catalysis* **29**, 441 (1973).
3. N. Barsan, M. S.-Berberich, and W. Göpel, *Fresenius' Journal of Analytical Chemistry* **365**, 287 (1999).
4. N. Yamazoe, K. Suematsu, and K. Shimano, *Sensors and Actuators B* **176**, 443 (2013).
5. N. Yamazoe, K. Suematsu, and K. Shimano, *Sensors and Actuators B* **163**, 128 (2012).
6. K. Suematsu, M. Yuasa, T. Kida, N. Yamazoe, and K. Shimano, *Journal of The Electrochemical Society* **161**, B123 (2014).
7. D. Koziej, N. Barsan, U. Weimar, J. Szuber, K. Shimano, and N. Yamazoe, *Chemical Physics Letter* **410**, 321 (2005).
8. R. G. Pavelko, H. Daly, C. Hardacre, A. A. Vasiliev, and E. Llobet, *Physical Chemistry Chemical Physics* **12**, 2639 (2010).
9. N. Ma, K. Suematsu, M. Yuasa, T. Kida, and K. Shimano, *ACS Applied Materials & Interfaces* **7**, 5863 (2015).
10. K. Suematsu, M. Sasaki, N. Ma, M. Yuasa, and K. Shimano, *ACS Sensors* **1**, 913 (2016).
11. K. Suematsu, N. Ma, M. Yuasa, T. Kida, and K. Shimano, *RSC Advances* **5**, 86347 (2015).
12. A. Tricoli, M. Righettoni, and S. E. Pratsinis, *Nanotechnology* **20**, 315502 (2009).
13. H.-R. Kim, A. Haensch, I.-D. Kim, N. Barsan, U. Weimar, and J.-H. Lee, *Advanced Functional Materials*, **21**, 4456 (2011).
14. K.-I. Choi, H.-J. Kim, Y. C. Kang, J.-H. Lee, *Sensors and Actuators B: Chemical* **164**, 371 (2014).
15. S. Gunji, Y. Shimotsuna, T. Fujimoto, and K. Miura, *Frontiers in Nanoscience and Nanotechnology* **3**, 1 (2017).

16. G. Tournier and C. Pijolat, *Sensors and Actuators B* **106**, 553 (2005).
17. K. Wada and M. Egashira, *Sensors and Actuators B* **53**, 147 (1998).
18. A. Tricoli, M. Graf, and S. E. Pratsinis, *Advanced Functional Materials* **18**, 1969 (2008).
19. L. T. Zhuravlev, *Colloids and Surfaces A: Physicochemical and Engineering Aspects* **173**, 1 (2000).
20. J. Watson, K. Ihokura, and G. S. V. Coles, *Measurement Science and Technology* **4**, 711 (1993).
21. N. Yamazoe, K. Shimano, and C. Sawada, *Thin Solid Films* **515**, 8302 (2007).
22. N. Yamazoe, J. Fuchigami, M. Kishikawa, and T. Seiyama, *Surface Science* **86**, 335 (1979).
23. A. Tricoli, *Biosensors*, **2**, 221 (2012).

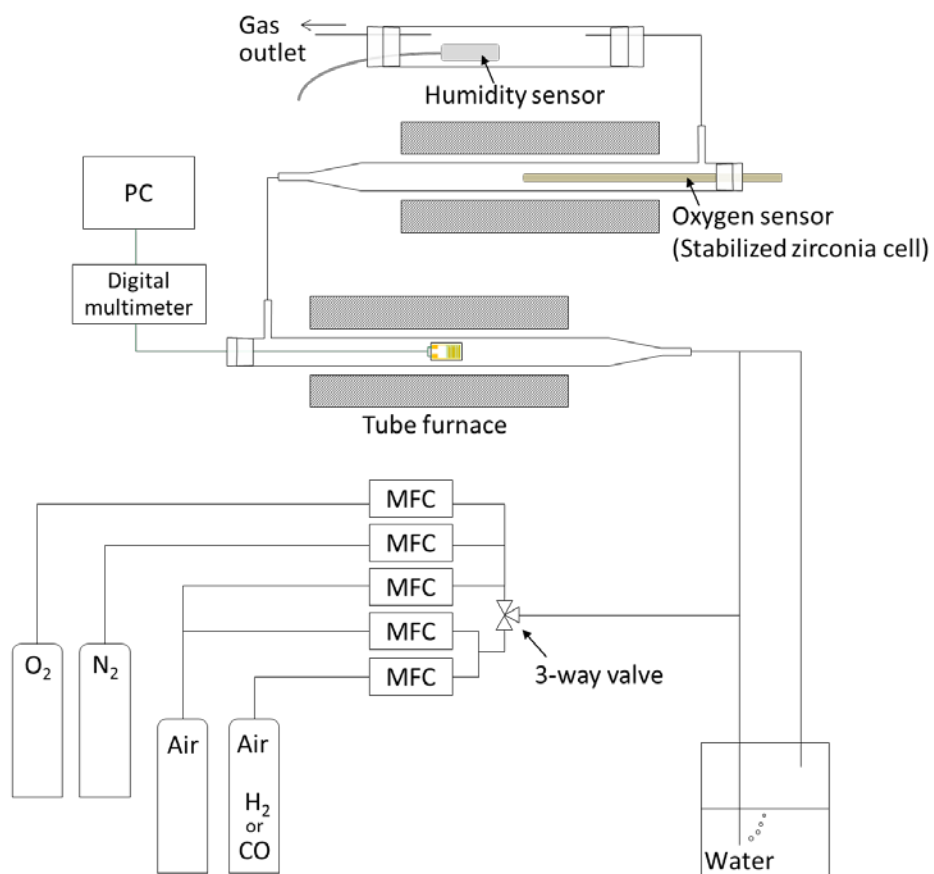


Fig. 1 Schematic of evaluation system of gas sensing properties in humid condition.

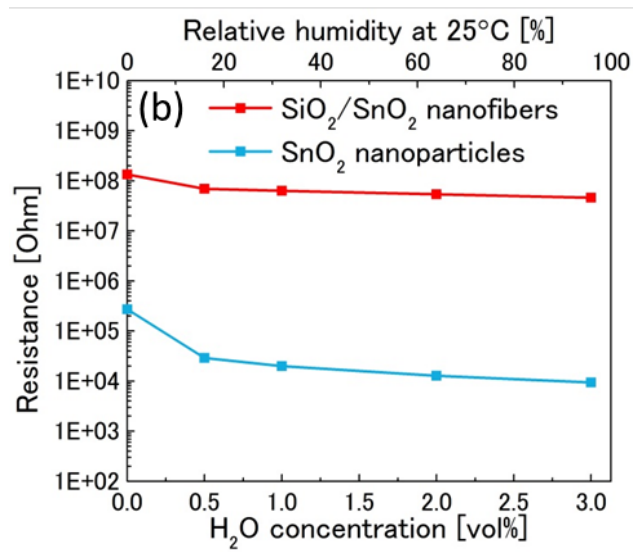
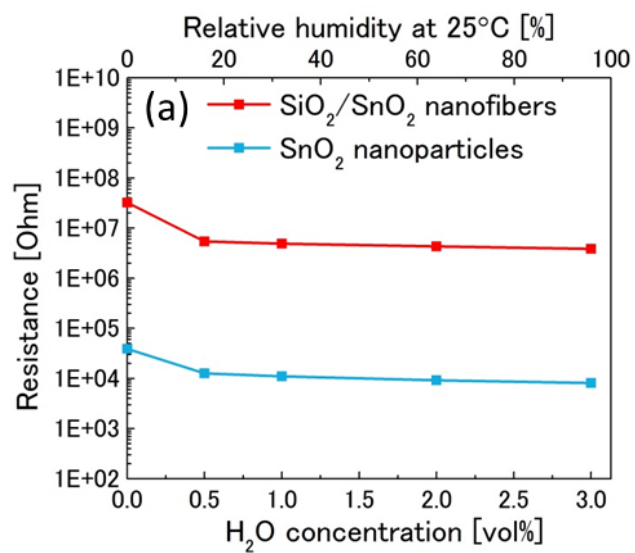


Fig. 2 Electric resistance related under various humidities at **a** 450°C and **b** 400°C .

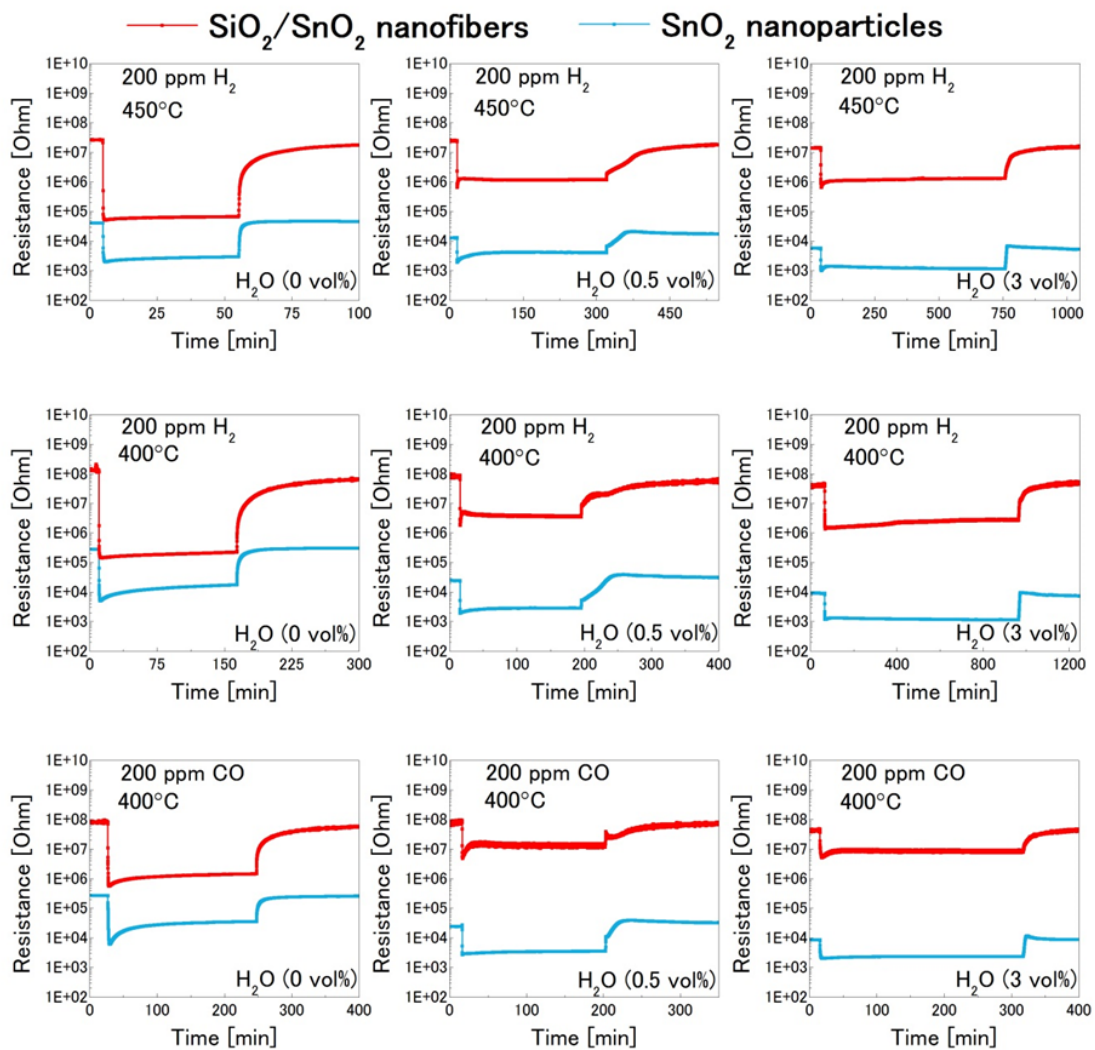


Fig. 3 Electric resistance changes under introduction of H_2 or CO at various temperatures and humidities.

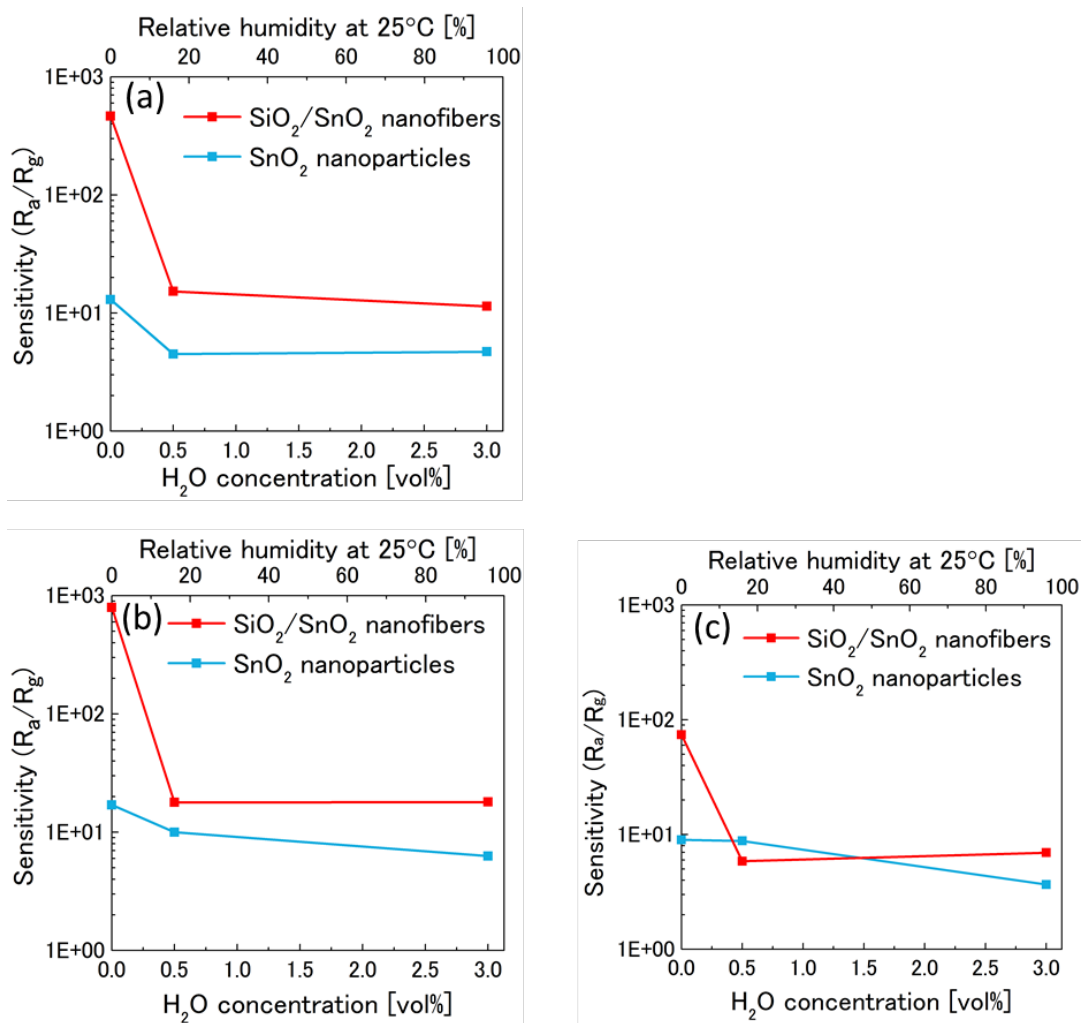


Fig. 4 Gas sensitivities under various humidities to **a** 200 ppm H_2 at 450°C, **b** 200 ppm H_2 at 400°C, and **c** 200 ppm CO at 400°C.

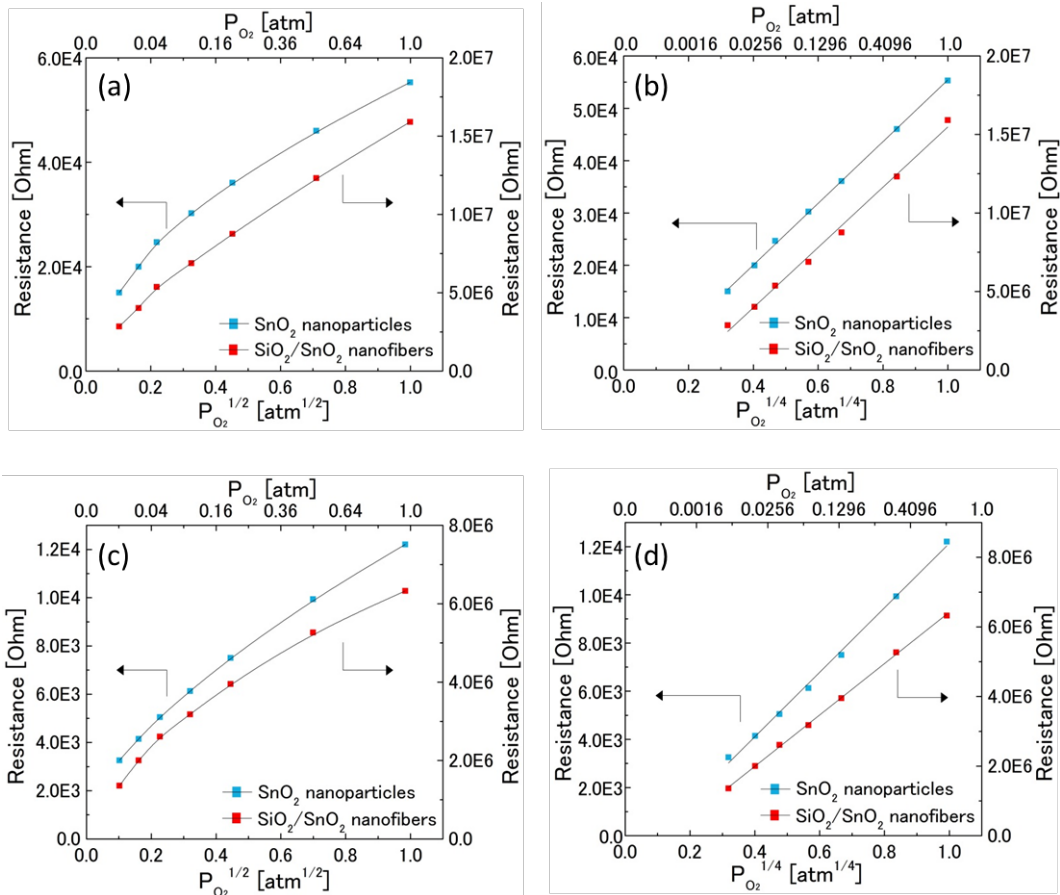


Fig. 5 Electric resistance depending on $P_{O_2}^{1/2}$ and $P_{O_2}^{1/4}$ at 450°C in **a, b** dry and **c, d** 3 vol% humid conditions.

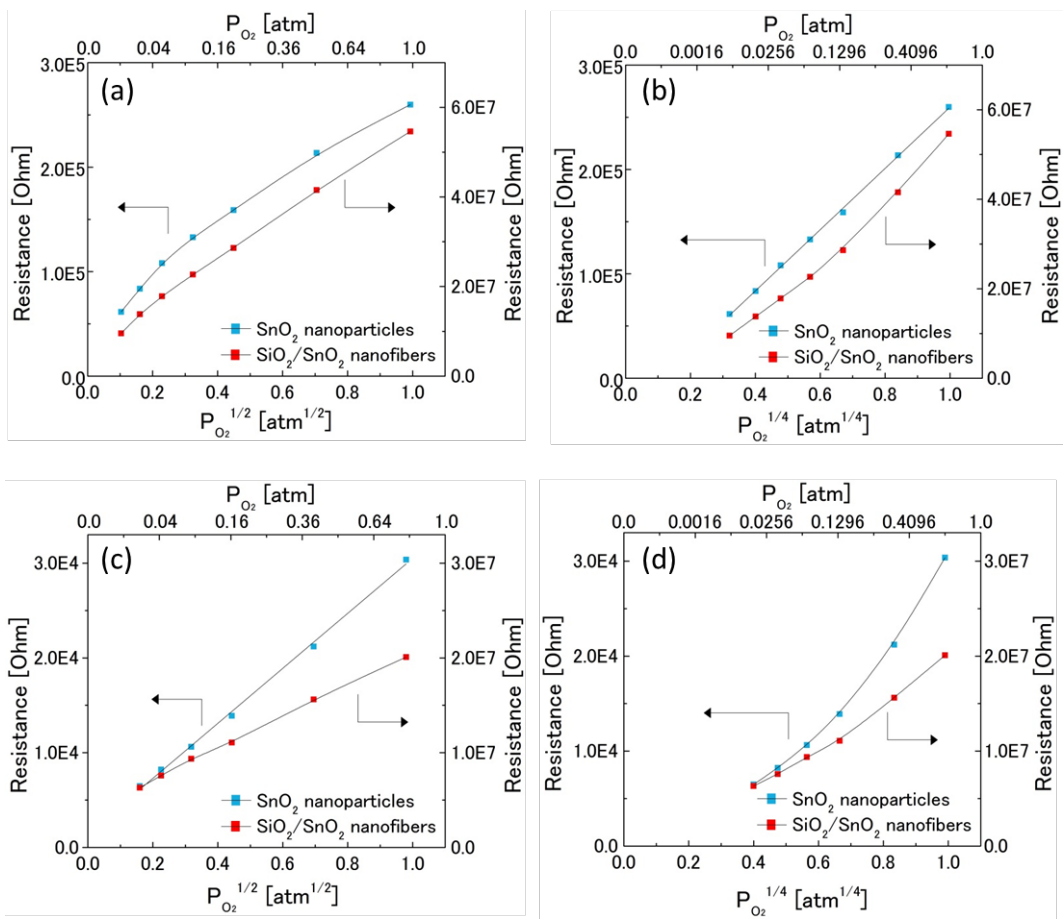


Fig. 6 Electric resistance depending on $P_{O_2}^{1/2}$ and $P_{O_2}^{1/4}$ at 400°C in **a, b** dry and **c, d** 3 vol% humid conditions.

Publication List

Chapter 1 and Chapter 2

“Synthesis of TiO_2 - SiO_2 nanofibers by using TEMPO oxidized cellulose nanofibers as templates”,

Shunsuke Gunji, Yasuhiko Shimotsuma, and Kiyotaka Miura,

Proceedings of the XVIII edition of the International Sol-Gel Conference (2015)

“Synthesis of TiO_2 - SiO_2 nanofibers using templates of TEMPO oxidized cellulose nanofibers”,

Shunsuke Gunji, Yasuhiko Shimotsuma, and Kiyotaka Miura,

Proceedings of 4th International Nanofiber Symposium (2015)

“Synthesis and photocatalytic properties of $\text{SiO}_2/\text{TiO}_2$ nanofibers using templates of TEMPO-oxidized cellulose nanofibers”,

Shunsuke Gunji, Yasuhiko Shimotsuma, and Kiyotaka Miura

Journal of Sol-Gel Science and Technology, Vol. 79, pp. 151-159 (2016)

Chapter 3

“Synthesis of $\text{SiO}_2/\text{SnO}_2$ nanofibers using TEMPO-oxidized cellulose nanofibers as templates”,

Shunsuke Gunji, Yasuhiko Shimotsuma, Tetsuya Fujimoto and Kiyotaka Miura,

Frontiers in Nanoscience and Nanotechnology, Vol. 3, pp. 1-4 (2017).

“Effect of SiO₂ on gas sensing properties in SiO₂/SnO₂ core-shell nanofibers “,

Shunsuke Gunji, Yasuhiko Shimotsuma, Ken Watanabe, Koichi Suematsu, Kengo Shimano, and Kiyotaka Miura,

Journal of Materials Chemistry C (to be submitted)

Acknowledgements

The present thesis has been carried out at Department of Material Chemistry, Graduate School of Engineering, Kyoto University under the direction of Professor Kiyotaka Miura.

First of all, the author would like to show his greatest appreciation to Professor Kiyotaka Miura for his warm encouragement, supportive suggestion, and valuable advice, ever since the author entered the laboratory.

The author demonstrates his gratitude to Associate Professor Yasuhiko Shimotsuma. Without his perseverant guidance and constructive advice this thesis would not have been possible.

Advices and comments given by Program-Specific Associate Professor Masaaki Sakakura has been a great help to acquire groundings for physics and programming.

The author would like to offer his special thanks to Doctor Keisuke Kametani for warm assistance to use apparatuses in Next Generation Laser Processing Technology Research Association.

The author also sincerely appreciates insightful comments and encouragements given by Assistant Professor Shunsuke Murai and Assistant Professor Masahiro Shimizu.

The author expresses his appreciation to Assistant Professor Koichi Suematsu, Associate Professor Ken Watanabe, and Professor Kengo Shimanoe in Kyushu University for the permission to use a gas sensing apparatus and for valuable comment.

Finally, the author would like to respectfully grateful to his parents, Fumio Gunji, Satoko Gunji, and his grandmothers, brothers for all their support and encouragement.

Shunsuke Gunji

Copyrights and Sources

The content of Chapter 1 and 2 was published in Journal of Sol-Gel Science and Technology and is made available as an electronic reprint with the permission of Springer Science+Business Media. The paper can be found at the following URL on the SpringerLink: [<http://link.springer.com/article/10.1007/s10971-016-4033-0>]. Systematic or multiple reproduction or distribution to multiple locations via electronic or other means is prohibited and is subject to penalties under law.

The content of Chapter 3 was published in Frontiers in Nanoscience and Nanotechnology. The paper can be found at the following URL on the Open Access Text: [<https://oatext.com/Synthesis-of-SiO2SnO2-nanofibers-using-TEMPO-oxidized-cellulose-nanofibers-as-templates.php>] and the DOI is as follows [DOI: 10.15761/FNN.1000144].

© 2017 Shunsuke Gunji, Yasuhiko Shimotsuma, Tetsuya Fujimoto, Kiyotaka Miura
